NASA Contractor Report 198287

An Experimental Investigation of Wall-Cooling Effects on Hypersonic Boundary-Layer Stability in a Quiet Wind Tunnel

Alan E. Blanchard and Gregory V. Selby
Old Dominion University, Norfolk, Virginia

Cooperative Agreement NCC1-180

February 1996

National Aeronautics and
Space Administration
Langley Research Center
Hampton, Virginia 23681-0001

ACKNOWLEDGMENTS

There are several other people that the authors would like to acknowledge for their efforts during the course of this experiment. For innumerable fruitful discussions throughout the course of this work and for developing an adaptable traversing routine, Jason T. Lachowicz is thanked. Since he ensured that all required materials, equipment, and facilities were available for the successful execution of this experiment, Steve Wilkinson is acknowledged. For their patience in explaining the CVA system and their trust in allowing a prototype CVA to be used in this research, Dr. Sarma and Tao Systems are acknowledged. Finally, the financial assistance of NASA is acknowledged.

TABLE OF CONTENTS

Page

Chapter

LIST OF FIGURES

NOMENCLATURE

A = disturbance amplitude
A_o = initial amplitude or amplitude at most upstream location
f = frequency, Hz
M = Mach number
N = integrated growth rate
P_o = stagnation pressure, psia
q' = an arbitrary fluctuating quantity
$\hat{q}$ = eigenfunction of q'
Re_∞ = unit Reynolds number, per foot
R_w = resistance of the hot-wire sensing element
$R_{w,adiabatic}$ = resistance of the hot-wire sensing element without heating
S = distance along the body of the cone surface, in.
t = time, s
T_o = stagnation temperature, °R
V_{rh} = voltage input to CVA to set wire voltage
$V_{s,RMS}$ = RMS voltage of CVA output
$V_{s,mean}$ = mean voltage of CVA output
x = distance along the axis on the cone, in.
y = distance normal to the x-axis
$-\alpha_i$ = spatial growth rate, 1/in.
δ = boundary layer thickness, in.
ω = frequency, rad/s

CHAPTER 1

INTRODUCTION

1.1 Purpose of the Present Research

The design of high-speed aircraft is linked to the knowledge of high-speed boundary-layer stability. For an aircraft to withstand the aerodynamic heating loads of hypersonic flight, it must employ active cooling and/or be constructed of expensive composite materials that retain their strength at elevated temperatures. The designer must confidently estimate the heating loads in order to select an appropriate, cost-effective construction material and/or cooling system. Heating loads, however, depend on whether the boundary layer is turbulent or laminar. In addition to the aerodynamic heating problem, there are also cases where the high-speed flow must be turbulent for thorough fuel-air mixing prior to combustion.[1] Furthermore, the aerodynamic performance of aircraft, whether high- or low-speed, depends on the nature of the boundary layer over the aircraft. Consequently, the stability and transition of high-speed flow is a crucial factor in the design of high-speed aircraft.

Since experimental data are fundamental to the understanding of boundary-layer stability, the purpose of this research was to conduct a parametric investigation of the stability of the 91-6 cone boundary layer, with variable wall temperature, in Mach 6 quiet flow and compare the results with theoretical predictions. This comparison between experiment and theory can reveal the extent of linear stability theory as a valid predictor of instability phenomena in hypersonic flows. Moreover, as the boundary layer becomes turbulent, new, valuable information related to nonlinear instability can be obtained for future transition-modeling codes.

1.2 Linear Stability Theory

The transition zone in a boundary layer is bordered on the upstream end by predictable laminar flow and on the downstream end by unpredictable turbulent flow. Within this zone, infinitesimal disturbance waves experience exponential growth and decay in the "linear" region as Re increases. Once the instability waves grow to a finite amplitude, the transition process enters a "nonlinear" region where nonlinear events, such as harmonic generation and mean-flow distortion, occur.[2] The distortion of the mean flow further destabilizes the flow to opportunistic secondary instabilities.[3,4] The multiplicity of growing and interacting flow disturbances in the nonlinear region results in a coherent, three-dimensional fluctuating flowfield that ultimately breaks down into turbulence and signifies the end of the transition zone.[5] It should be noted that the linear region is usually much longer in extent than the nonlinear region.[6] The foregoing description of the transition zone does not apply universally, but is the most common phenomenology of transition.

Linear stability theory (LST)[7,8] describes a mathematical approach used to predict the growth and decay of spatially and temporally periodic disturbances in a boundary layer in the linear region of the transition zone. To formulate the stability equations, the governing flow equations are identified and each flow variable is assumed to be composed of mean and fluctuating components. These quantities are substituted into the governing equations and the resulting equations are linearized. The original mean-flow equations are then subtracted from the linearized equations and a parallel flow assumption is imposed; i.e., the profile of the mean flow quantities depends only on the normal distance from the wall boundary. A functional form of the oscillatory disturbances is then assumed:

$$q' = \hat{q}(y)\exp[i(\alpha x + \beta z - \omega t)] \qquad \text{(Eqn.1.1)}$$

where $\hat{q}(y)$ is the eigenfunction that defines the amplitude profile and $\exp[i(\alpha x + \beta z - \omega t)]$ describes the frequency and spatial orientation of the disturbance. In order to evaluate the stability of this disturbance, assumptions must be made regarding its growth (either spatial or temporal) and orientation angle. If the spatial growth of a two-dimensional disturbance propagating in the x-direction is to be investigated, then the frequency, ω, is real; the x-wavenumber, α, is complex; and the z-wavenumber, β, is zero. The resulting flow disturbance would have the following form:

$$q' = \hat{q}(y) \exp[i(\alpha_r x - \omega t)] \exp(-\alpha_i x) \qquad \text{(Eqn.1.2)}$$

where $\exp(-\alpha_i x)$ defines the spatial growth of the disturbance. Clearly, when $-\alpha_i$ is positive (α_i is negative), the disturbance will grow at an exponential rate in the x-direction. The primary objective of linear stability theory is to determine the growth rate of a given disturbance frequency at a specific x location.

For the case of incompressible flow, there are inviscid, viscous, and centripetal instability mechanisms that can lead to the growth of flow disturbances. Once viscous forces are neglected, the second-order Rayleigh equation governs the flow stability. In order for a disturbance to grow inviscidly, a point of inflection must exist in the velocity profile and there must also be some location in the boundary layer where the following inequality applies: $U''(U-U_s)<0$. For this inequality, U'' is the second derivative of the velocity and U_s is the magnitude of the velocity at the inflection point. There are a number of parallel shear flows where this "inviscid instability" or "Rayleigh instability" mechanism is applicable including Blasius flows with adverse pressure gradients, wakes, jets, and mixing layers. The velocity profiles for these flows are shown in Fig. 1.1 and the existence of inflection point(s) is clear in each case . In the absence of an inflection point in the boundary-layer velocity profile, such as Blasius flow or plane Poiseuille flow (see Fig. 1.1), the effects of viscosity must be included to explain the instability that develops in these flows. Upon including the viscous terms, the fourth-order Orr-Sommerfeld stability equation is found to govern the stability of the flow. In the case of the inviscid instability mechanism, viscosity acts to stabilize the flow; however, in the case of flows without an inflection point, viscosity acts to destabilize the flow over a finite Re range. The disturbances that grow in Blasius flow due to the destabilizing effect of viscosity are known as Tollmien-Schlichting waves. As Re increases, viscous forces decrease and the flow tends toward its stability as predicted using the inviscid theory. Since the viscosity of a fluid is dependent upon temperature, the destabilizing effects of viscosity will decrease as the temperature of a gas decreases (the opposite will happen for a liquid), thereby decreasing the viscosity of the gas. This can occur if the wall temperature is decreased through an active cooling process. Another type of instability mechanism is introduced if the flow boundaries include curved surfaces, as in the case of Görtler, Taylor, and Dean flows (see Fig. 1.1). In these cases, when the flow reacts to the centripetal force (induced by the surface curvature) by forcing high-momentum fluid into low-momentum fluid; e.g., the Görtler case shown in Fig. 1.1, the flow is destabilized and vortices develop. However, when low-momentum fluid is forced into high-momentum fluid; e.g., when the inner cylinder of the Taylor flow is at rest and the outer is rotating, the flow is stable. Hence, there exist a variety of instability mechanisms that may lead to the growth of disturbances in the transition zone of an incompressible flow depending upon the curvature of the velocity profile, the curvature of the wall boundaries, and the viscous forces.

For the flow of interest in the present research, the stability equations must be derived from the Navier-Stokes equations governing the flow of a viscous, compressible fluid. The detailed derivation of the eighth-order system of compressible stability equations and the bounded boundary conditions will not be repeated here but can be found in Ref. 7 and also in References 9 and 10.

The highlights of the compressible stability equations using only the inviscid theory will now be summarized. From Lees and Lin[11], the importance of the "generalized inflection point" was shown as a sufficient condition for the existence of unstable disturbances. This generalized inflection point is

$$\frac{d}{dy}\left[\rho\frac{dU}{dy}\right]=0 \qquad \text{(Eqn.1.3)}$$

and if density is held constant, the incompressible inflection point, U"=0, is recovered. This generalized inflection point plays the same role in compressible flow as does the velocity inflection point in incompressible flow. From the work of Mack[7], a critical observation regarding the importance of the "relative Mach number," $\hat{M}$, as defined below[5], was made:

$$\hat{M}=M-\frac{c}{a} \qquad \text{(Eqn.1.4)}$$

In Eqn.1.4, "M" is the local Mach number, "c" is the phase velocity of the disturbance which is equal to ω/α_r for spatial stability theory, and "a" is the local speed of sound. Disturbances in the compressible boundary layer are classified depending on the magnitude of $\hat{M}^2$:

$\hat{M}^2 < 1$	Subsonic Disturbance	(Eqn.1.5a)
$\hat{M}^2 = 1$	Sonic Disturbance	(Eqn.1.5b)
$\hat{M}^2 > 1$	Supersonic Disturbance	(Eqn.1.5c)

Mack was the first to discover that the mathematical nature of the stability equations for a compressible flow with a locally supersonic disturbance changes from elliptic (if the proper assumptions are made), with a unique wavenumber solution, to hyperbolic, with infinitely many wavenumber solutions. The additional solutions have come to be known as higher modes or "Mack" modes in his honor, and they begin to appear when the Mach number exceeds 2.2 in the case of flat-plate flow over an adiabatic wall. There are no analogous Mack modes in incompressible flow since there are no locally supersonic disturbances.

Mack made many important findings related to his inviscid investigation of these higher modes. The first of the additional modes, or the second mode, was found to be the most unstable of the additional higher modes for all Mach numbers. The wavenumber was found to be inversely proportional to the thickness of the relative supersonic layer; i.e., there was a mathematical link between the thickness of the boundary layer and the frequency of the higher-mode disturbances. Moreover, there was evidence that the maximum amplification rate was also inversely proportional to boundary-layer thickness. Hence, any parameter that alters the boundary-layer thickness will also affect the frequency and the growth rate of second-mode disturbances. The most unstable second mode was always a two-dimensional wave for all Mach numbers; however, as the freestream exceeded the sonic value, the most unstable first mode was an oblique, three-dimensional wave with an inclination angle; e.g., a wave of 60° at M=2. For the flow over an insulated wall, the first mode was the most unstable disturbance up to M=3.8, after which the second mode became the most unstable. Also, second-mode disturbances tended to have much higher frequencies than the first mode.

What may arguably be considered the most important of Mack's findings was related to the effect of wall cooling. Before Mack's discovery, it had been predicted that wall cooling could completely stabilize the flow of a compressible boundary layer[12] for Mach numbers between 1 and 9. Mack showed that the first mode could be completely stabilized (with oblique orientations requiring greater cooling rates), but the effect of wall cooling on the second mode was much different. Since the second mode is generated by an inviscid instability mechanism, wall cooling cannot eliminate the presence of this mode. Unlike the first mode, the second mode increases in maximum amplification rate and wave number with wall cooling. This increase in second-mode instability was due to the increase in the region of relative supersonic mean flow. In essence, the second mode was destabilized by wall cooling and the most unstable second mode was still a two-dimensional wave. Mack showed conclusively that due to the presence of the second and higher modes, wall cooling is not a viable method of achieving a stable, compressible boundary layer.

Mack also investigated compressible flow stability when the viscous terms were not neglected. He found that viscosity always had a stabilizing effect on the second mode for all Re and Mach numbers, with finite Re second-mode disturbances having lower amplification rates than predicted by inviscid theory. This is the same trend that exists in incompressible flows when the effects of viscosity are included in the analysis of an inviscid instability. As M increased, the viscous instability effect was seen to decrease and eventually disappear. Two-dimensional second-mode disturbances were still more unstable than oblique second-mode disturbances at finite Re. When wall cooling was included with the viscous analysis for the second mode, the inviscid theory trends persisted; i.e., the boundary-layer reduction due to the cooling generated an increase in disturbance frequency.

The physical manifestation of the first- and second-mode disturbances over a flat plate will now be described. As shown in the typical eigenfunctions of Ref. 4, the Mach number plays a crucial role in defining the character of the first mode. At subsonic Mach numbers, there is no second mode, due to the lack of supersonic disturbances, and the dominant first mode is a relatively low frequency velocity fluctuation with a broad amplitude distribution throughout the boundary layer. As the Mach number increases, the velocity eigenfunction does not change appreciably in either amplitude or extent; however, a temperature fluctuation develops as the region of relative supersonic mean flow increases. At M=4.5, this temperature fluctuation has a maximum amplitude that is 15 times that of the velocity fluctuation, but the disturbance is confined to a region near the boundary-layer edge. The second mode is primarily a high-frequency temperature and density[13] fluctuation also confined to a region near the boundary-layer edge with relatively insignificant velocity contributions. Thus, once the Mach number increases beyond four, the first- and second-mode flow disturbances are primarily temperature fluctuations with maximum amplitudes near the boundary-layer edge.

The results of Mack's LST analysis highlight aspects of compressible flow stability germane to the present research. Unlike an incompressible flow, both low-frequency first-mode and high-frequency second-mode disturbances can coexist in the compressible boundary layer. In addition, the maximum amplitude of the temperature disturbances associated with both modes at hypersonic Mach numbers will occur near the boundary-layer edge. Wall cooling will stabilize the first mode, but destabilize the second mode due primarily to the decrease in boundary-layer thickness.

1.3 The 91-6 Cone and its Predicted Boundary-Layer Stability

Due to the physical constraints of the M6NTC quiet wind tunnel used in the present research, a flared-cone model geometry was used that would produce measurable disturbance growth in the boundary layer over a short length. The M6NTC exit diameter is 7.5 in. and the usable quiet core length is less than 25 in. long. The slow growth of disturbances in a straight-cone boundary layer necessitated the addition of a flare on the cone model to produce an adverse pressure gradient. With this flare, second-mode cone model disturbances grew more quickly to measurable levels and transition was detectable on the cone surface. The main effect of the flare (for the second mode) was to maintain an approximately constant boundary-layer thickness over the flare region thereby allowing a constant frequency second-mode disturbance to grow. The final geometry of the cone model with flared afterbody used in this research is shown in Fig. 1.2. The nomenclature "91-6" defines a flare radius of 91 in. and a straight cone section 6 in. long upstream of the flare.

A thorough numerical investigation of various cone geometries was conducted by Balakumar and Malik[14] using the quasi-parallel, compressible linear stability e^{Malik} code,[15] which documented the parametric effects of the pressure gradient and wall cooling on the stability of the flow over the 91-6 cone. The mean-flow parameters of interest to the present research are $T_0=810^{\circ}R$, $P_0=130$ psia and $M=6$. For the viscous first-mode disturbances, the most unstable frequency was 70kHz and grew to N=4 at x=16 in. for the straight-cone case. The addition of the adverse pressure gradient (due to the flare) introduced an inviscid instability mechanism and increased the growth of the first mode to N=5.3. Wall cooling reduced the viscous effects (via a reduction in viscosity with reduced temperature) and removed the inflectional instability thereby stabilizing the first mode and reducing N. For the inviscidly unstable second mode, the most unstable straight-cone frequency was 210kHz, which grew to N=4.4 at x=16 in. This growth is comparable to the first mode case, but the frequency has tripled as is characteristic of the second mode. The addition of the flare shifted the most unstable second-mode frequency to 270kHz and the growth increased to N=10.7. This occurred because the boundary-layer thickness was held constant in the flared region thereby allowing a constant-frequency second mode to grow. For comparison, disturbances are usually detectable experimentally after N=5 and flow transition occurs near N=10.[16-18] Wall cooling shifted the second-mode frequency even higher -- to 310kHz -- and the disturbance growth dramatically increased to N=15.8. The increase in frequency, as well as the increase in growth in the cooled wall case, can be attributed to the enhanced region of relative supersonic mean flow. As the trends of Mack showed, the decrease in boundary-layer thickness accompanying the introduction of both the flare and wall cooling increased the second-mode frequency and growth.

Expected experimental results are clear from the numerical investigation.[14] For the adiabatic-wall case, the dominant flow-disturbance frequency should be 270kHz since maximum growth is observed at this second-mode frequency. There should be little or no shifting of the dominant second-mode frequency since the boundary layer is approximately constant. Once cooling is applied, there should be a detectable frequency increase to 310kHz and a substantial increase in disturbance growth. The accompanying decrease in transition Re should be detectable. Since the first-mode disturbances do not grow significantly above the N=5 level, it was questionable whether their detection would be possible.

1.4 Comparison of LST and Experimental Data

Compressible LST has been used to predict the growth rates of various frequencies at select Re for a variety of boundary layers. To compare with the LST analysis, experimental amplitudes, A, for the same frequency may be reduced using the following relationship:

$$\frac{1}{A}\frac{dA}{dx} = -\alpha_i \qquad \text{(Eqn.1.6a)}$$

or the mathematical equivalent:

$$\frac{d}{dx}(\ln A) = -\alpha_i \qquad \text{(Eqn.1.6b)}$$

It is accepted practice in stability experiments to acquire this amplitude data in the region of maximum RMS energy for each x location. For the present research, the flow is hypersonic and this maximum is expected to be located near the edge of the boundary layer. Since LST predicts growth rates and experimental data yields amplitudes, the integrated growth rate or N-factor can be calculated in order to directly compare experimental amplitudes to theory. The N-factor is defined as:

$$N = \int_{x_o}^{x} -\alpha_i(x)\,dx \qquad \text{(Eqn.1.7)}$$

The N-factor for a specific frequency is integrated from an upstream x_0 location where the disturbance amplitude is A_0. This x_0 location is typically the first- or second-mode neutral point on the stability diagram. To compare with the experimental amplitudes, A, the following relation is used:

$$\frac{A}{A_o} = e^N \qquad \text{(Eqn.1.8)}$$

where N is the value found using Eqn.1.7. Eqn.1.8 can also be expressed as:

$$\ln(A) - \ln(A_o) = N \qquad \text{(Eqn.1.9)}$$

which is similar to the "frequency response curve" used by Mack.[2] If the theoretical N-factor curves have been calculated for the flow in question, Eqn.1.9 indicates that the natural logarithm of the experimental amplitudes may be compared with the LST predictions by shifting the experimental data an amount, $\ln(A_0)$, and comparing the local slopes.[19]

The comparison between LST predictions and experimental data is straightforward. To perform the appropriate comparison, either set of raw results must be manipulated. To compare the LST growth rate directly with experimental data, the derivative of the experimental amplitudes must be taken using Eqn.1.6. To compare experimental amplitudes directly with LST using Eqn.1.9, the LST growth rate must be integrated using Eqn.1.7. There is a fundamental question as to which procedure introduces more error into the comparison. This issue will be further addressed in later chapters.

1.5 Quiet Tunnels and the M6NTC

The overriding feature defining the uniqueness of the present research is the use of a quiet tunnel environment. Whereas numerical models assume an ideal, noiseless flow (except for computational roundoff errors), experimental high-speed flows generally have a measurable freestream disturbance field at high Re_∞.[20-23] Due to wind-tunnel design variations, resulting disturbance fields interact with boundary layers differently and produce conflicting results for similar models. For example, Pate and Schueler[24] and Pate[25] found unexpected variations in transition Reynolds number for cone and flat plate models for $3<M<8$ in different wind tunnels. This result confirmed the undesirable effect of acoustic freestream disturbances in stability and transition research and helped establish the need for low-disturbance, high-speed, "quiet" tunnels.

High-speed wind tunnels can generate a variety of unsteady freestream disturbances that are classically characterized as vorticity, entropy, and sound modes[26] generated in the settling chamber or nozzle.[20,21] Vorticity mode disturbances, i.e. turbulence, are generally negligible for hypersonic nozzles due to the large flow expansion from the settling chamber to the test section.[22,27] Entropy mode disturbances; i.e., temperature "spottiness," are negligible if the heated flow has been thoroughly mixed prior to entering the test section.[21] The sound mode is the significant source of high-speed noise and has many sources, including Mach wave radiation from turbulent boundary layers, "shivering" Mach waves from surface irregularities, and sound wave propagation from the settling chamber.[20,21] In general, the radiant sound mode dominates the freestream disturbance field for high-speed flows and is primarily produced by acoustic disturbances radiating from the turbulent tunnel-wall boundary layer.[22]

Quiet-tunnel technology, developed and implemented at NASA-Langley Research Center, maximizes the region of laminar flow over the nozzle wall, thereby delaying the onset of turbulent nozzle-wall boundary layers and the attendant radiated sound.[28-30] Certain elements are unique to a typical quiet tunnel, as shown in Fig. 1.3. They are: 1) a suction slot upstream of the nozzle throat to bleed off the turbulent settling chamber boundary layer,[31] 2) a highly polished nozzle throat to minimize the transition-promoting effects of surface roughness,[32] 3) a straight contour just downstream of the nozzle throat to delay the development of Görtler vortices,[33] and 4) high-density porous plates in the settling chamber to attenuate upstream piping/valve noise. Transition research conducted in quiet tunnel environments shows transition trends closer to those obtained in free-flight than do data from conventional tunnels.[28] These data confirm the effectiveness of quiet tunnels for high-speed stability and transition research and the applicability to the present research.

As part of NASA Langley Research Center's program for hypersonic instability and transition research, a quiet Mach 6 facility was developed. This involved retrofitting a new quiet nozzle to the Langley Nozzle Test Chamber facility and modifying the settling chamber. The modified facility is commonly known as the Mach 6 Nozzle Test Chamber Facility or M6NTC. The nozzle has been thoroughly calibrated in support of the present research[34] and was found to be appropriate for hypersonic boundary-layer stability investigations.

1.6 Previous Experimentation

A major objective of transition-zone investigations is understanding flow transition mechanisms and their accurate modeling. Although there have been numerous transition experiments conducted (with and without wall cooling effects) where the "transition point" was identified under specific conditions, this information was very difficult to generalize and to apply to other flow situations, because there was little or no information about the nature of the flow disturbance responsible for transition.[35-68] Only stability experiments using traditional experimental techniques; e.g., hot-wire anemometry, give the necessary information for a detailed description of the transition process that is conducive to numerical modeling.

Despite their sparsity in the literature, there have been a number of significant high-speed stability experiments conducted in recent years since Mack's discovery of the higher disturbance modes. The motivation for nearly all boundary-layer stability experiments, regardless of flow regime, stems from the breakthrough experiments of Schubaurer and Skramstad[69] fifty years ago that showed the validity of the linear stability assumptions in incompressible flat-plate flow. Prior to the discovery of the higher modes, Demetriades conducted the first hypersonic stability experiments.[70,71] Kendall was the first to experimentally verify the existence of dominant disturbances in a hypersonic boundary layer[72] and to identify the second mode.[73] Demetriades conducted further experiments that verified Mack's predictions relating to wall cooling.[74,75] The work of Stetson, et al.,[76-86] throughout the past decade provides the most complete description of parametric effects on the stability of high-speed flow. Overall, the results of Stetson's studies agreed with the trends found in LST predictions for frequency and growth; however, these tests were conducted in a conventional high-speed tunnel with typical acoustic-radiation noise interference. Upon examining these data, it was found that the flow was transitioning at a relatively low N~4 value based on the saturation of the second-mode disturbances.[19] Since the emphasis in the previous experiments was on the linear region, possible secondary instabilities and the nonlinear breakdown of the two-dimensional second-mode disturbances were not investigated. Numerical investigations of secondary instability and the nonlinear region continue[3,13,87-89] - often using the parabolized stability equation (PSE) method - so the "great need for additional experimentation"[13] and "particularly hypersonic quiet tunnel stability experiments"[86] is understandable. In the area of high-speed stability experimentation, the present research represents a logical and anticipated step - stability experiments in a quiet-flow environment where the linear as well as the nonlinear regions may be investigated. Prior to the present research, the NASA-Langley quiet tunnels have been used primarily for transition experiments.[90]

1.7 Research Objectives

Intermediate tasks accomplished before initiating experiments included: conducting a literature search, designing a cooled-cone model with a cooling system, designing a traversing system with interchangeable hot-wire probes, designing a contact system, and evaluating the performance of the M6NTC.

The research objectives for the present experiment are as follows:

1) Use constant-voltage anemometry to investigate the boundary layer disturbances over the 91-6 cone under adiabatic and wall-cooling conditions;
2) Identify the most unstable frequencies, compare their growth with the LST predictions and reconcile any differences;
3) Identify any new stability phenomena associated with the quiet-flow environment;
4) Investigate the nonlinear region of the transition zone and identify possible transition mechanisms; and
5) Document the sensitivity of the experimental results to experimental parameters.

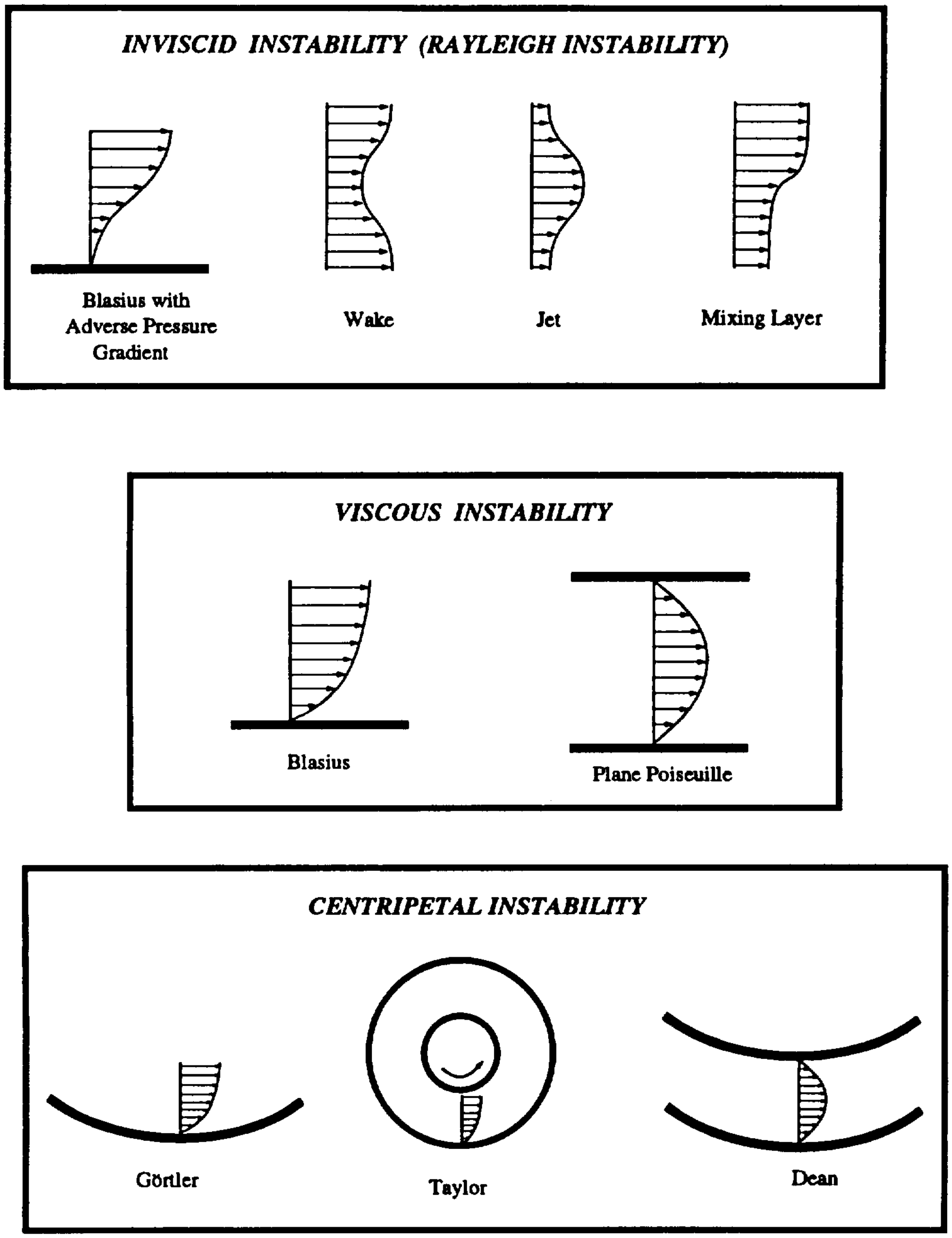

Figure 1.1 Characterization of Instability Mechanisms

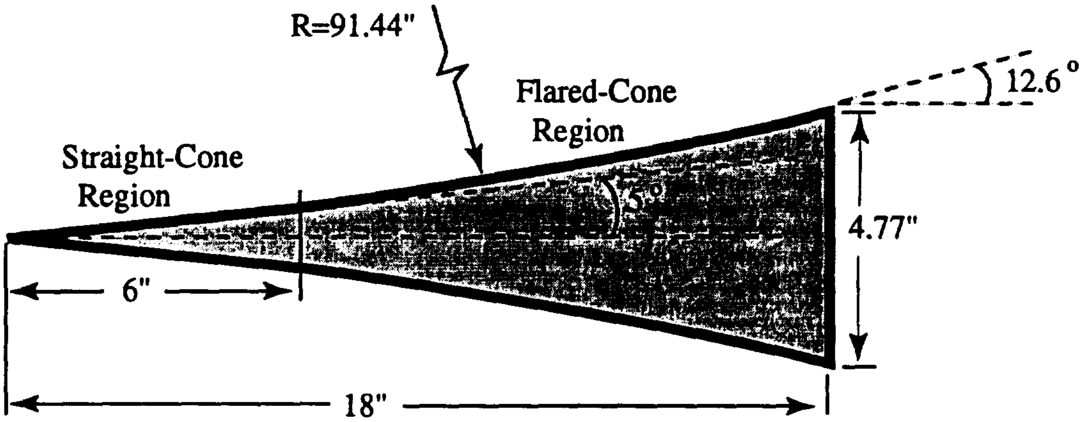

Figure 1.2 Geometry of the 91-6 Cooled-Cone Model

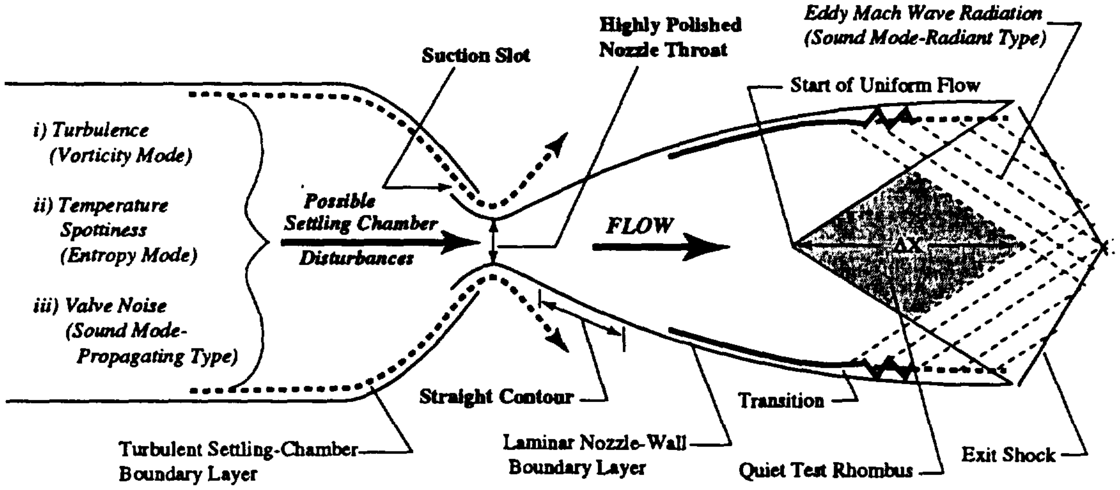

Figure 1.3 Typical Quiet Tunnel

CHAPTER 2

EXPERIMENTAL APPARATUS

2.1 Cone Model and Coolant System

As shown in Fig. 1.1, the cone has a straight 5° angle for the first 6 in. which tangentially merges into a flared region of radius 91.443 inches for the remaining 12 in. of its length. The total length of the cone is 18.0 in. and the base diameter is 4.768 in. As previously explained, the flare was added to the cone to promote high disturbance growth rates and to ensure that the end of the transition zone would be detectable on the cone.

The cone has a wall thickness of 0.080 in. and is instrumented with 51 T-type thermocouples along one ray of the cone and 30 pressure ports of diameter 0.020 in. located 180° from the thermocouple ray. All flow data were acquired in the plane of the thermocouples so that direct comparisons with wall temperature could be made.

The cone had a variety of surface imperfections. There was a notable manufacturing flaw in the symmetry of the cone - a 0.001-in. reduction in radius exists on the thermocouple side. This error in contour is, however, smooth and parallel to the flow direction. The tip-frustum interface produces a 0.0005 in. rearward-facing step relative to the flow direction. The cone tip is 1.5 in. long with a tip radius of approximately 0.0025 in. The cone had an rms finish of between 4 and 8 microinches; however, the sealant at the tip-frustum interface leaked during testing and produced approximately 10 randomly spaced roughness sites between x=1.5 in. and x=3 in. The height of these roughnesses appeared to be on the order of the tip-frustum interface height. Since the model was not moved during testing, these roughness sites were likely present for all tests; however, LST calculations predict that second mode frequencies are damped in this roughness region for both the adiabatic- and cooled-wall cases.

The cone is equipped with internal passages for active surface cooling, as depicted in Fig. 2.1. As shown, the frustum acts as a parallel-flow heat exchanger, while the tip is not cooled. In the cooling mode, an FTS Systems model RC211 Recirculating Cooler pumped Flourinert FC-72 through insulated stainless steel tubing to the cone and back to the cooler for heat removal. For steady-state operation of the cooler at tunnel flow conditions, the cooler set points were -15°C (465°R) for maximum cooling and 25°C (537°R) for minimum cooling. Once the set point was reached during testing, the fluid temperature was held to within ±1°C. Note that the LST calculations assumed a wall temperature of 420°R for the cooled case calculations, which is 10% lower than the lowest wall temperature achievable with the present cooling system. The sensitivity of the flow disturbances to the wall temperature was addressed in this research.

2.2 Mach 6 Nozzle Test Chamber (M6NTC)

The operating parameters of the M6NTC were selected to match those of the LST results at the highest practical Re_∞. For all tests, the tunnel operating parameters were held constant at T_0=810°R and P_0=130 psia with experimental errors of ±3°R and ±2 psi, respectively. The variation of centerline Mach number down the tunnel measured from a previous investigation[34] at the same stagnation conditions is presented in Fig. 2.2 and shows a mean Mach number of 5.91 ±1.4%, which is less than the M of 6.0 used in the LST calculations. Given the M, T_0 and P_0 presented, the resulting Re_∞ is 2.85×10^6/ft. The quiet core length is 25.3 in. at this Re_∞ and begins 20.76 in. downstream of the nozzle throat.[34] For reference purposes, the throat-to-exit length of the nozzle is 39.76 in. In Fig. 2.3, the quiet core of the empty nozzle at $Re_\infty = 2.85 \times 10^6$/ft. is presented with the cone profile in its test orientation. It can be seen that there is a significant region where the flow over the cone is expected to be quiet. The actual noise level above the boundary layer was investigated and is presented herein.

Model position in the M6NTC was determined by trial and error in order to maximize run time. The final position of the cone resulted in 3 in. of the model extending from the nozzle exit. With the model in this position, the tunnel could run in a nearly indefinite steady-state mode at the desired stagnation temperature and pressure.

The orientation of the cone with respect to the mean flow was of great concern. Since the pressure system was not available at the time of final cone positioning, a mechanical approach was utilized. Specifically, the cone was aligned with the outer edge of the nozzle using calipers and a straight edge so that the cone was at zero degrees yaw with an error of ±0.1 degrees. Using an inclinometer, the cone was set at zero degrees angle-of-attack with an error of ±0.1 degrees.

It is significant to note that the M6NTC used in performing the present research no longer exists. The tunnel was decommissioned and dismantled within weeks of the completion of these experiments.

2.3 Hot-Wire Probes and Constant-Voltage Anemometer

To satisfy the requirements of this experiment, the author designed and built unique hot-wire probes incorporating a contact sensor as shown in Fig. 2.4. Since LST calculations predicted a boundary-layer thickness of less than 0.040 in. for the cooled case and the majority of the cone was inside the nozzle, accurate determination of the position of the probe relative to the cone wall, without optical access, was fundamental to the success of the experiment. To ascertain when the probe contacted the wall, a contact circuit was designed (Fig. 2.5) that produced a high TTL output when mechanical (and hence electrical) contact between the cone wall and contact sensor was made. All traversing motions were then made relative to this wall position. As seen in Fig. 2.4, the contact sensor was positioned far downstream of the hot-wire to minimize flow interference.

Omegabond 200 was selected as the high-temperature epoxy for securing the wire supports and contact sensor to the probe body. This epoxy proved to be rigid and durable.

The shape of the wire support tips was another unique feature of the probes. The hot-wire was 0.0001 in. dia. platinum-rhodium (10%) wire with a length-to-diameter aspect ratio of 150. This wire material and aspect ratio have been used successfully in recent high-speed stability research[86] despite its lack of strength compared to tungsten[91] and the potential for end conduction effects.[92-94] To avoid unsteady strain gaging; i.e. spurious frequencies in the time-trace data due to wire vibrations, a hot wire in high-speed flow must have some slack.[95,96] To obtain the slack, or curvature, seen in Fig. 2.4, the wire support tips were angled and the hot wire was soldered, using high-temperature solder, to the center of the support tips. This unique approach resulted in hot-wire probes with negligible unsteady strain gaging.

There were a total of 6 hot-wire probes built for this experiment that were repaired a total of 22 times due to wire breakage. During testing, there was a recurring failure mode of the wires - the resistance of the wire would steadily increase over time and the wire would ultimately break in the middle. Since there was no visible evidence of oxidation on the broken wires, it is thought that the wires were plastically deforming which resulted in a reduced diameter and hence higher resistances. The wire breakage is thought to be due to mechanical failure as each wire was stressed beyond its ultimate strength.

The constant-voltage anemometer (CVA) used in the present research is a recent invention under development by Tao Systems.[97-100] While the CVA is usually operated at constant wire voltage, the author has chosen to operate the CVA in a constant overheat mode with a resistance ratio ($R_w/R_{w,adiabatic}$) of 1.5 to minimize possible sensitivity variations due to overheat drift. The overriding reason for using the CVA was its low noise level while operating in the M6NTC environment. Constant-temperature anemometry and constant-current anemometry systems have been used previously in the M6NTC, but neither have the low noise level and hence, high signal-to-noise level, of the CVA. The

CVA used in the present study was a Tao Systems prototype Model CVA400 with a bandwidth of 400kHz, which is well-suited for detecting the highest predicted second mode frequencies of 310 kHz. The sensitivity of the CVA (in the constant voltage vs. constant overheat modes) to flow disturbances is addressed herein.

In Fig. 2.6, the typical no-flow noise spectra of the CVA is compared to a typical hot-wire spectra with the wire located in a low-disturbance region of the adiabatic-cone boundary layer. This figure illustrates the lack of unsteady strain gaging typical of the hot-wire probes used. Unsteady strain gaging would be seen as large amplitude spikes usually above 500 kHz. Noting that the frequency amplitudes are on a logarithmic scale, the roll-off of the no-flow noise output near 400 kHz is evident. This defines the bandwidth of the CVA. It is also worthy to note that the lower frequencies (e.g., 15 kHz) have lower absolute noise levels than the second mode frequencies (e.g., 310 kHz) indicating that these lower frequencies can be detected before the second mode frequencies.

No attempt to calibrate the hot wires was made for a number of reasons. First, static calibration would have greatly increased the experimentation time beyond the scheduled decommissioning date of the M6NTC. Secondly, the wire failure rate showed that a calibrated wire would be useful for only a limited time. Thirdly, the range of flow conditions available for calibration purposes was limited, which meant that it would not be possible to quantify most of the boundary-layer mean flow. In addition, the static response of a hot-wire in high-speed flow using CVA has not yet been studied rigorously. The author is aware of research presently being conducted at Syracuse University to analyze and experimentally verify the static and dynamic response of a constant-voltage anemometer in high-speed flow. Finally, and most importantly, the highest priority of the present research was to determine the stability of the flow and uncalibrated data were sufficient to glean the dominant frequencies and their growth.

2.4 Traversing System

A schematic of the conical model in the M6NTC is presented in Fig. 2.7 with the dashed lines indicating the location of the thermocouples (flow data were acquired in the plane of the thermocouples). Note the distance between the nozzle exit and the diffuser inlet in Fig. 2.7. This tunnel dimension imposed the tightest constraint on the design of the traversing arm and the maximum length of cone traverse in the x-direction. A typical x-traverse of the cone boundary layer was limited to 7.5 inches. A schematic of the traversing arm is presented in Fig. 2.8. It was designed to accept the interchangeable hot-wire probes while minimizing deformation under flow loading. The traversing arm experienced no problems associated with deformation or other phenomena during the tests. The coordinate system used in this research is also presented in Fig. 2.7. The x-axis begins at the cone tip and coincides with the cone axis. The y-axis is normal to the x-axis and parallel to the tunnel floor. The y-distance is always taken relative to the cone surface at a specific x-location. The traversing arm was attached to two computer-controlled linear motion traverses mounted on the ceiling of the tunnel -- one for the x-direction and the other for the y-direction. These traverses moved 12,700 steps per inch of motion with errors of ±0.00039 in.

Throughout this work, the x-direction is the coordinate of interest, whereas in the LST calculations, "S" or distance along the surface of the cone is used. In Fig. 2.9, the difference between the two coordinates is presented and at the maximum x-location (x=18.00 in.) the corresponding S location is S=18.18 in. This 1% difference is negligible and hence the experimental data can be compared using the x-coordinate.

The curvature of the cone presented some difficulty upon attempts to traverse a constant y-location over the cone. The software was designed so that constant heights between the contact sensor and the cone could be investigated. Since the hot wires are not positioned directly over the contact sensor (see Fig. 2.4), a systematic error exists in the y-location of the wire as x is varied. In Fig. 2.10, the appropriate correction distance is presented so that the true y-location of the hot wire can be determined. Since the traversing arm is fixed at an angle of 13.1° with respect to the x-axis and the curvature of the cone increases with x, the y-correction increases with x. The net effect of this systematic error in y is that a "constant y" traverse actually follows a line of slightly increasing y as x increases. Unless otherwise noted, all y-values presented are uncorrected and the random y position error is ±0.0025 in. which is ±1/2 the hot-wire support diameter. This error represents the uncertainty in centering the wire directly along the center of the supports.

2.5 Data Acquisition System

The fully automated data-acquisition system (driven by a C-program executed on a 486-DX33 PC) is depicted in Fig. 2.11. The C program was designed so that experimental grids could be traversed over the cone in uniform x- and y-steps. The program controlled all motions of the traverse in conjunction with the contact switch output. Generally, the traversing arm moved to the first x location and then moved the hot-wire probe toward the cone in single step increments. Upon making contact with the cone surface, the traversing movement stopped and then reversed direction until the first y location was reached. After a predetermined "wait" time (on the order of milliseconds), the appropriate data were acquired and stored on the PC. This sequence of moving, waiting, and then acquiring data was repeated until the grid was covered.

The time-trace data were acquired using a Nicholet Pro 40 digital oscilloscope with a sampling rate of 2 million points per second and record length of 2^{17} points. The oscilloscope was used primarily because it had an amplitude resolution of 12 bits; i.e., the full-scale range is divided into 4,096 bins. Since the amplitude of the unsteady data increased exponentially with x, a software routine was developed to optimize the amplitude scale at a suitable level prior to acquiring each time trace. The CVA time-trace data were first AC-coupled and filtered using a Stanford Research Systems model SR560 low-noise preamplifier with a low-pass filter setting of 1 MHz, a high-pass filter setting of 100 Hz, and a gain of 1. The high-pass setting was selected to help minimize the 60 Hz facility noise and the low-pass setting was selected based on the Nyquist criteria; i.e., 1/2 the sampling rate. The roll-off of the Stanford filter was only 6 dB per octave, but other available filters with higher roll-offs were found to introduce spurious frequencies and large noise levels when the signal amplitude was small. To help minimize the electrical noise further, the CVA power supplies were connected to a Topaz Line Noise Suppressing Ultra-Isolator.

While testing, a LeCroy digital oscilloscope was used to monitor the filtered CVA output so that hot-wire failure could be readily determined. The LeCroy oscilloscope was also used as a spectrum analyzer so that the quality of the hot-wire signal could be evaluated. This was especially useful in making immediate determinations about any unsteady strain-gaging behavior of the wires. It should be noted that the LeCroy oscilloscope, while exhibiting a faster sampling rate than the Nicholet model, had only 8-bit amplitude resolution; i.e., 256 bins, meaning that the quantization error with the Nicholet oscilloscope was significantly less. Moreover, the Nicholet oscilloscope could store records 3 times longer than those available using the LeCroy.

To set the voltage across the hot wire, a programmable Hewlett-Packard model 59501B power supply was used. With this device, voltages from 0.01 to 9.99 V could be selected as the V_{rh} input to the CVA, with an error of ±0.01 V. Voltage selection was done via a function in the main data acquisition program used to set the wire overheat.

A Keithley Model 199 System Digital Multi-Meter/Scanner was used to measure mean and RMS quantities from the CVA. With this device, "true" RMS measurements could be made as well as DC-voltage and wire resistance measurements. All data acquisition instructions via the Keithley were computer-controlled and data were stored on the PC.

The M6NTC also had a Schlieren system available. To record images of the flow over the last 3 in. of the cone, a Panasonic Model AG-7300 video cassette recorder was used and continuous images were stored on standard videotape. Since most of the cone was inside the nozzle, these images only show the flow phenomena associated with the end of the transition zone.

Data from the instrumented cone were also collected. A Hewlett-Packard Model 3852A Data Acquisition and Control Unit (DACU) was used to acquire the voltages from the cone thermocouples and from the resistance temperature devices used to establish the reference temperature. Thermocouple voltage data from the DACU were transferred to the PC, converted to temperatures and stored. There were nine Baratron 10-Torr pressure transducers used to measure surface pressures on the cone. The voltage data from the pressure transducers were converted to pressures by an MKS Instruments, Inc. Type 670 Signal Conditioner and the data were recorded directly from the display.

2.6 Measurements

A review of the data acquired during this research is now presented.

The focus of stability experiments is on the frequency components in the unsteady data, so most data acquired was the AC-coupled output of the CVA. For each time trace acquired, the necessary quantization parameters were also recorded in a separate file. These files contained such information as the sampling rate, full-scale range, and the conversion factor to recover voltages from the binary time-trace data.

In order to determine the location of maximum disturbance energy, the RMS of the CVA output was recorded as the wire passed through the cone boundary layer. These data were acquired with the CVA in its constant-voltage mode (V_{th}=5.0V) to minimize test time. The location of maximum RMS energy is traditionally where unsteady data is acquired in a stability experiment, due to the large measurable disturbance amplitudes.

Since a traditional total temperature probe would cause too much interference in the 0.040-in. boundary layer over the cooled cone, the unheated hot wire was traversed through the boundary layer and the mean resistances recorded. In this mode, the hot wire responded only to mean total temperature and the final resistance indicated the adiabatic wall temperature of the wire. These resistance data were used to determine the thickness of the thermal boundary layer and to indentify mean-flow distortion.

A heated wire, on the other hand, responds to changes in total temperature, mass flow, and overheat. The DC voltage of the CVA output was recorded as the hot wire was traversed through the boundary layer with the CVA in its constant voltage (V_{rh}=5.0V) mode to minimize test time. These data were also used as a qualitative indication of mean-flow distortion and as another means of determining boundary-layer thickness.

The wall temperature of the cone was determined from the T-type thermocouples and is traditionally used as the indicator of boundary-layer transition. Wall static pressure data were obtained in the flared region of the cone using 9 of the 30 orifice locations on the cone surface and are compared herein to the theoretical calculations for the laminar boundary layer.

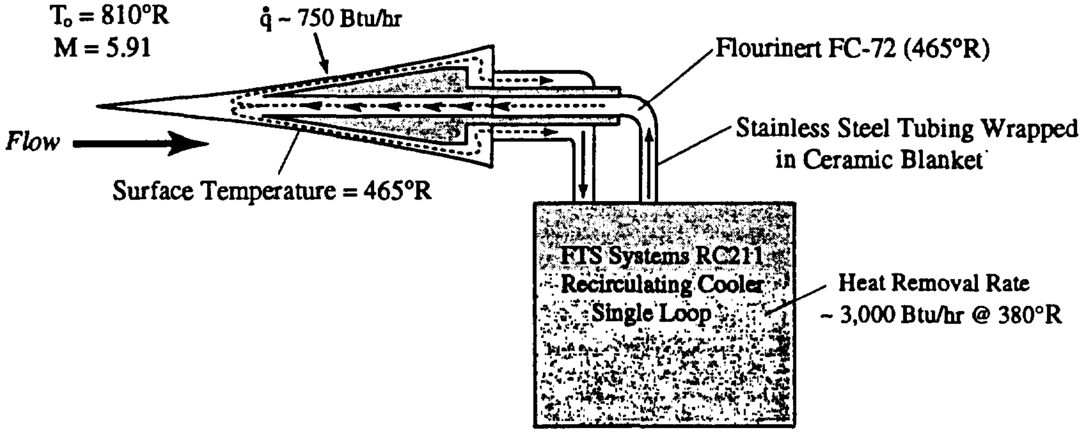

Figure 2.1 Active Cooling System for the Cooled Cone

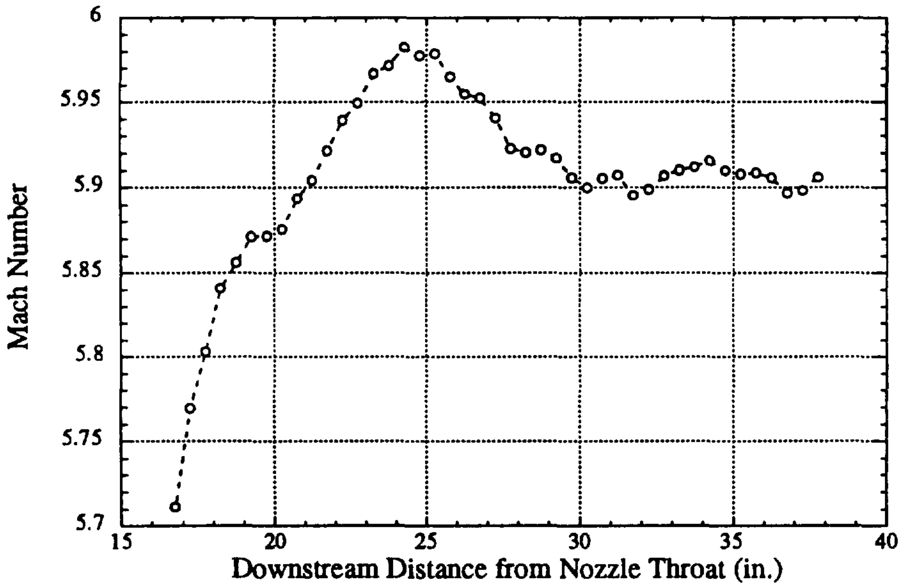

Figure 2.2 Centerline Mach Number of the M6NTC at $Re_\infty = 2.85 \times 10^6$ /ft.

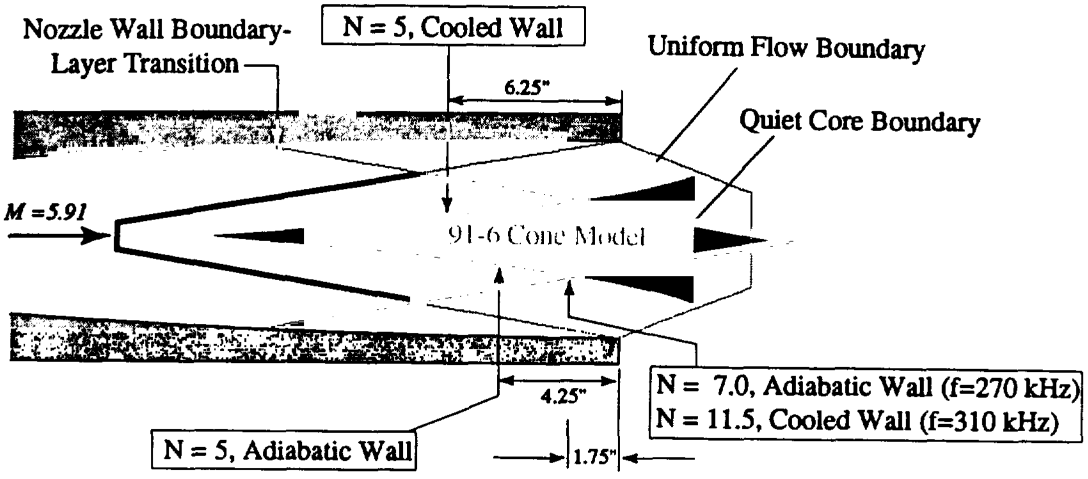

Figure 2.3 Cone 91-6 in M6NTC with Quiet Core

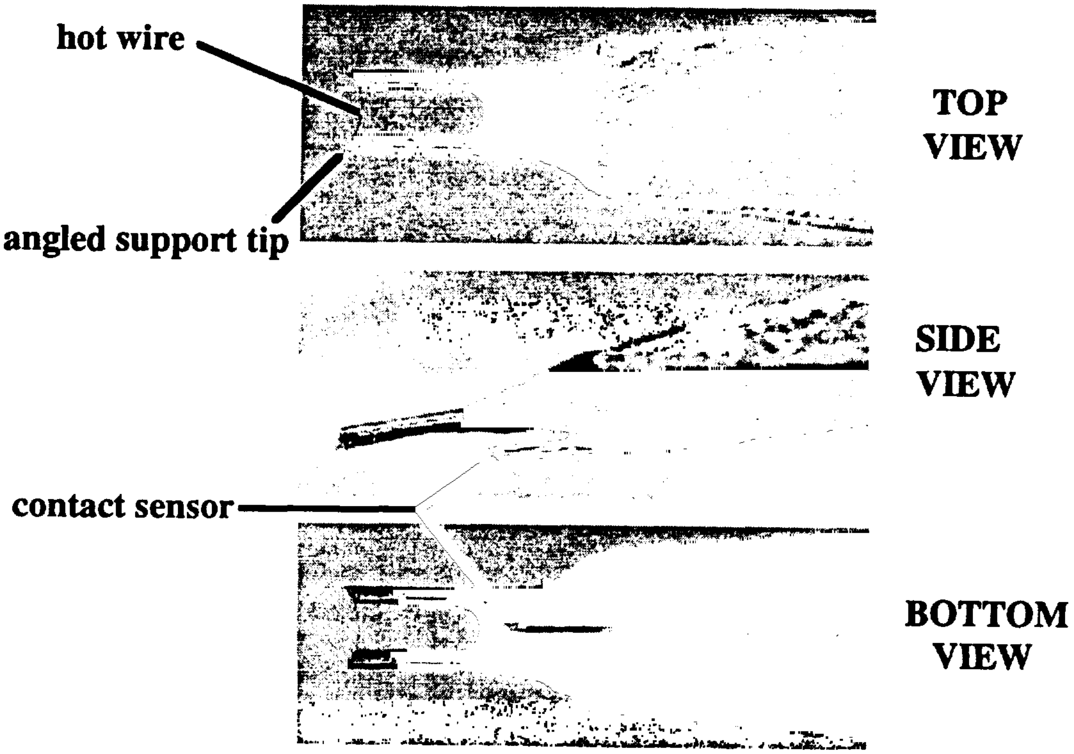

Figure 2.4 Custom Hot-Wire Probes

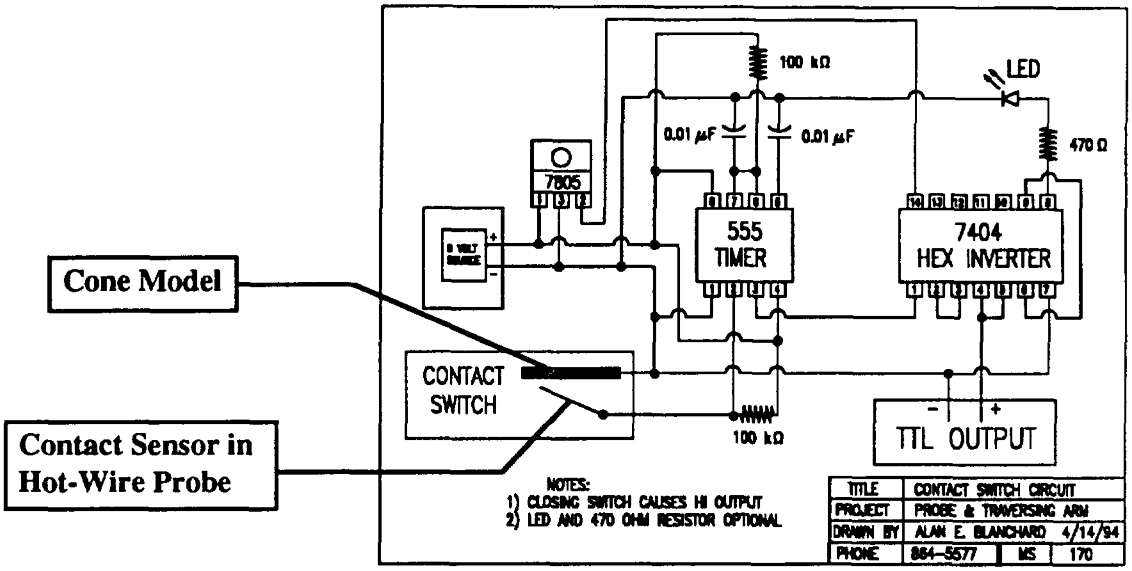

Figure 2.5 Contact Circuit Schematic

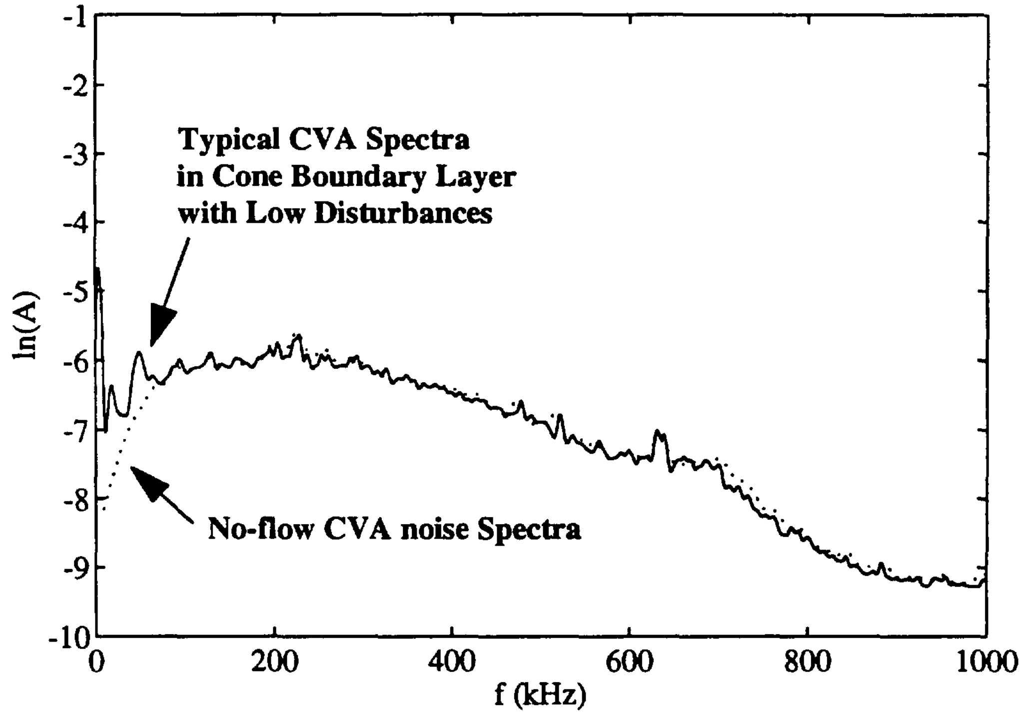

Figure 2.6 CVA Noise Spectra and Hot-Wire Low-Disturbance Spectra

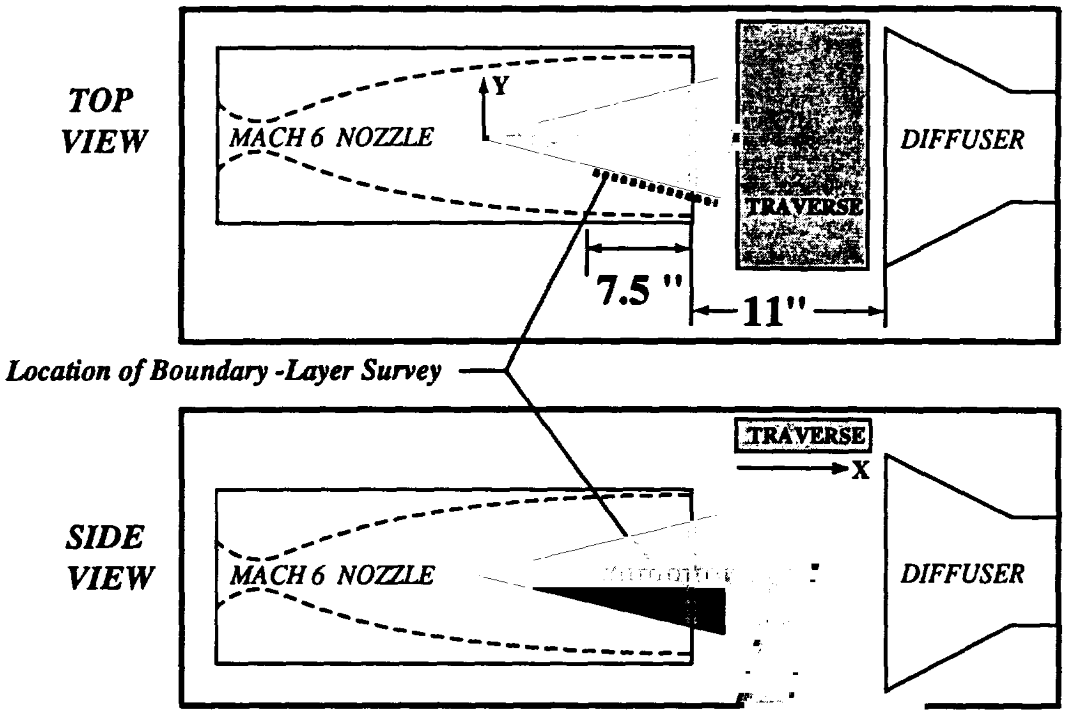

Figure 2.7 Traversing Line over Cone and Coordinate System

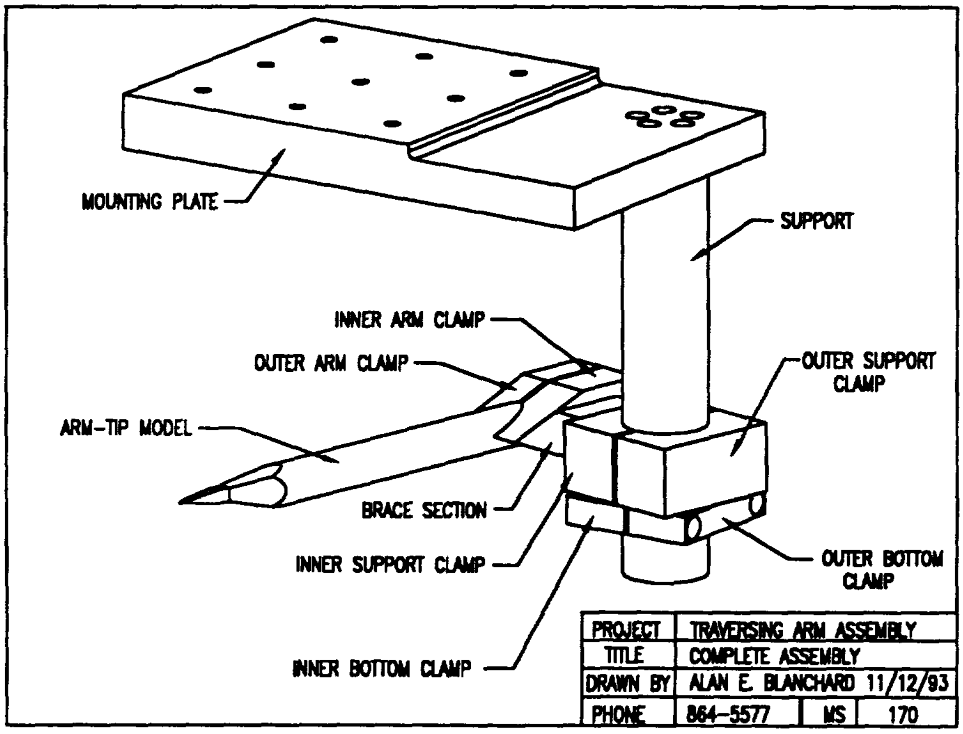

Figure 2.8 Traversing Arm

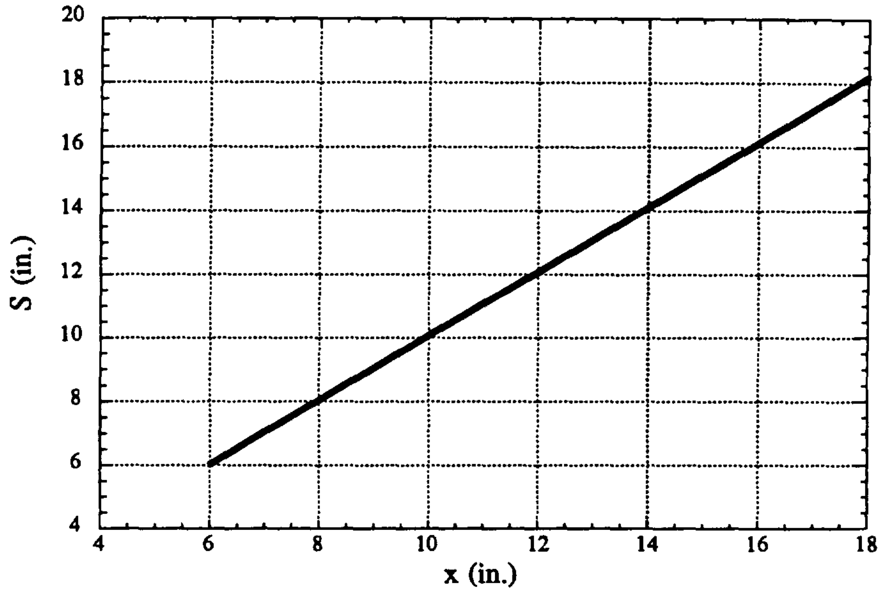

Figure 2.9 Comparison of "S" versus "x" coordinates

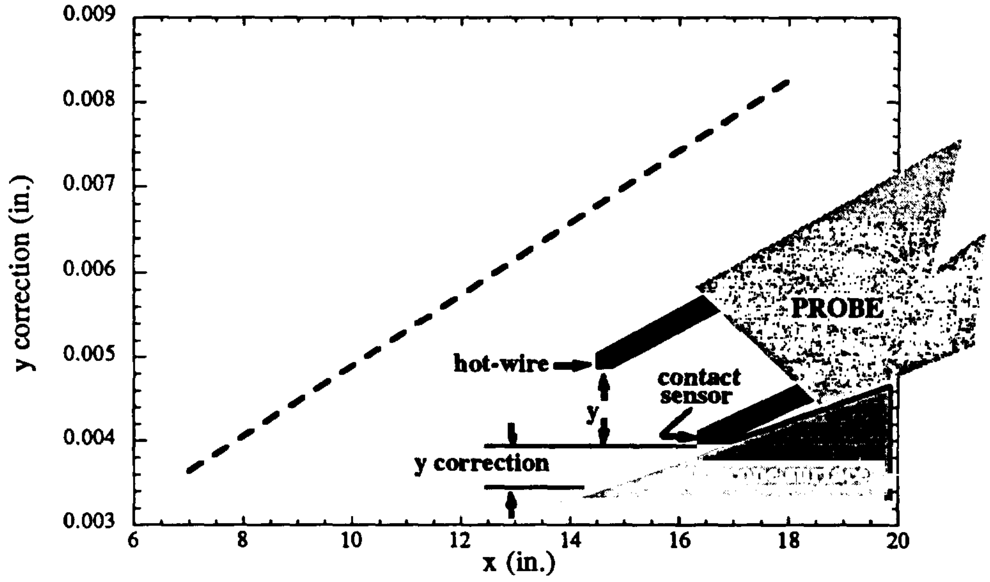

Figure 2.10 Correction Chart for Experimental "y" values

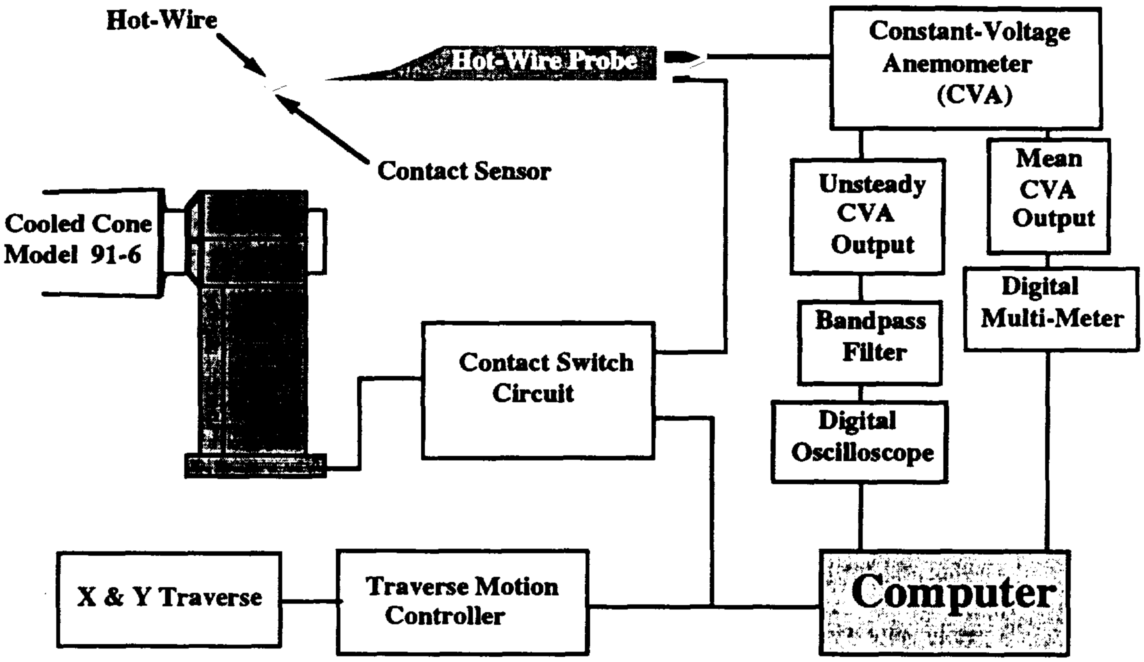

Figure 2.11 Schematic of Data Acquisition System

CHAPTER 3

FREESTREAM DISTURBANCES

3.1 Overview of Freestream Disturbance Spectra

One of the unique features of the present research is that the stability of the cone boundary layer has been investigated in a quiet flow environment. As discussed earlier, conventional tunnels have turbulent tunnel wall boundary layers which radiate eddy mach-waves into the freestream. This freestream noise impinges on the model boundary layer and introduces unwanted, transition-promoting disturbances.[24,25] Quiet tunnels are designed to minimize acoustic radiation and hence allow the model boundary layer to develop in a manner that more closely resembles that predicted by linear stability theory.

To investigate the freestream flowfield, the region 0.24 in. above the model was surveyed from x=9 in. to x=16.5 in. at the test flow conditions of T_0=810°R and P_0=130 psia. The cone was cooled for this test to 537°R, the minimum cooling temperature of the system. However, for this type of test, the wall conditions of the cone were immaterial. The maximum cone boundary-layer thickness for all tests was 0.050 in.; so, the survey was at least 4 boundary-layer thicknesses away from the wall. The cone angle over the straight section of the cone was 5°. Hence, inviscid theory predicts a shock 0.64 in. above the surface of the cone at x=6 in.[99,100] Since the cone shock will not decrease in distance away from the cone as x increases, it is clear that the survey at y=0.24 in. was between the cone shock and the cone boundary layer .

For each spectra presented, the 2^{17} data points were divided into 2^8 records and averaged using an FFT length of 2^{10}. Due to the window length in the power spectral density (PSD) routine, the frequency amplitudes below 10kHz were suspect and were not presented. Since the focus of the subject research was on frequencies much greater than 10kHz, this was of little consequence. The units of the amplitudes of the PSD curves are $(\text{volts})^2/\text{Hz}$ and all amplitudes presented herein are the square root of this parameter. This spectral analysis routine was applied to all the unsteady data herein.

In Fig. 3.1 the freestream spectra are presented at y=0.24 in., x=9 and 16.5 in. There are two generic features of freestream noise[81] illustrated by the "noisy" flow curve at x=16.5 in.: 1) the lowest frequencies have the highest amplitude and 2) noise amplitudes rapidly diminish as the frequency increases. This "noisy" flow curve is typical of the freestream spectra associated with conventional tunnels. The quiet flow curve at x=9 in. is unique to quiet tunnels operating at this unit Re_∞ and can be produced in conventional tunnels only when Re_∞ is reduced.

In Figures 3.2 and 3.3, the development of the "noisy" flow is presented in terms of a series of spectral plots for the x-locations investigated. From Fig. 3.2, there is no evidence of disturbances in the flow until x=12.5 in., and this "noise" only appears in the lowest frequencies. Although the flow upstream of x=12.5 in. may contain disturbances, they could not be detected with the present measuring instruments. In Fig. 3.3, there is an anomaly in the data in the vicinity of 220kHz and x=15.5 in., but this phenomena was not found to be repeatable and does not impact the estimation of the quiet region. However, the general trends of the spectra presented in Figures 3.2 and 3.3 are repeatable.

3.2 Low-Frequency Disturbances

The dominance of low-frequency disturbances in the freestream of the M6NTC is evident. In Fig. 3.4, disturbance amplitude at selected low frequencies has been plotted as a function of x, with polynomials fitted to the data points. Since the lower frequencies have lower noise levels, each data set has been normalized by the value of A_0 at x=9, the furthest upstream location. The logarithm of the amplitude ratio is presented in Fig. 3.4

since the unsteady data in the cone boundary layer is presented in terms of this parameter in later chapters. It is clear that the maximum disturbance amplitude is associated with the lowest frequency. As frequency increases, maximum amplitude diminishes, with the amplitude profile for 100kHz barely rising above zero. The amplitude increase with x was due to increased radiation intensity as the nozzle wall boundary layer evolved from transitional to turbulent. The transition zone of the nozzle wall boundary layer is thought to be characterized by the formation, growth, and breakdown of Görtler vortices.[33]

For the present research, the most important low-frequency disturbances are at 70kHz which is the most unstable first-mode frequency predicted for the adiabatic cone case.[14] As seen in Fig. 3.4, the amplitude profile for a frequency of 70 kHz does not become nonzero until x>14 in. and its amplitude is much less than for the 15kHz case. The importance of these low-frequency disturbances is that they can potentially enter the cone boundary layer and trigger the growth of first-mode instabilities.

3.3 High-Frequency Disturbances

The amplitudes of the high-frequency disturbances are presented in Fig. 3.5. The frequencies presented are the most unstable second-mode frequencies predicted by LST, and the subharmonics of these modes. The same vertical scale used in Fig. 3.4 is also used in Fig. 3.5 to emphasize the fact that no high-frequency disturbances in the freestream increase appreciably above the reference level.

3.4 M6NTC Flow Quality

The M6NTC produced a substantial region of high-quality "quiet" flow over the cone model. There were no measurable second-mode frequencies in the freestream at y=0.24 in. above the test cone in the orientation used for testing. There was a first-mode frequency in the freestream, but it was only measurable for x>14 in. Moreover, there were no measurable disturbances for x<12.5 in., indicating that the flow over the cone was "quiet" up to that point. "Quiet" flow does not necessarily imply "noiseless" ideal flow. There may have been disturbances in the freestream whose amplitudes were so small as to escape detection, but the traditional acoustic disturbance levels typical in a conventional tunnel were absent for x<12.5 in.

In Fig. 2.3, the quiet core determined from the empty tunnel calibration[31] predicted that disturbances would first radiate onto the cone boundary layer at x=13.25 in. which is slightly downstream of x=12.5 in., as determined from Fig. 3.2. This difference can be attributed to the fact that the freestream disturbances of Fig. 3.2 were located at least 0.19 in. above the boundary layer. If the trajectory of the disturbance from y=0.24 in. is considered, the x=13.25 delineation between "quiet" and "noisy" flow was reasonable. Then, x=12.5 in. is a conservative estimate of the end of the quiet region.

While a significant region of quiet flow was expected, there remained the question of whether or not the flow disturbances would be measurable in the quiet region. Referring to Fig. 2.3, the second-mode growth for the adiabatic wall case is N=7 at the location where measurable freestream disturbances radiate onto the cone boundary layer. Since the growth of second-mode disturbances in the cooled case is even higher, the potential exists for measurable disturbances to grow in the cone boundary layer while the boundary layer is in the quiet core of the M6NTC.

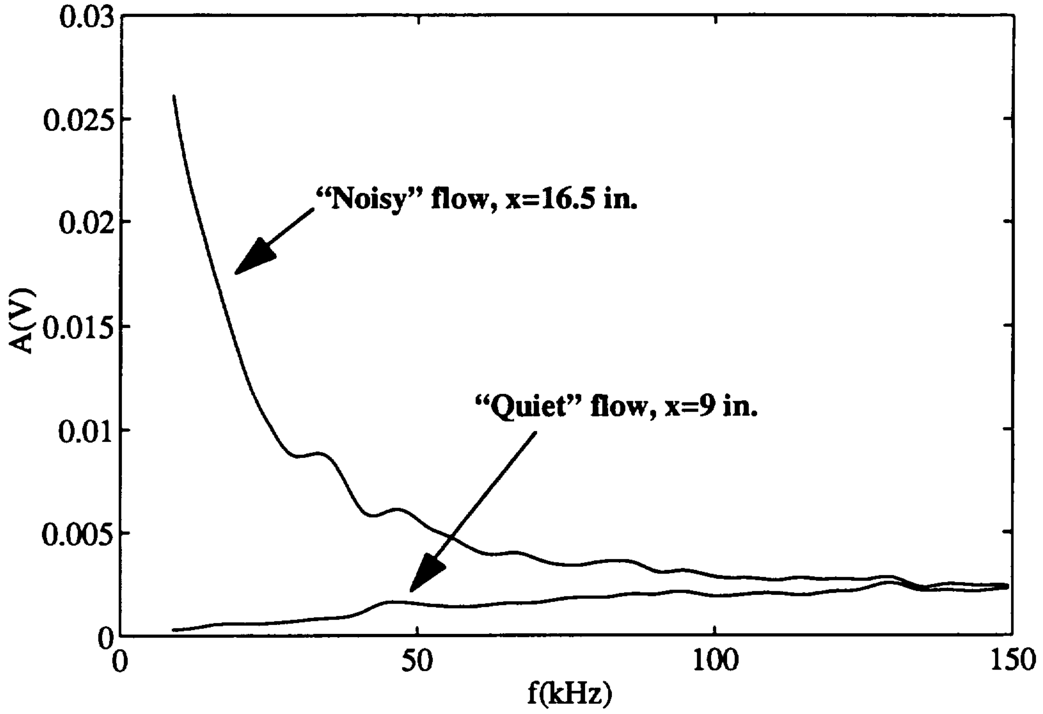

Figure 3.1 "Quiet" and "Noisy" Flow at y = 0.24 in.

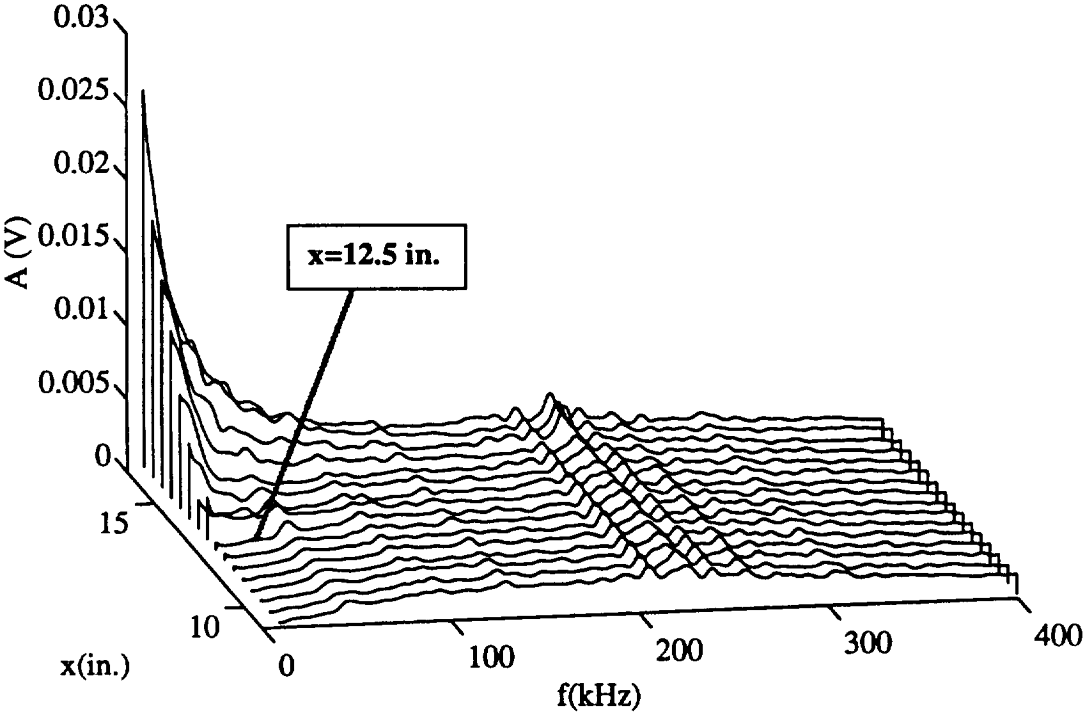

Figure 3.2 Freestream Spectra at y = 0.24 in.

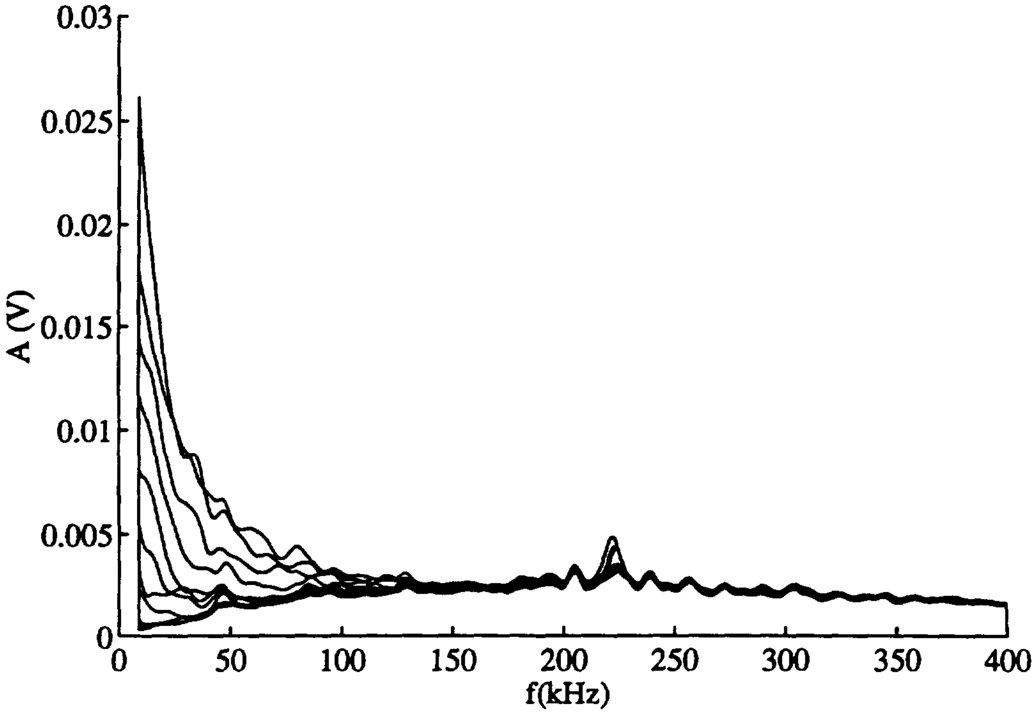

Figure 3.3 Front View of Fig. 3.2 data

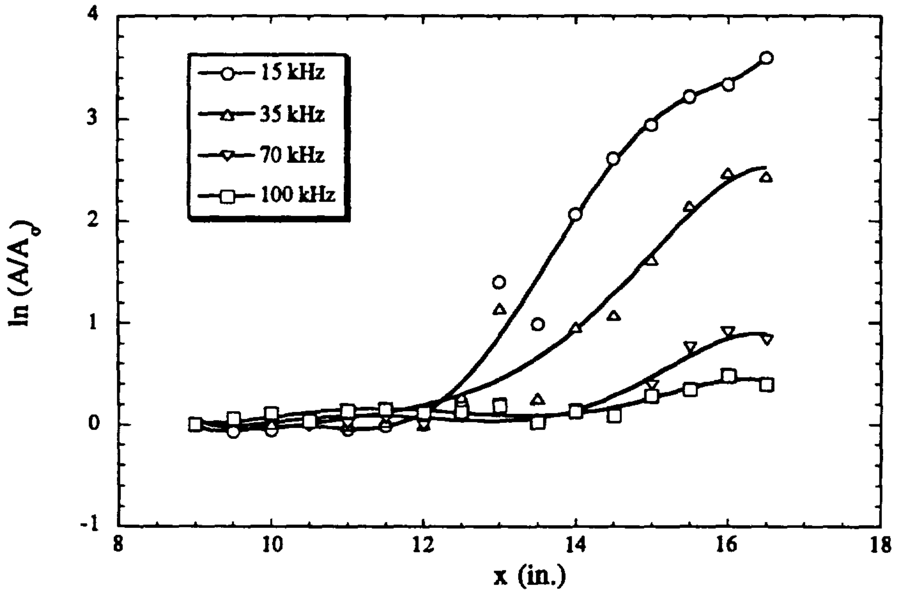

Figure 3.4 Low-Frequency Disturbances in the Freestream

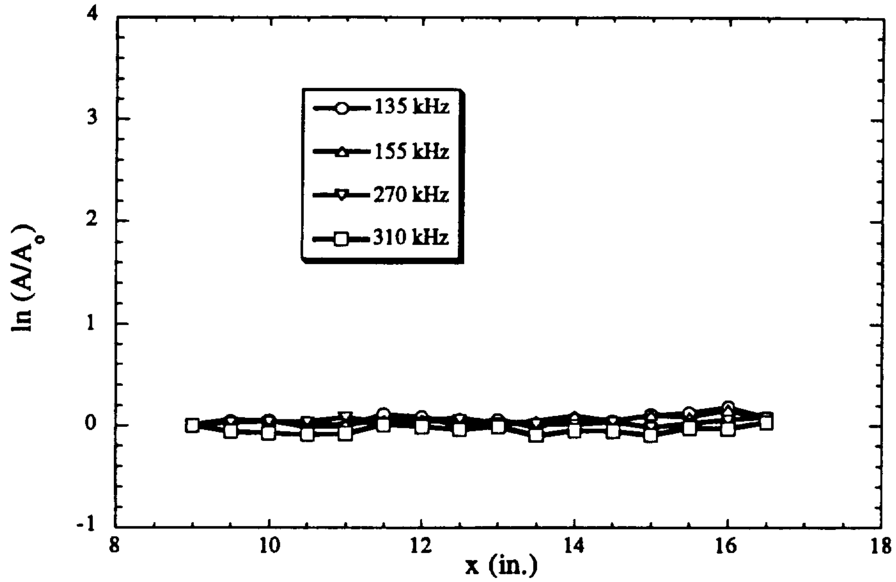

Figure 3.5 High-Frequency Disturbances in the Freestream

CHAPTER 4

ADIABATIC-CONE MEASUREMENTS

4.1 Adiabatic-Cone Wall Temperature

One of the simplest ways of identifying the transition zone over a model in high-speed flow is through the use of temperature data from thermocouples mounted just under the surface of the model. As the boundary layer undergoes transition, the heat transfer coefficient increases from its laminar value to a higher turbulent value and thermocouples mounted directly under the surface of the model indicate the increased heat transfer rate through an increase in wall temperature.[36]

In Fig. 4.1, the wall temperature distribution on the adiabatic cone is presented and the dramatic increase in wall temperature due to the presence of transitional flow is apparent. For each test of the adiabatic cone, the model was "pre-heated" with a flow of high-density, high-temperature air for approximately 1/2 hour. Once the flow conditions were met (Mach 6, P_0=130 psia, T_0=810°R), the cone model was allowed to reach a repeatable steady-state wall temperature before data were acquired. Due to the extensive preheating, the "wait" time for this temperature distribution at flow conditions was minimized (between 10 and 15 minutes). The data in Fig. 4.1 are an average of the wall temperatures recorded for 18 separate tests conducted on the adiabatic cone. The standard deviation of the temperature at any wall location was less that 1% for all the adiabatic wall tests. The coolant passages in the cone model were evacuated for these tests.

A typical transition zone can be identified in Fig. 4.1. The intersection of two lines, one approximating the slope of the laminar wall temperatures and the other the slope in the high temperature-gradient region, gives an indication of the start of the transition zone. The end of the transition zone, or "transition point," can be equated with the location of maximum wall temperature as shown.[14] Of course, the transition process occurs over a region and the definition of a transition "point" is somewhat arbitrary. In general, the wall temperature data in Fig. 4.1 show that a transition zone exists over the adiabatic cone between x=12 and x=16 in. This is only a rough estimate of the extent of the transition zone, but it does indicate where the initial hot-wire surveys should be conducted.

4.2 Mean Boundary Layer Over the Adiabatic Cone

To help determine the state of the adiabatic-cone boundary layer, surveys of the boundary layer were conducted with an unheated hot wire. Since the resistance of the unheated hot wire increases linearly (as a first approximation) with total temperature, the resistance of the hot wire was recorded as the wire was surveyed through the boundary layer. In Fig. 4.2, the resistance profile of the wire, normalized by the value at $y=y_{max}$, is presented at x=9 in.. This R_w curve has the characteristics of a typical stagnation temperature profile in a high-speed boundary layer with a "bulge" in T_0 near the boundary-layer edge due to frictional heating.[103] Since T_0 will reach a constant value outside the boundary layer, the boundary-layer thickness is estimated to be 0.055 in. at x=9 in. Note that the thinness of the boundary layer precluded the use of a standard T_0 probe, which could have caused excessive flow interference due to its size.

All of the normalized R_w data are presented in the form of a contour plot in Fig. 4.3. The line defining the value of unity may be considered the edge of the boundary layer as was shown in Fig. 4.2. This line actually defines the thermal boundary-layer thickness, since the mean-flow analysis associated with the LST predictions[14] show that the temperature continues to vary slightly after the velocity has reached the freestream value. In boundary-layer theory, in general, and in the LST calculations specifically, the velocity and temperature profiles are shown to change slowly with x. Hence, in the R_w data presented in Fig. 4.3, this slow variation translates into a series of parallel contour lines with a slight slope between x=9 and 13.5 in. For x>14 in., there is a dramatic change in the R_W profile that suggests a distortion of the mean flow from its laminar state.

A second method of determining boundary-layer thickness and mean-flow distortion was employed. The heated wire was surveyed through the boundary layer and the mean response of the CVA was recorded. In this test, the CVA was operated at a constant wire voltage with V_{rh}=5.0V to minimize test time. The mean CVA output voltage of the heated hot wire, $V_{s,mean}$, responds to changes in mean mass flow, mean total temperature, and overheat. Again, the flow variables, as well as the wire overheat, vary slowly in x for a given y location, so parallel lines with a slight slope would be expected in the laminar region. In Fig. 4.4, the mean CVA response to the heated wire, normalized by the y_{min} and y_{max} values at each x location, is presented in contour plot form. In this case, the line defining the normalized value of 0.99 is used as the location of the boundary-layer edge. As was the case for the unheated hot wire data in Fig. 4.3, the heated hot-wire data in Fig. 4.4 also show a distortion of the mean flow for x>14 in., as evidenced by the deviation of the contour data from a family of parallel lines.

The boundary-layer thickness data as defined previously, is compared to the LST prediction in Fig. 4.5. The general trend of the experimental data matches well with the numerical prediction for the laminar, adiabatic-cone boundary layer. For x>15 in., the experimental data is seen to deviate from the laminar prediction. This deviation is expected as the transitional boundary layer evolves and grows.

The wall pressure data in the transition zone were also recorded for the adiabatic cone and are presented with the LST predictions in Fig. 4.6. Although the data are sparse, the overall trend matches well the predicted value and gives further confidence to the experimental results. It should be noted that the wall pressure data for locations x=13 in. and x=16 in. are suspect since the wall pressures were still changing (decreasing) even after 1 hour .

Upon considering all the mean-flow data presented in Figures 4.1-4.6, the behavior of the adiabatic cone boundary layer may be deduced. Up to x=15 in., the boundary-layer thickness stays relatively constant and compares well with the numerical prediction. The results of the heated and unheated wire survey suggest that the boundary layer begins to distort significantly at x>14 in., and this is followed by an increase in boundary-layer thickness at x>15 in. Hence, it may be concluded with reasonable certainty that the adiabatic cone boundary layer is laminar for x<14 in. and that the mean flow has undergone a significant distortion by the time the "transition point" has been reached at x=16 in., as shown in Fig. 4.1.

4.3 Overview of Adiabatic-Cone Disturbances

The disturbances in the adiabatic-cone boundary layer were measured at the location of maximum disturbance amplitude, as is standard practice in high-speed stability experiments.[86] To determine the location of maximum disturbance energy, the heated hot wire (using a constant voltage setting of V_{rh}=5.0V to minimize test time) was traversed through the adiabatic-cone boundary layer and a digital multimeter was used to measure the output of the anemometer in terms of $V_{s,RMS}$. In Fig. 4.7, the RMS data at x=9 in. is presented versus the y distance normalized by the boundary-layer thickness as defined in Fig. 4.5. The maximum value of $V_{s,RMS}$ occurs near the boundary-layer edge at y/δ=0.87, which is typical of second-mode disturbances, as seen in previous high-speed experiments.[86] The amplitude of the disturbances is seen to diminish rapidly to a constant "zero" value outside the boundary layer at this x location. Note also that there is a second maximum at y/δ=0.58, but the spectral content of this peak did not differ from the peak at y/δ=0.87. This second peak may result from an increasing hot-wire sensitivity combined with decreasing disturbance amplitude, as y/δ decreases.

All of the aforementioned RMS data are presented in a contour plot in Fig. 4.8 with the hot-wire survey path identified. For this plot, the natural logarithm of the RMS values was first taken and then the data were spatially filtered using a low-pass routine to minimize experimental noise. As shown in Fig. 4.8, the path of the hot wire used to record the disturbance spectra coincided with the nominal location of maximum RMS energy, to within the experimental error of +/- 0.002 in. Also observed in Fig. 4.8 is the distortion of the RMS contours for x>14 in., which coincides with the previously identified region of mean-flow distortion.

In Figures 4.9, 4.10, and 4.11, the spectral content of the timetrace data acquired at the location of maximum disturbance energy for the adiabatic cone are presented in an oblique-view waterfall plot, a front-view waterfall plot, and a contour plot, respectively. The value of A_0 used for normalizing each frequency was the value measured at x=9 in.--the most upstream location. For each timetrace, the hot wire was heated to R_w=1.5 $R_{w,adiabatic}$. As shown in the figures, there are three distinct peaks in the spectra centered about zero, 280, and 560kHz. It should be noted here that the bandwidth of the anemometer is 400kHz, which implies that the amplitude data for frequencies above 400kHz have been attenuated.

4.4 Second-Mode Disturbances Over the Adiabatic Cone

From the LST calculations, the most unstable disturbance in the adiabatic-cone boundary layer are second-mode disturbance at 270kHz . There exists a band of unstable frequencies in the experimental data which include this predicted second mode. In general, second-mode disturbances are highly tuned to the thickness of the boundary layer, and the band of unstable second-mode frequencies in Fig. 4.10 is nearly constant since the boundary-layer thickness in this case is approximately constant prior to transition (see Fig. 4.5). This result greatly simplifies the analysis because there is no shifting of the unstable frequencies which is typical for a straight cone.[76]

To identify individual second-mode frequencies, a segment of a single spectrum is presented in Fig. 4.12 at x=13 in. It can be seen that there are two dominant second-mode frequencies at 275 and 291 kHz, rather than a single dominant frequency. Changing the parameters of the power spectral density routine to refine the spectrum only made these two peaks more pronounced. It is known that "natural" second-mode disturbances in a hypersonic boundary layer occur in wave packets[104] which suggests that the two frequencies identified in Fig. 4.12 could be indicative of the wave-packet nature of the flow disturbances in this case.

In Fig. 4.13, the growth of the second-mode disturbances is compared to the LST predicted growth of 270kHz. As discussed in Sec.1.4, experimental stability data can be compared to numerical calculations though Eqn.1.6a or Eqn.1.9. An attempt was made to use the traditional approach whereby a curve was fit to the experimental amplitude data and Eqn.1.3a was applied. It was found that a 7th or higher order polynomial was required for a suitable fit and that in the region of "small" amplitudes near the electronic noise level, the resulting values of $-\alpha_i$ oscillated wildly. Moreover, different curve-fit routines produced dramatically different spatial growth rates for the small amplitude data. Because of the bias introduced by the selection of the curve-fit routine, Eqn.1.9 was used for comparing the experimental data with the LST predictions.

There are two regions where the experimental amplitudes deviate from the predicted growth in Fig. 4.13. At the low amplitude end where $N=4.8$, the noise level of the CVA defines the smallest disturbance that can be detected. The shift of 10.75 required for the experimental data to be comparable to the predicted levels implies that the initial amplitude of the second-mode disturbance could be as little as $\exp(-10.75)$; i.e., $20\mu V$ (RMS) at $x=4$ in. Clearly, more sensitive experimental methods and/or equipment are required if the significant region below $N=4.8$ is to be investigated. As the second-mode disturbances rise above the noise level, N factors for both frequencies (275 and 291 kHz) are seen to follow the predicted "linear" growth up to $N=9$. For $x>15$ in., the second-mode disturbances have achieved their maximum growth and have saturated. An underlying assumption of the LST prediction is that the disturbance amplitude is negligibly small, but reality dictates that the disturbances will ultimately reach a finite level that violates this premise. It is then expected that the unstable disturbances will saturate and that other "nonlinear" processes such as mean-flow distortion and harmonic generation will appear.[2] Thus, there is a significant "linear" region in the adiabatic cone boundary layer where second-mode frequencies follow the growth predicted by linear stability theory.

4.5 Second-Mode Harmonics Over the Adiabatic Cone

While the linear growth of second-mode disturbances dominates a significant portion of the transition zone, the processes that ultimately lead to turbulent flow are nonlinear and evidence of nonlinearity is present in the adiabatic-cone boundary layer. Mean flow distortion, an inherently nonlinear event, has already been discussed in Figures 4.3 and 4.4 at x>14 in. More evidence of nonlinearity is the generation of harmonics as shown in Figures 4.9 to 4.11 by the existence of the frequency band at 560kHz. In other high-speed experiments, it has been shown that frequencies twice the second-mode frequency are true harmonics and not just fortuitous spectral anomalies.[105] Hence, the frequency band at 560kHz is assumed to be a harmonic band related to the second-mode instabilities.

In Fig. 4.14, the amplitudes of the fundamental second-mode frequencies and their harmonics are compared. There is a significant region at x<13.5 in. where the fundamental disturbances are growing linearly and there exists no measurable harmonics. Disturbances at the harmonic frequencies, which begin growing at x=13.5, cannot be explained by linear stability theory. In addition, the mere presence of these harmonics suggests the end of the linear region and the start of the nonlinear region. These harmonics are seen to grow and saturate at about the same location, x=15 in., where the fundamentals saturate. In comparing the dimensional growth rates in Fig. 4.15, the reduction in growth rate of the fundamental mode tends to coincide with the increase in growth rate of its harmonic; i.e., the disturbance energy shifts from the saturating fundamental to the growing harmonic.

However, the harmonic saturates quickly and the only disturbance growth in the boundary layer, as seen in Fig. 4.11 at x>15 in., is a generalized spectral broadening of the second-mode frequency band and the low-frequency band centered about 0 kHz.

4.6 Low-Frequency Disturbances Over the Adiabatic Cone

Referring to Figures 4.9, 4.10, and 4.11, there is a third band of growing frequencies centered at 0 kHz in addition to the second-mode band and the harmonic band. Upon comparing Fig. 4.16 (the low-frequency disturbances in the boundary layer) and Fig. 3.4 (freestream noise), it can be seen that the trends are strikingly similar, with the lowest frequencies having the highest amplitudes. Furthermore, the noise in the freestream is first measurable at x=12.5 in. (see Fig. 3.2) and the low-frequency band is first detectable in the boundary layer near this same x-location (see Fig. 4.11).

The growth of the low-frequency band is thought to be closely related to the increasing freestream noise level. As the nozzle-wall boundary layer of the M6NTC becomes more strongly turbulent, the amplitude of the freestream noise impinging on the adiabatic-cone boundary layer increases with x, as evidenced in Fig. 3.4. These freestream disturbances are internalized and the amplitude of the low-frequency disturbances in the boundary layer at any given x is related to the history of the freestream noise upstream of that x location. If the "damping" of disturbances at the low frequencies is less than the "production" at low frequency energy by the freestream, then the disturbances at these frequencies will grow. Upon comparing Figures 3.4 and 4.16, it is clear that the disturbances at the lowest frequencies, 15 and 35 kHz, have grown to levels substantially higher than the freestream level. In fact, the growth at the lowest frequencies is much higher than any linear stability prediction and is similar to the second-mode growth in Fig. 4.14. Thus, it is concluded that the growing low-frequency disturbance band is most likely a result of the increasing freestream noise and henceforth the low-frequency band will be referred to as the "freestream noise" band.

Unlike the harmonic band, the growth of the freestream noise band has no effect on the linear growth of the fundamental. In Fig. 4.16, the lowest frequencies have measurable values as far upstream as x=11 in., but the fundamental second-mode disturbances are growing linearly as predicted by linear stability theory up to x=14 in. This tends to show that the freestream noise band is not a nonlinear effect of interacting second-mode frequencies and lends more credence to labeling these disturbances the "freestream noise" band.

The predicted first-mode frequency of the adiabatic cone is 70kHz and this frequency is embedded in the freestream noise band. The disturbance growth at 70kHz shown in Fig. 4.16 is not completely inconsistent with linear theory; however, the measured growth should not be considered a linear phenomenon because it occurs in a region of the boundary layer where nonlinear events have already been identified. In addition, Fig. 4.10 shows that 70kHz is not the center of a distinct first-mode frequency band. There may well be a growing first-mode disturbance in the adiabatic cone boundary layer, but its growth is undetectable in the linear region for x<14 in. Hence, the measurable disturbance at 70kHz is better described in this case as an artifact of the freestream noise than as a distinct first mode.

One additional observation concerns the low-frequency disturbances in the adiabatic boundary layer. From Figures 4.9, 4.10, and 4.11, the spectra at x=9 in. is devoid of any significantly growing disturbances, but Fig. 4.7 shows that a maximum in disturbances energy exists near the boundary-layer edge and Fig. 4.8 shows that the disturbance level increases with x. Recalling that the frequencies below 10kHz could not be resolved, as explained in Sec.3.1, it can then be concluded that the disturbance energy profile presented in Fig. 4.7 is due to the presence of sub-10kHz frequencies.

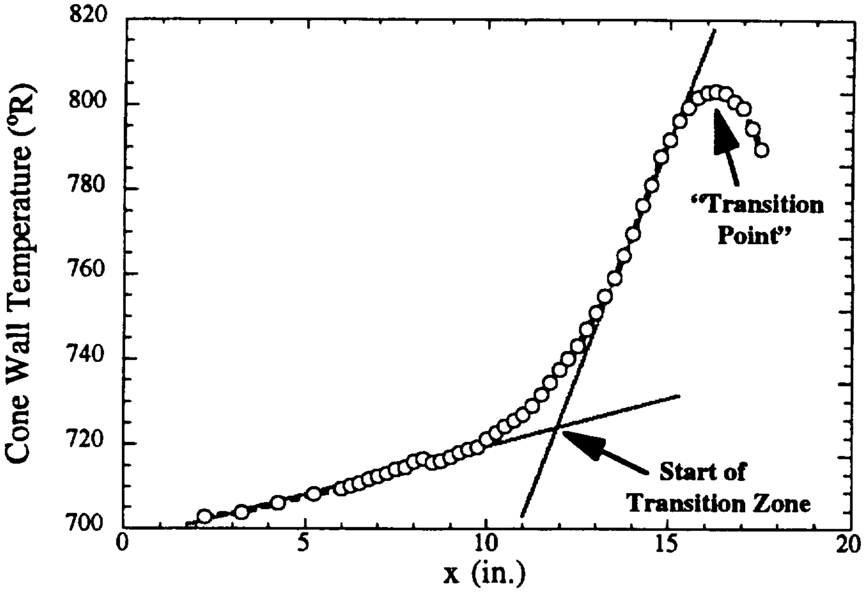

Figure 4.1 Wall Temperature (Adiabatic Cone)

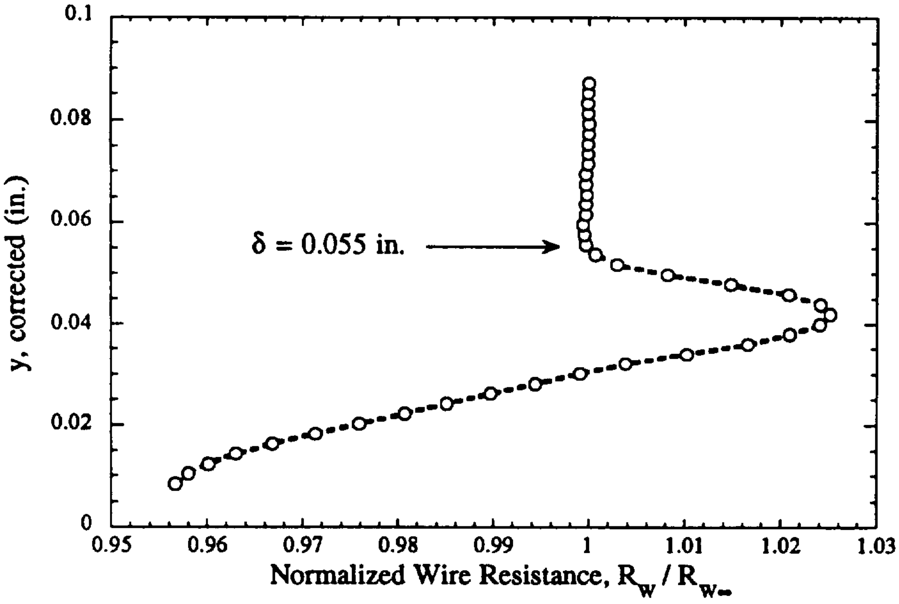

Figure 4.2 Resistance of Unheated Hot Wire at x=9.00 in. (Adiabatic Cone)

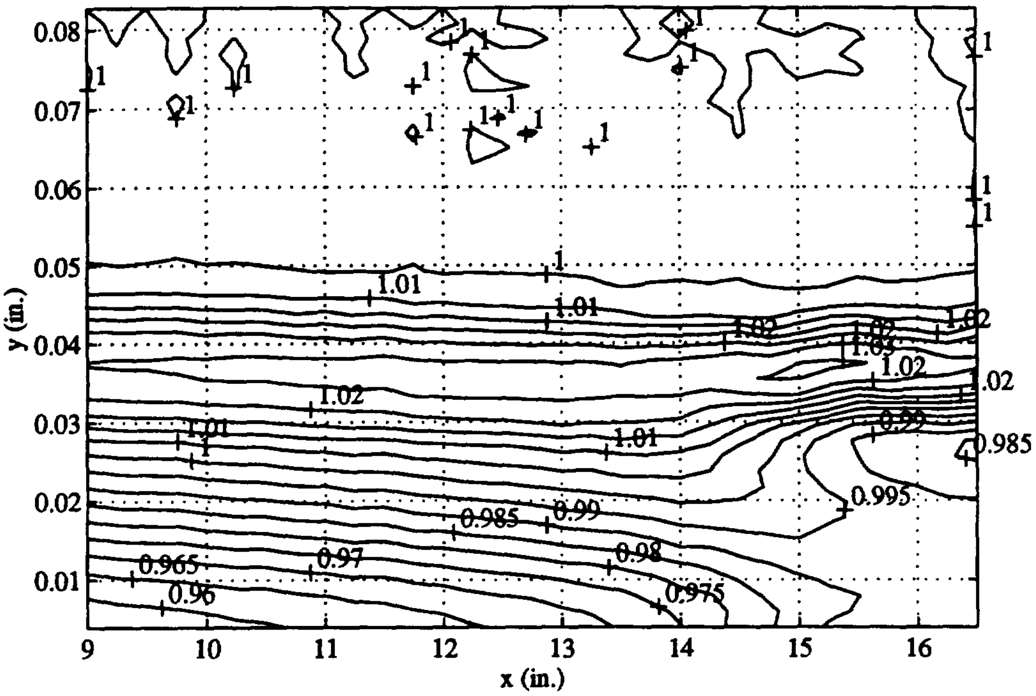

Figure 4.3 Contour Plot of Normalized R_w (Adiabatic Cone)

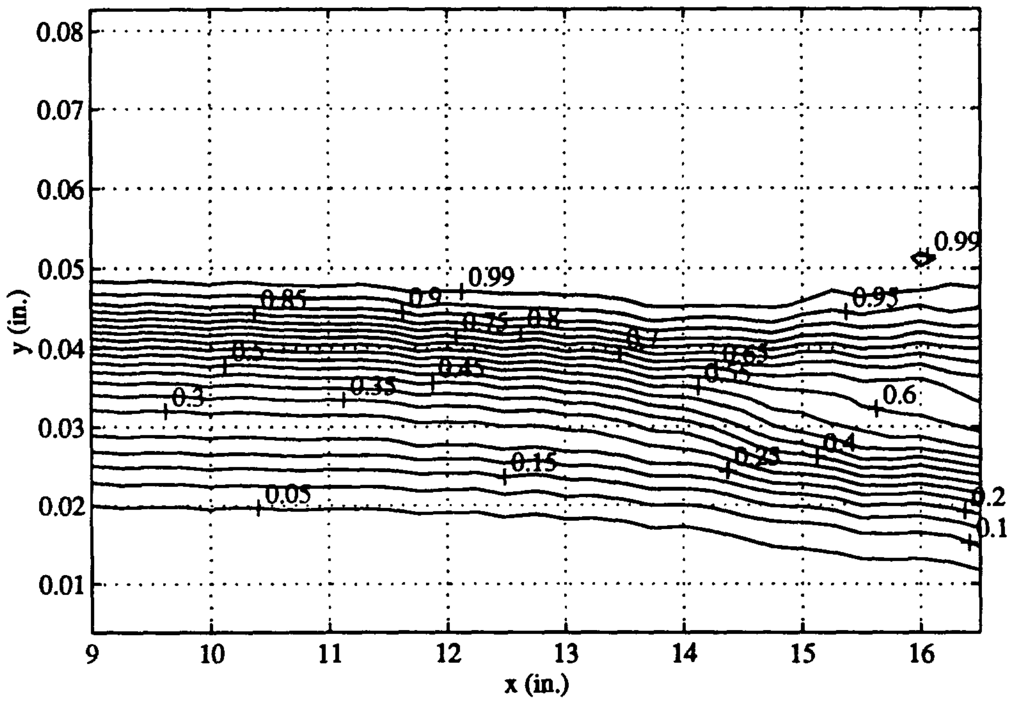

Figure 4.4 Contour Plot of Normalized $V_{s,mean}$ (Adiabatic Cone)

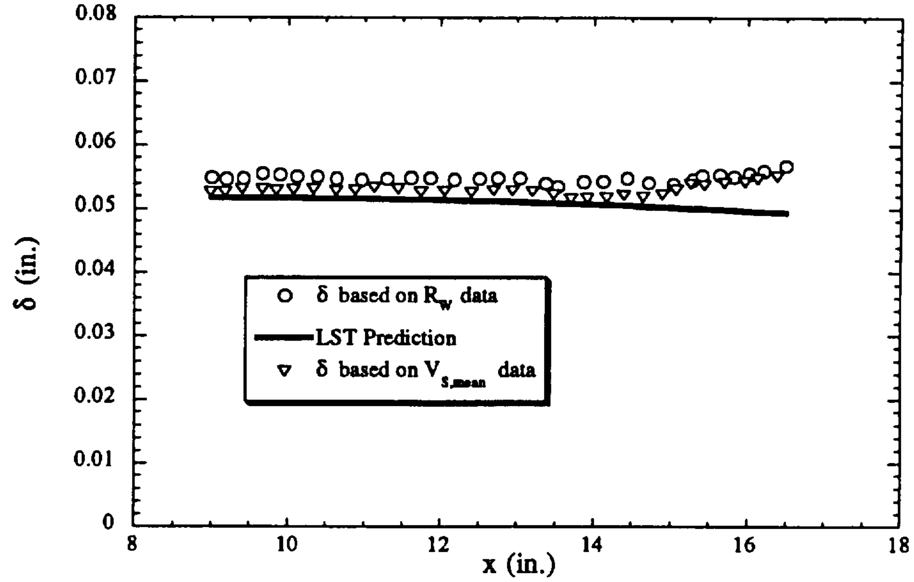

Figure 4.5 Boundary-Layer Thickness (Adiabatic Cone)

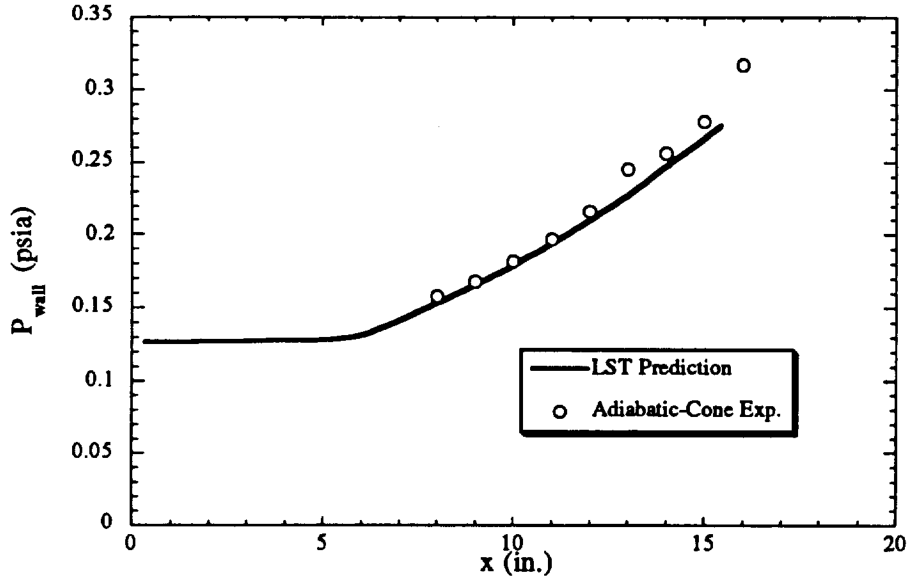

Figure 4.6 Wall Static Pressure (Adiabatic Cone)

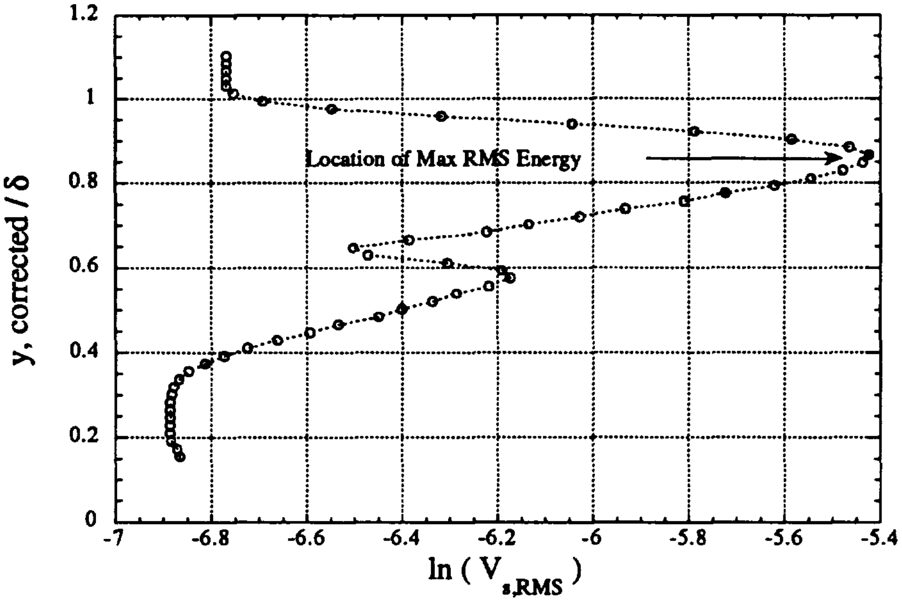

Figure 4.7 RMS Energy at x=9.00 in. (Adiabatic-Cone)

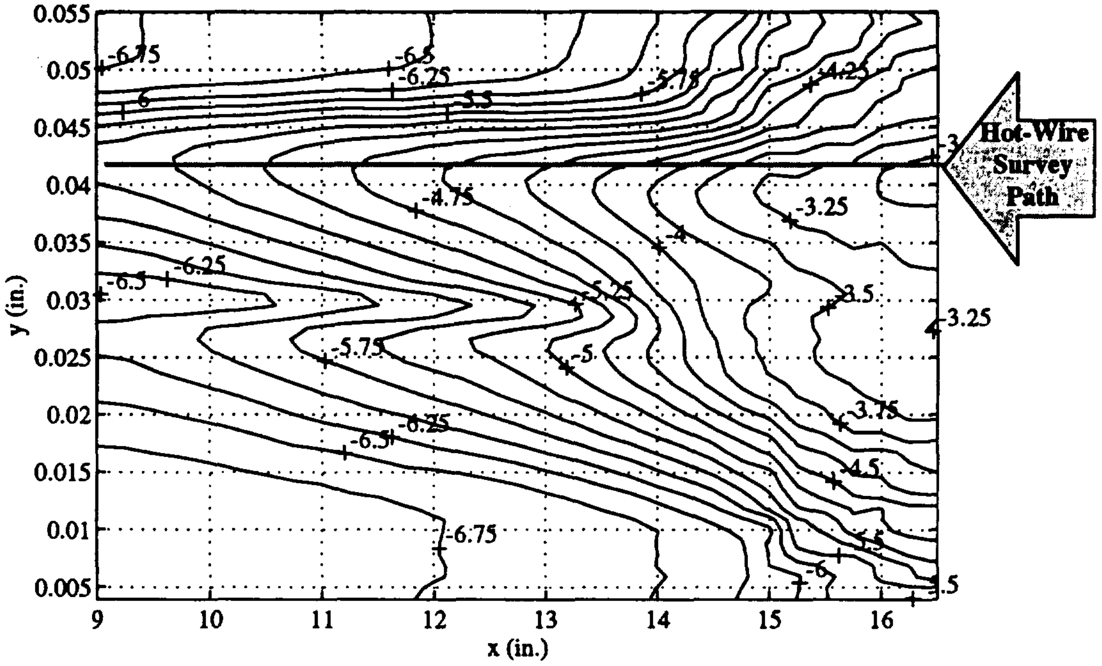

Figure 4.8 Hot-Wire Survey Path and RMS Contours (Adiabatic Cone)

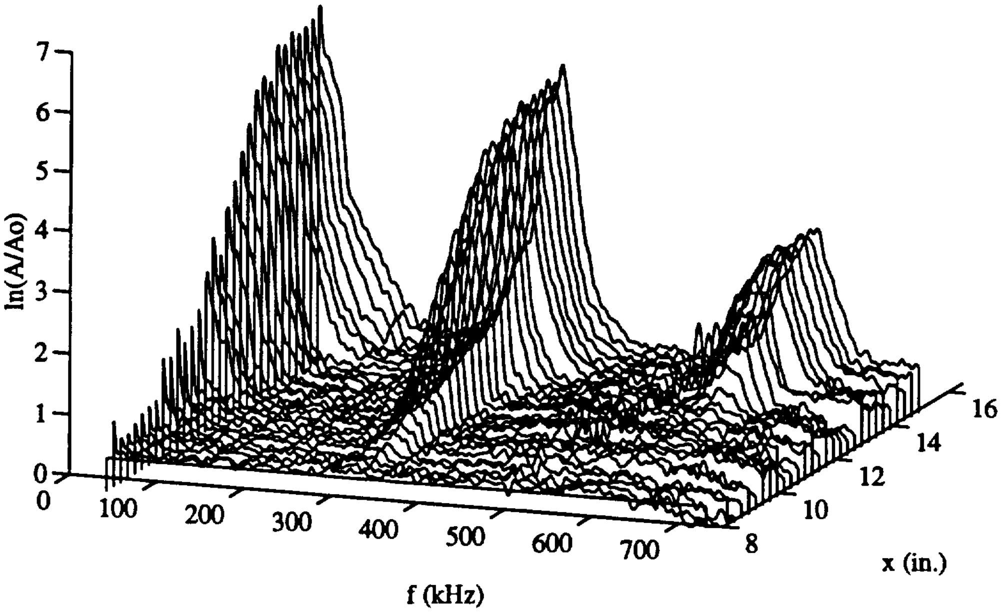

Figure 4.9 Disturbance Spectra in the Adiabatic-Cone Boundary Layer (Oblique View)

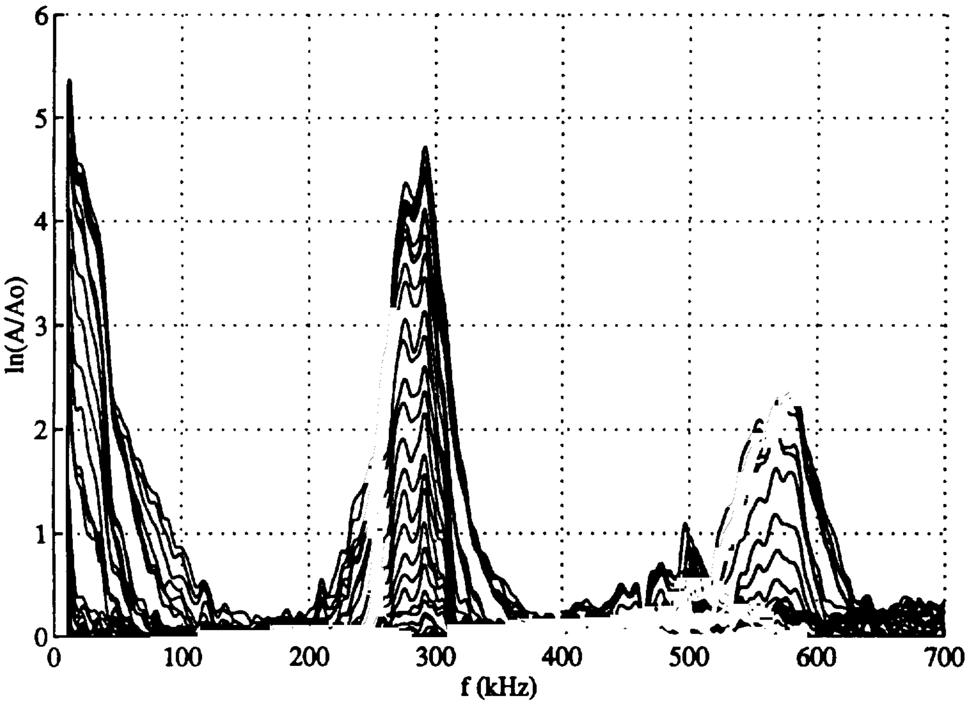

Figure 4.10 Disturbance Spectra in the Adiabatic-Cone Boundary Layer (Front View)

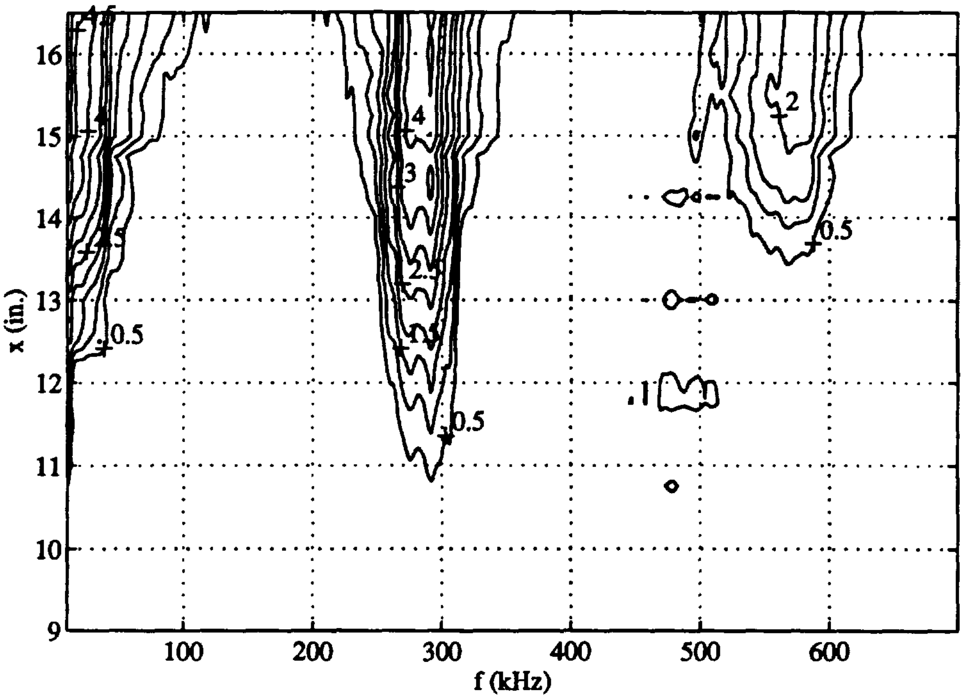

Figure 4.11 Disturbance Spectra in the Adiabatic-Cone Boundary Layer (contour plot) (contours based on ln(A/Ao) data in 0.5 increments from 0.5)

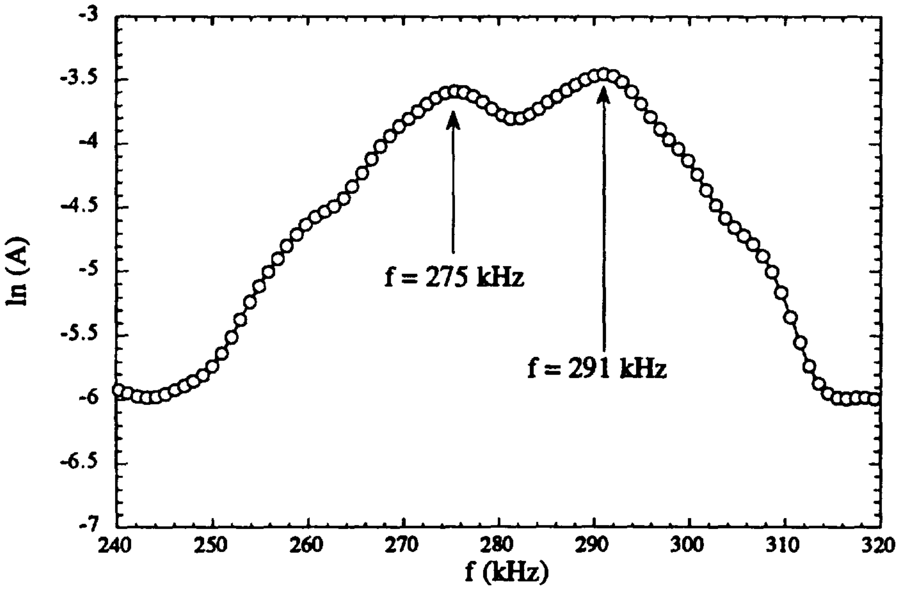

Figure 4.12 Second-Mode Disturbance Band (Adiabatic Cone, x=13 in.)

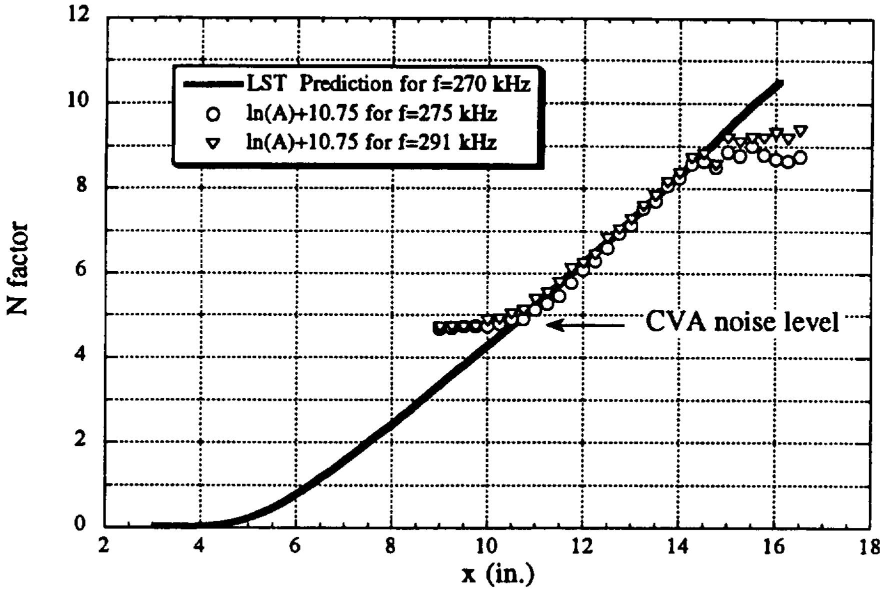

Figure 4.13 Disturbance Growth Chart for the Adiabatic-Cone Boundary Layer

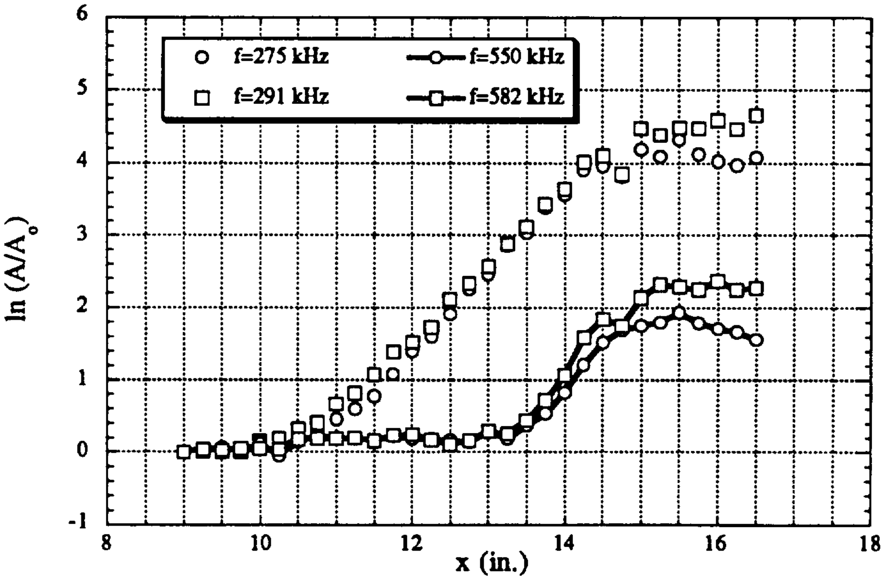

Figure 4.14 Growth of Second-Mode Disturbances and Harmonics (Adiabatic Cone)

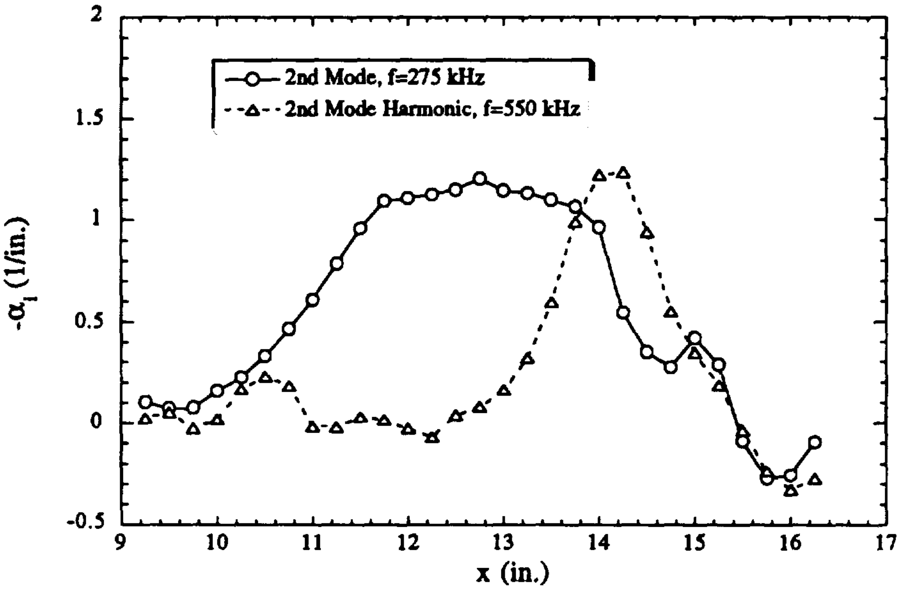

Figure 4.15 Second-Mode and Harmonic Growth Rates (Adiabatic Cone)

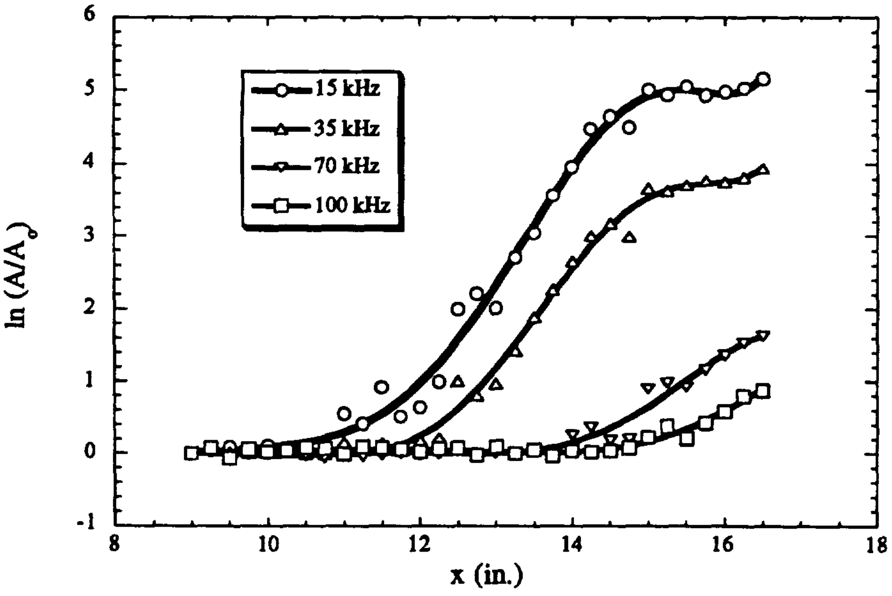

Figure 4.16 Low-Frequency Disturbances in the Adiabatic-Cone Boundary Layer

CHAPTER 5

COOLED-CONE MEASUREMENTS

5.1 Cooled-Cone Wall Temperature

In Fig. 5.1, the measured wall temperature variation of the cooled cone is presented and regions of large temperature gradients are present near the tip and base of the cone. Since the tip of the cone is not cooled, this region acts as a heat source that dissipates energy via conduction into the actively cooled region of the cone. The dissipation of energy produces a large negative temperature gradient for $x \leq 7$ in. At x=7 in., the wall temperature becomes nominally uniform at 470°R. This uniform cone temperature, which corresponds to the maximum cooling capability of the cooling system and hence the lowest possible cone wall temperature, extends to about x=11 in. where a positive temperature gradient begins. There is a peak in the wall temperature at about x=15 in., after which the temperature falls and finally rises again as the base of the cone is reached. This final rise is expected because of base conduction effects due to the presence of the relatively hot, uncooled sting assembly.

To obtain the cooled-cone wall temperature profile displayed in Fig. 5.1, the average wall temperature data from 22 cooled-wall tests was taken. Special procedures were developed in order to operate the cooled cone in the M6NTC successfully. During the preheat period of the tunnel where hot, high density air flowed over the cone, the set point of the cooling unit was T=25°C (537°R), due to the high thermal loads. The cooler would fail if the temperature were set any lower during preheat, because it would begin to operate in a cyclic, rather than a steady mode. If the cyclic mode were allowed, stagnant coolant would remain in the cone, absorb heat, and vaporize, rendering the coolant and the cooling unit ineffective. Once the tunnel was brought up to Mach 6 operating conditions, the set point on the cooler was lowered to -15°C (465°R) and within 5 to 10 minutes, a repeatable cone temperature distribution was achieved. Due to the active control of the cone temperature and the minimum preheat time required, the cooled-cone tests were significantly shorter than the adiabatic-cone tests.

In Fig. 5.1, a typical transition region is identified using the same method that was used for the adiabatic cone in Fig. 4.1. Hence, a transition zone over the cooled cone exists between x=11 and x=15 in., which represents an upstream migration of 1 in. relative to the transition zone of the adiabatic cone. This upstream movement of the transition zone due to wall cooling is expected, based on the LST predictions for enhanced second-mode growth.

5.2 Mean Boundary Layer Over the Cooled Cone

As with the adiabatic-cone boundary layer, the cooled cone was surveyed using an unheated hot wire as an indication of the stagnation temperature distribution through the boundary layer. In Fig. 5.2, the normalized resistance of the hot wire is plotted at x=9 in. As with the adiabatic cone, there is a bulge in R_w near the boundary-layer edge due to frictional heating, but the bulge is not as pronounced as in the adiabatic case. This effect, and the reduced value of R_w near the cone wall, is due to the significantly reduced wall temperatures. Note also that the boundary-layer thickness defined in Fig. 5.2 has been reduced from 0.055 in. in the adiabatic-wall case to 0.041 in. for the cooled wall.

In Fig. 5.3, a contour plot of R_w data is presented and a region of parallel contour lines can be seen for x<12.5 in. As discussed in Sec. 4.2, this region of approximately parallel contour lines is expected when the boundary layer is changing slowly; i.e., when it is laminar. The results of the mean-flow analysis verify that the velocity and temperature profiles change slowly in the laminar region.[14] For x>12.5 in., it can be seen that the contours undergo significant changes in shape associated with disturbance growth at harmonic frequencies in the nonlinear region of the adiabatic-cone boundary layer.

Using a heated hot wire, the cooled-cone boundary layer was surveyed and the mean CVA output was recorded. A contour plot of the normalized data is presented in Fig. 5.4 which confirms that the region for x>12.5 in. is significantly different in character than the region for x<12.5 in. Hence, based on the results of the adiabatic-cone investigation, the data in Fig. 5.3 and Fig. 5.4 suggest that the boundary layer becomes nonlinear as x increases beyond 12.5 in.

To facilitate comparison with theoretical predictions, boundary-layer thickness data from Figures 5.3 and 5.4, as defined in Sec. 4.2, are plotted in Fig. 5.5. As was the case for the adiabatic cone in Fig. 4.5, the predicted and measured boundary-layer thicknesses agree to within the error of the experiment for x<13.5 in. For x>13.5 in., the data in Figures 5.3 and 5.4 show that the mean boundary layer is deforming and the increasing boundary-layer thickness further suggests that the boundary layer is becoming turbulent. This same sequence of data; i.e., deforming mean flow followed by an increasing boundary layer, was also observed for the adiabatic cone. However, cooling has moved transition upstream while reducing the laminar boundary-layer thickness by 25%.

Finally, the wall pressure for the cooled cone is presented in Fig. 5.6. As with the adiabatic cone, there is good agreement between the cooled-cone data and the predicted wall pressure where the boundary-layer thickness matches the laminar value in Fig. 5.5. As x increases beyond 14 in., it can be seen that the wall pressure begins to increase to levels higher than the laminar predictions. This increase may be attributed to the increasing thickness of the boundary layer (see Fig. 5.5), as the boundary layer becomes turbulent.

Considering all the mean-flow data, the behavior of the cooled-cone boundary layer may be deduced, as was done for the adiabatic cone. The results of the heated and unheated hot-wire surveys suggest that the boundary layer begins to distort for x>13 in. and this distortion is followed by an increase in boundary-layer thickness and wall pressure starting at x=13.5 in. Hence, it may be deduced with reasonable certainty that the cooled-cone boundary layer is laminar for x<13 in. and that the mean flow has undergone a significant distortion by the time the "transition point," as shown in Fig. 5.1, has been reached (at x=15 in.).

5.3 Overview of Cooled-Cone Disturbances

The profile of disturbance RMS energy level at x=9 in. presented in Fig. 5.7 for the cooled cone is qualitatively and quantitatively similar to the adiabatic-cone RMS plot at the same x-location in Fig. 4.7. Again, maximum RMS energy for the cooled cone occurs near the boundary layer edge at $x/\delta=0.90$, indicative of second-mode behavior and the RMS energy reaches an asymptotic "zero" value in the freestream by $y/\delta=1.2$.

The contour plot of all the RMS data for the cooled cone is presented in Fig. 5.8 (including the path of the hot-wire survey used to collect the timetrace data). This figure is strikingly similar to Fig. 4.8 for the adiabatic cone; i.e., the adiabatic-cone data for x<16.5 in. exhibits nearly identical trends as the cooled-cone data for x<14 in. The LST analysis (and LST in general) shows that cooling the wall does not diminish the inviscid instability mechanism[14] and the similarity of the RMS data for the adiabatic and cooled walls appear to confirm this prediction. Also, the distortion in the cooled cone case of the RMS trends for x>12.5 in. coincides with the distortion of the mean flow data. Especially noteworthy in Fig. 5.8 is the -2.5 contour near x=16.5 in., since it represents an increasingly uniform distribution of disturbances throughout the boundary layer, as would be expected in a turbulent flow.

In Figures 5.9, 5.10 and 5.11, the spectral content of the timetrace data is presented in an oblique-view waterfall plot, a front-view waterfall plot, and a contour plot, respectively. As was the case for the adiabatic cone, there are three distinct peaks in the cooled cone spectra that are associated with freestream noise, the second mode and the second-mode harmonic. At the most downstream position in these spectra plots, the nearly complete evolution to a turbulent boundary layer is evident; hence, these are the first data that document the evolution of linear disturbances into a nearly turbulent flow in a quiet hypersonic flow.

5.4 Second-Mode Disturbances Over the Cooled Cone

From the LST calculations, the most unstable frequency in the cooled-cone boundary layer are second-mode disturbances at 310kHz. There is a band of frequencies with growing disturbances in the experimental data which contains this frequency. As was the case for the adiabatic cone, the cooled-cone boundary layer thickness remained roughly constant in Fig. 5.5 for x<13.5 in., and as a result, there is no noticeable shifting of the second-mode frequencies (see Fig. 5.10).

To identify the frequencies associated with the wave packets in the cooled-cone case, the disturbance spectrum at x=12 in. is presented in Fig. 5.12. The wave packets appear to be composed of three main frequencies -- 291, 306, and 320 kHz. Note that 291kHz was one of the frequencies associated with the adiabatic-wall wave packets (see Fig. 4.12) and is a contributor to the cooled-cone wave packets as well. However, the dominant frequency in the cooled cone case is clearly 306 kHz.

A comparison of the growth of the disturbance at 306kHz with the predicted growth of disturbances at 310kHz in Fig. 5.13 shows that there is a region where the two compare very well. At the low end, near N=6.8, the electronic noise level of the CVA prevents further disturbance detection upstream of x=10 in., and at N=11 (x=13 in.) the second-mode disturbances have saturated. This saturation point at N=11 for the cooled cone is higher than the saturation point at N=9 for the adiabatic-wall case; however, both saturation N-factors are consistent with linear boundary-layer transition predictions.[5] One possible explanation for the difference in N-factor growth is that the initial disturbance in the cooled-cone boundary layer enters (or develops) at a later point; e.g., where N~2, such that the saturation N-factor could be scaled back to the adiabatic cone level of N=9. The internalization and generation of disturbances in the hypersonic boundary layer is best addressed by "receptivity" experiments that can help explain this difference in N-factor, but these types of tests require equipment much more sensitive than was used in the present experiments.

The growth of disturbances at the other wave-packet frequencies is illustrated in Fig. 5.14, which shows that there is a region where these disturbances grow near the rate of those at the dominant wave-packet frequency. Hence, as was the case for the adiabatic cone, the cooled-cone second-mode disturbances grow as a set of discrete wave-packet frequencies that generally follow the growth predicted for the most unstable second-mode frequency using LST.

5.5 Second-Mode Harmonics Over the Cooled Cone

The frequency band that exists in Figures 5.9, 5.10, and 5.11 at double the second-mode frequency is considered to be the harmonic band of the second mode, as was the case for the adiabatic cone. In Fig. 5.15, the growth of the dominant second mode disturbances at 306kHz and the harmonic are compared and are seen to match the growth trends already discussed for the adiabatic-cone case in Figures 4.14 and 4.15. For x>13 in., the harmonic has grown to its maximum amplitude and has saturated, along with the fundamental. This location (x=13 in.) compares well with the location where the mean-flow contours in Figures 5.3 and 5.4 and the RMS contours in Fig. 5.8 begin to distort. Since mean-flow distortion and harmonic generation are characteristics of nonlinearity, it can be concluded that the flow over the cooled cone has become nonlinear for x>13 in. This onset of nonlinearity in the cooled-cone boundary layer occurs approximately one inch upstream of its occurrence in the adiabatic-cone boundary layer.

5.6 Low-Frequency Disturbances Over the Cooled Cone

The third band of growing disturbances was previously termed the "freestream noise" band due to its likely freestream source in the adiabatic-cone case and will be designated similarly in the cooled-cone case. Comparing Figures 5.16, 4.16, and 3.4, the amplitude trends are similar, except that the low frequencies in the cooled-cone case have another region of growth for x>15 in. Amplitudes at the lowest frequencies, 15 and 35 kHz, in both the cooled-wall and adiabatic-wall boundary layers appear to reach a saturation level which occurs at or near the onset of the nonlinear region in each case. In addition, disturbances growth at the lowest frequencies is greater in the cooled-cone case than the adiabatic-cone case. This suggests that the internalization of freestream noise frequencies by the boundary layer could be related to the growth of the fundamental disturbances. Since the cone model has a flared geometry, there is always the concern that the low-frequency disturbances were caused by the development of Görtler vortices. Regardless of the source of the low-frequency band, the second-mode disturbances in the cooled-cone boundary layer grow linearly; i.e., independently, as they did in the adiabatic-cone boundary layer.

First-mode disturbances are damped by wall cooling, as predicted by linear stability theory, and there is a distinct, slowly-growing, 50kHz disturbance peak in the linear region (x<13 in.) of the cooled-cone boundary layer. This disturbance is easily seen in the contour plot of Fig. 5.11 and its amplitude is compared with second-mode amplitude data in Fig. 5.17. It should be noted that there was no distinct first mode in the adiabatic-wall case and so the 50kHz disturbance in the cooled-cone case is somewhat unexpected. LST calculations predict that 70kHz is the most unstable first-mode frequency for the adiabatic-wall case, and the analysis of another cone with a similar flared geometry[11] suggests that a frequency of 50kHz for the first mode is reasonable for the cooled-wall case. Comparing the growth of the first and second modes in Fig. 5.17 between x=10 and 13 in., the second mode is seen to grow four times as fast (on a logarithmic scale) as the first mode, as expected.

The growth region at x>15 in. in Fig. 5.16 occurs in a nonlinear region and cannot be explained by linear theory. Referring to Fig. 5.11, it can be seen that between x=13 and 15.5 in., the only "growth" indicated by the hot wire is a generalized spectral broadening of the disturbance bands, as was the case for the adiabatic cone for x>14 in. (Fig. 4.11). Beyond x=15.5 in., the spectra fills with measurable disturbance frequencies between the three dominant peaks. So the growth of frequencies beyond x=15.5 in. is not limited to low frequencies. Note that disturbances at 153kHz (the subharmonic of the second mode) show no growth until x>15.5 in., and there is no distinct band of frequencies associated with the subharmonic (see Fig. 5.11).

5.7 Disturbance Growth in the Nonlinear Region

The rapid, generalized broadening of the spectrum in the region for x>15.5 in. was found to be accompanied by a rapidly growing unknown disturbance near 800kHz, as seen in Figures 5.18 and 5.19. This disturbance is not an integer multiple of the dominant second-mode disturbance, so it cannot be considered another harmonic of the fundamental. If the spectral broadening is considered the final breakdown of the fundamental disturbance, then this growing unknown disturbance could be destructively interacting with the fundamental structure to generate the turbulent frequency pattern that is clearly evolving. Attempts to repeat the results found for x>15.5 in. for the cooled cone were mostly unsuccessful due to the large dynamic loads in this nearly turbulent region that readily broke the hot-wire sensors. By contrast, results in the linear region were easily repeatable for both the cooled-cone and the adiabatic-cone cases. Thus, due to spectral broadening, the region for x>15.5 in. is considered the "breakdown" region of the flow in the cooled-cone boundary layer. As was the situation as in another hypersonic experiment,[104] the second-mode disturbances in this experiment retains its character well into the breakdown region.

A comparison of the spectrum at x=16.5 in. in Fig. 5.18 with the last spectrum in Fig. 5.10 shows that the spectral data in Fig. 5.18 appears much smoother than the spectral data in Fig. 5.10. This apparent conflict is due to the division of the amplitudes, A, by the amplitudes at x=9 in. In other words, the "roughness" of the spectrum between 100 and 250 kHz in Fig. 5.10 is a result of the noise at the furthest upstream location and should not be considered the result of other disturbance modes.

It must be noted that the disturbance at 800kHz is twice the bandwidth of the CVA, so the amplitudes of the disturbances at 800kHz have been greatly attenuated. There does not appear to be a valid electronic explanation for the well-defined, exponentially growing disturbance band at 800kHz, so the disturbances were considered a fluid dynamic phenomenon. At the very least, the existence of a growing disturbance at 800kHz in this experiment highlights the need for high-bandwidth instrumentation to investigate the nonlinear and breakdown regions of hypersonic boundary layers. Moreover, the need for even higher sensitivity equipment to measure smaller amplitude disturbances (see Figures 4.13 and 5.13) defines the instrumentation requirements for future hypersonic stability investigations in the linear region.

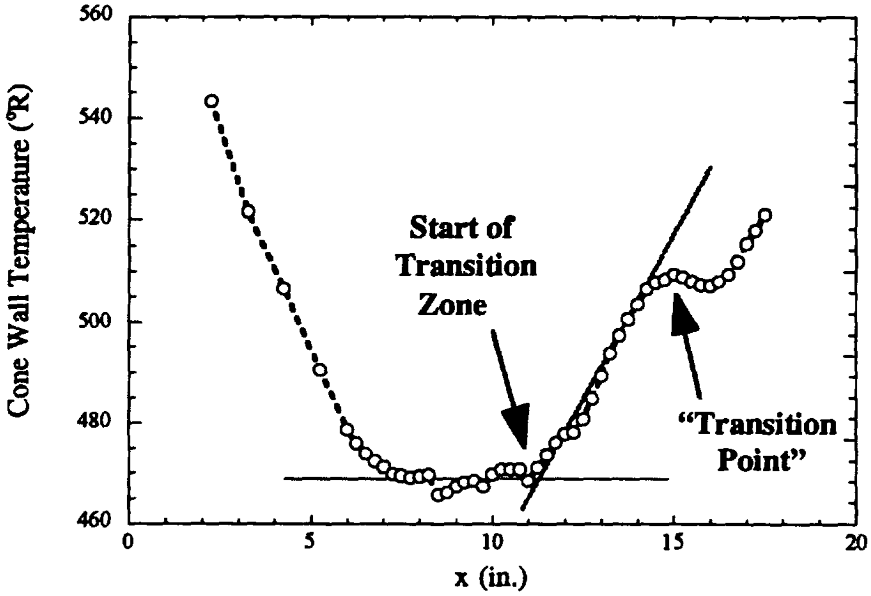

Figure 5.1 Wall Temperature (Cooled Cone)

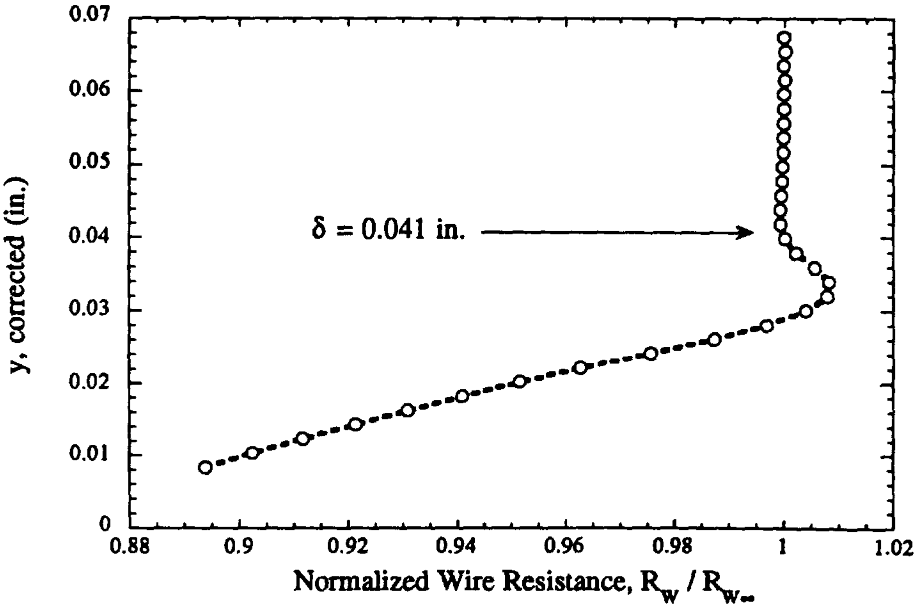

Figure 5.2 Resistance of Unheated Hot Wire at x=9.00 in.(Cooled Cone)

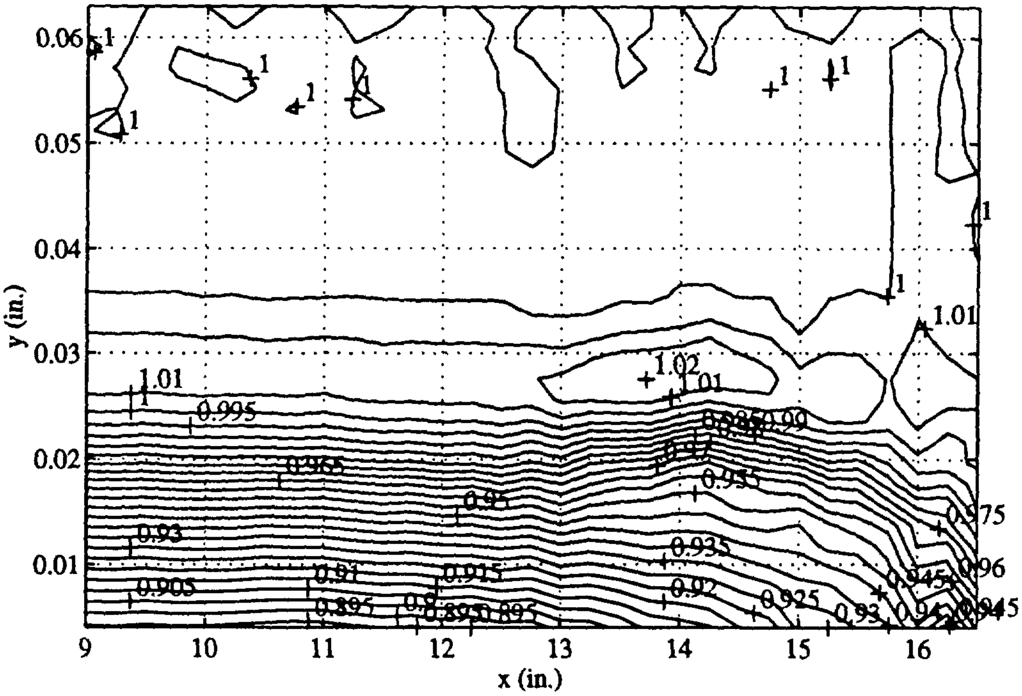

Figure 5.3 Contour Plot of Normalized R_w (Cooled Cone)

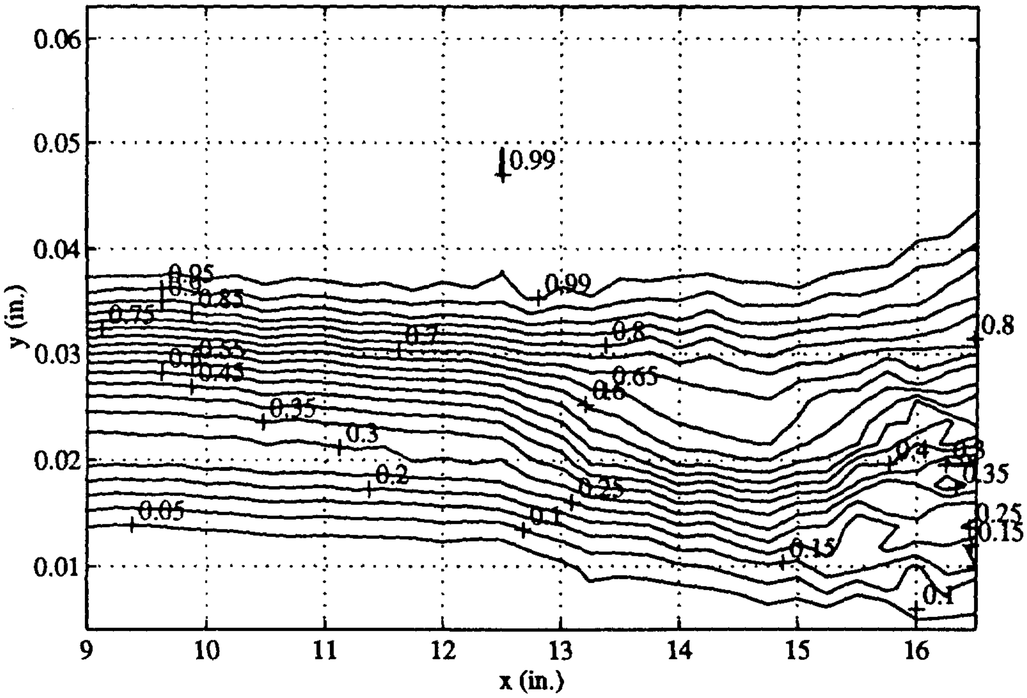

Figure 5.4 Contour Plot of Normalized $V_{s,mean}$ (Cooled Cone)

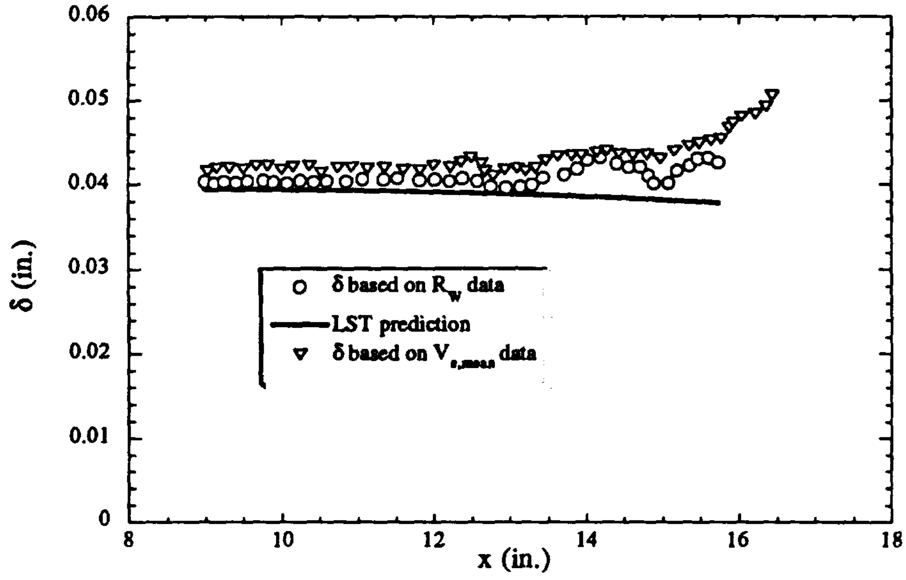

Figure 5.5 Boundary-Layer Thickness (Cooled Cone)

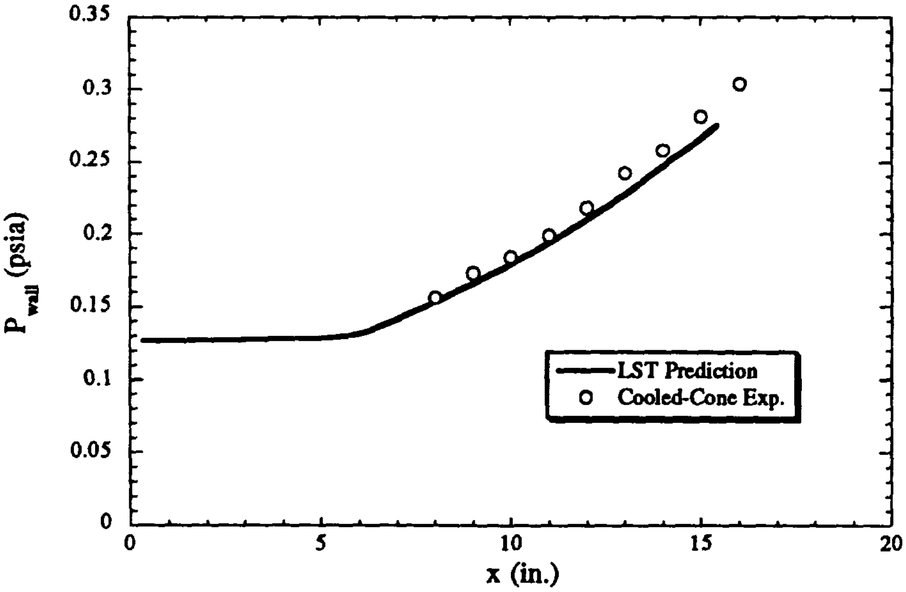

Figure 5.6 Wall Static Pressure (Cooled Cone)

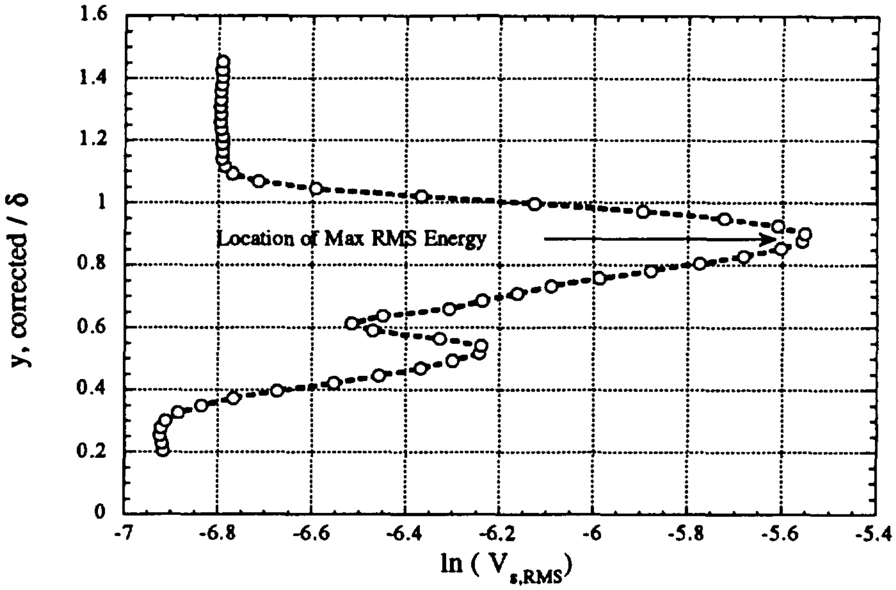

Figure 5.7 RMS Energy at x=9.00 in. (Cooled-Cone)

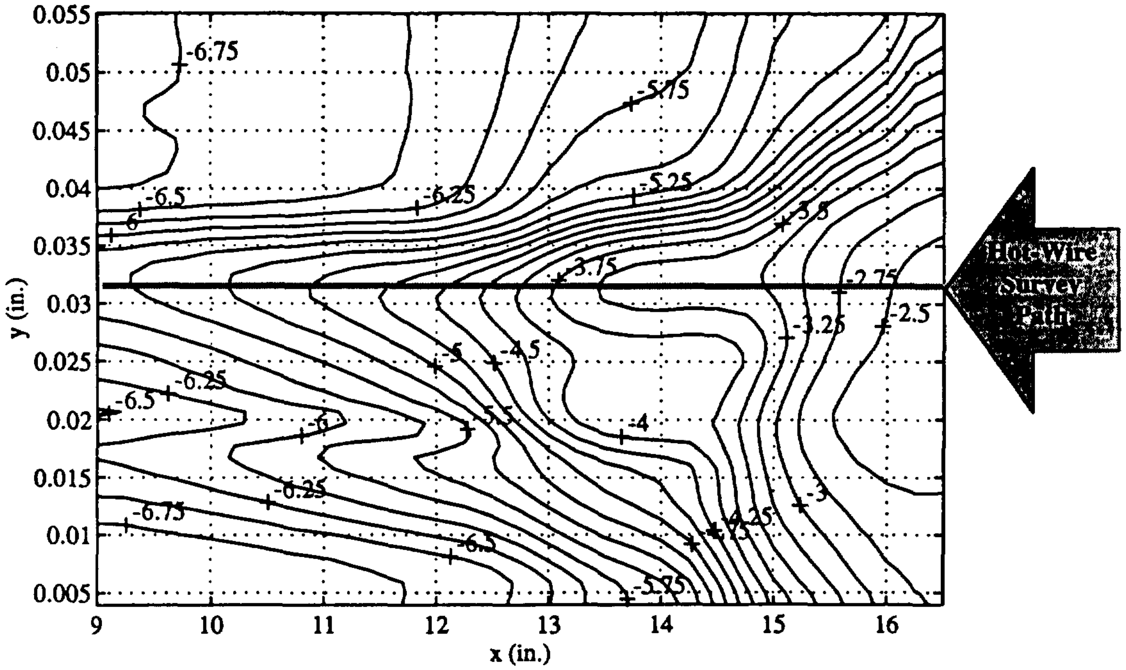

Figure 5.8 Hot-Wire Survey Path and RMS Contours (Cooled Cone)

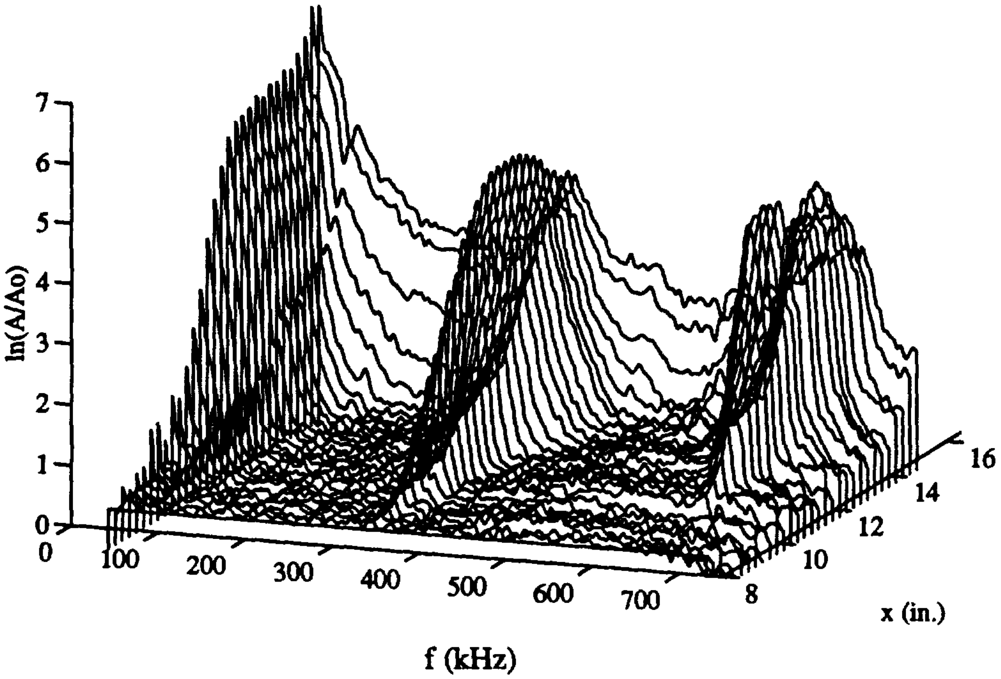

Figure 5.9 Disturbance Spectra in the Cooled-Cone Boundary Layer (Oblique View)

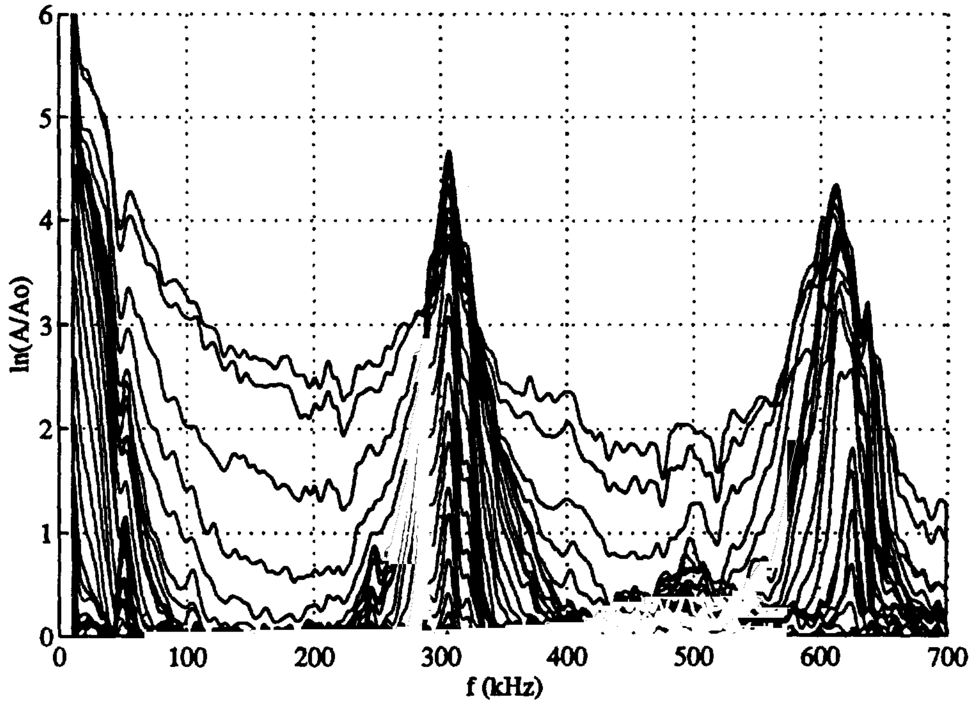

Figure 5.10 Disturbance Spectra in the Cooled-Cone Boundary Layer (Front View)

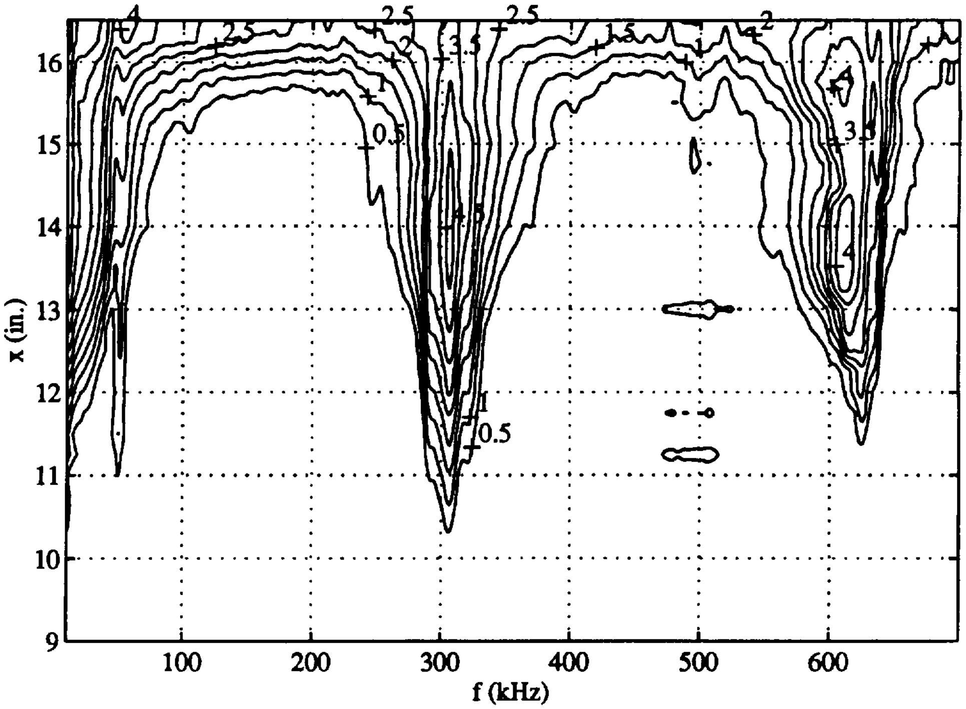

Figure 5.11 Disturbance Spectra in the Cooled-Cone Boundary Layer (contour plot)

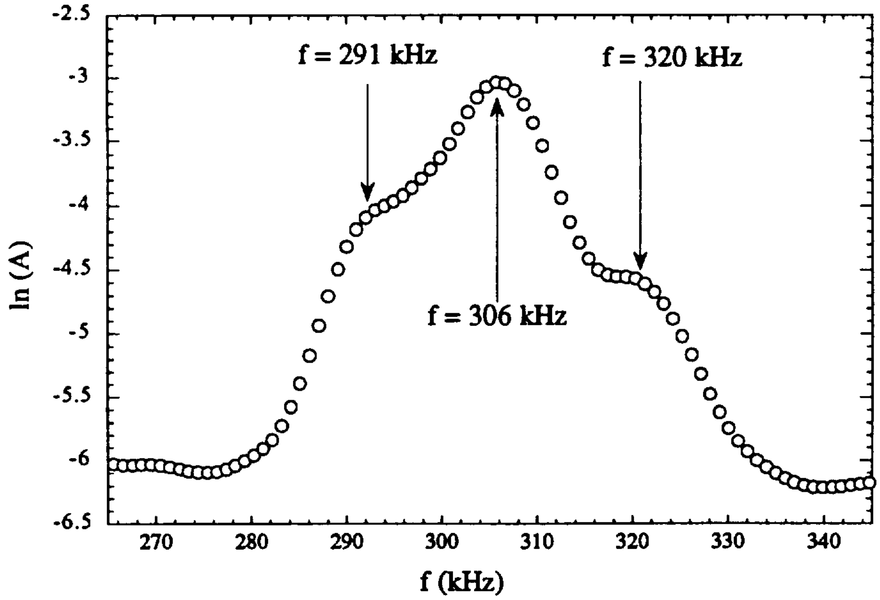

Figure 5.12 Second-Mode Disturbance Band (Cooled Cone, x=12 in.)

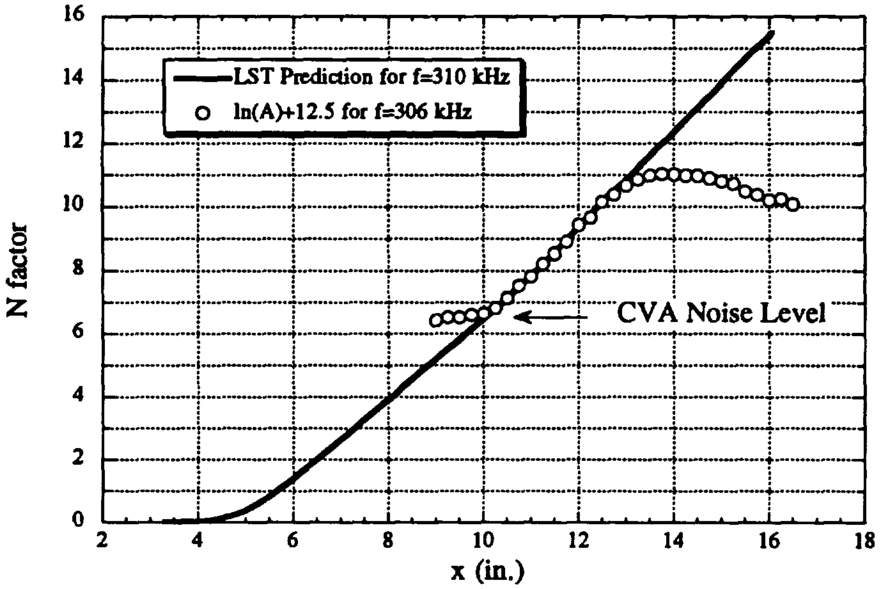

Figure 5.13 Disturbance Growth Chart for the Cooled-Cone Boundary Layer

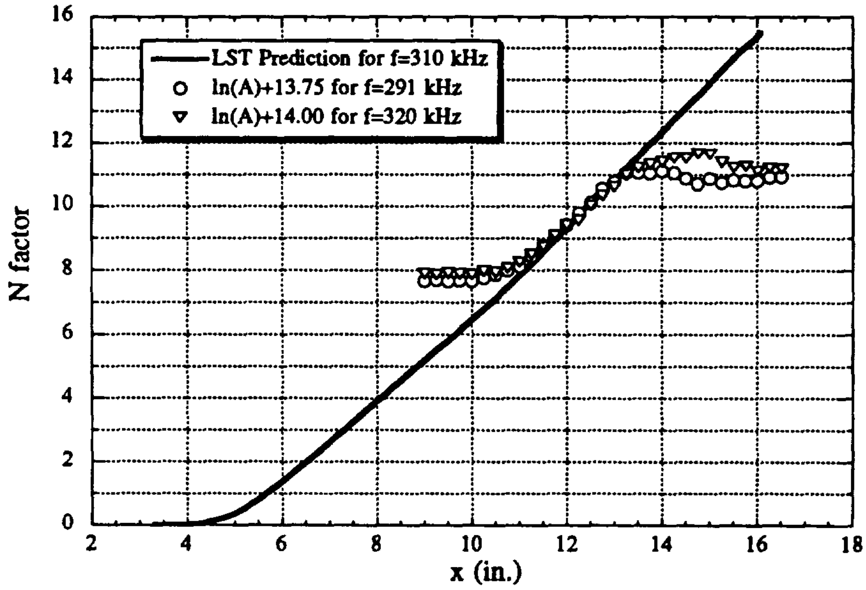

Figure 5.14 Growth Chart for 291 and 320 kHz (Cooled Cone)

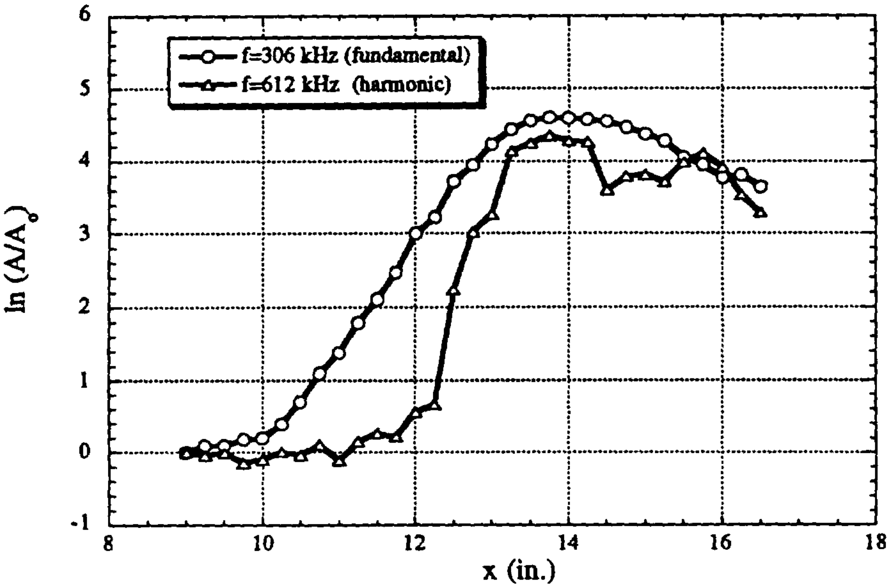

Figure 5.15 Growth of Second-Mode Disturbance and Harmonic (Cooled Cone)

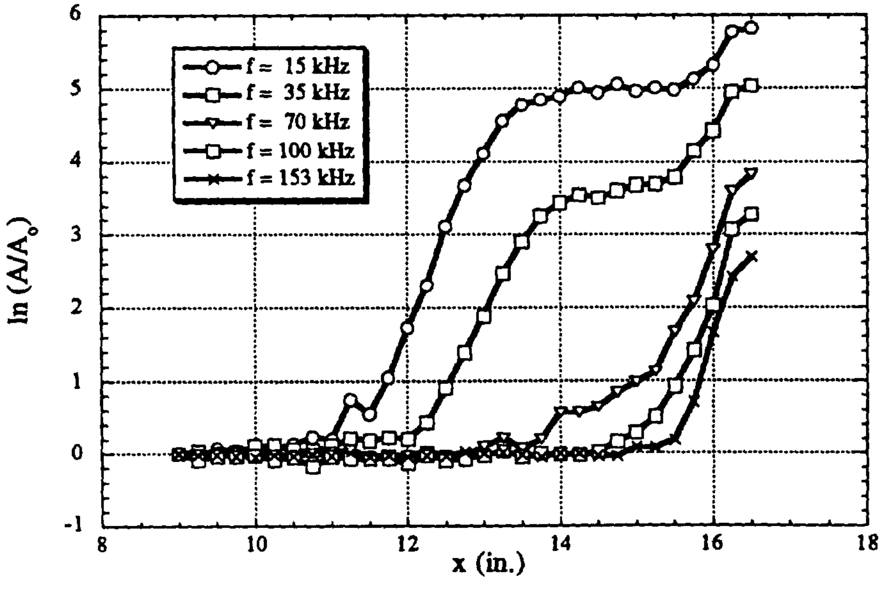

Figure 5.16 Low-Frequency Disturbances in the Cooled-Cone Boundary Layer

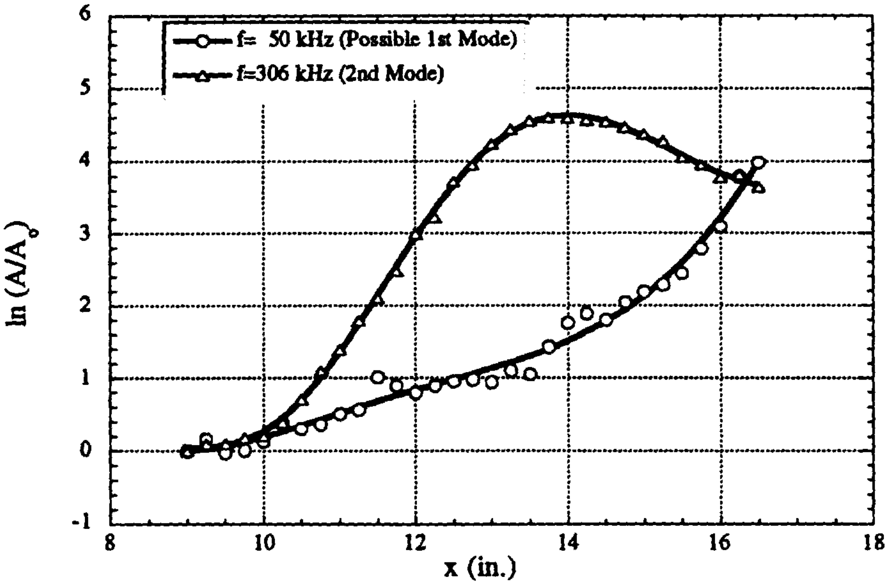

Figure 5.17 Growth of the Second Mode and a Possible First Mode (Cooled Cone)

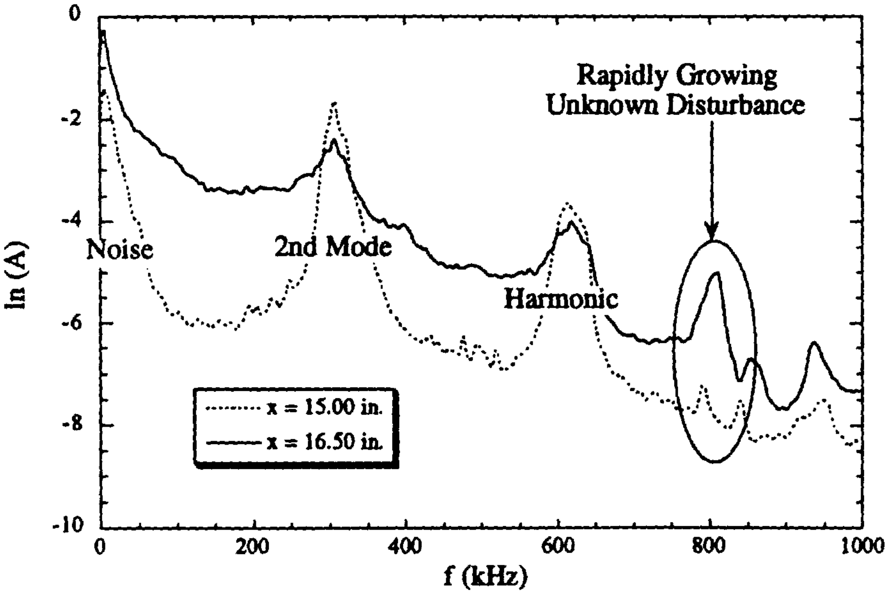

Figure 5.18 Spectral Growth in the Nonlinear Region (Cooled Cone)

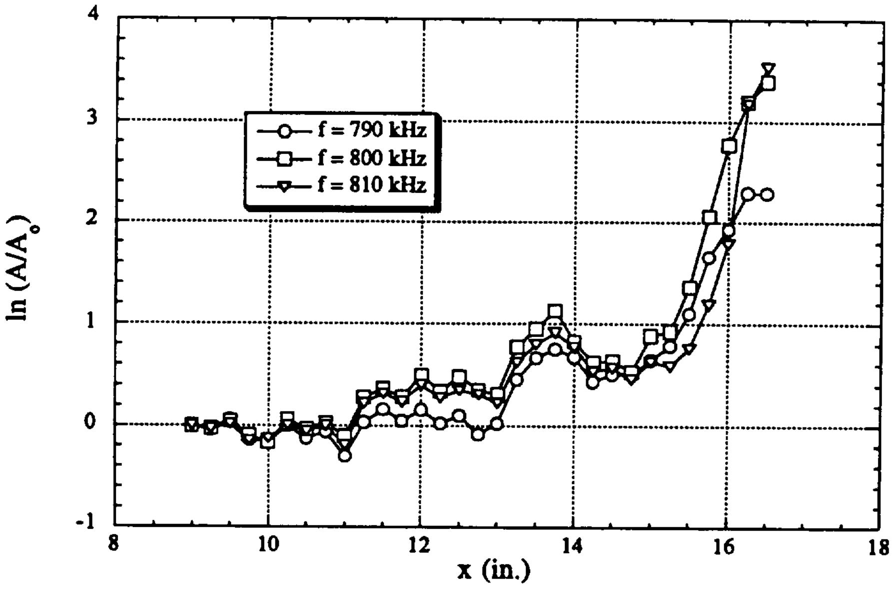

Figure 5.19 Growth of the Unknown Disturbance Band Identified in Fig. 5.18

CHAPTER 6

EXPERIMENTAL SENSITIVITIES

6.1 CVA Operation Mode

The normal response of a hot-wire sensor in a high-speed flow depends primarily on mean mass flow, mean total temperature, and overheat ratio. In this experiment, all spectral data were acquired using a constant overheat ratio of 1.5, meaning that the unsteady output was dependent upon variations in mean-flow quantities only and that overheat variations were eliminated. The CVA may be operated in its normal mode whereby overheat is neglected and the voltage is held constant; however, the overheat of the wire drifts with variations in the recovery temperature.

To investigate the sensitivity of the results to the CVA operation mode, the boundary layer of the adiabatic cone was surveyed with a constant wire voltage, V_w, set on the CVA and the results are compared with constant overheat (OH) data in Fig. 6.1. In the constant voltage case with V_{rh}=5.0V, the overheat of the wire drifted from about 1.45 at the most upstream location, to 1.35 at the most downstream location. As seen in Fig. 6.1, the fundamental second-mode disturbance (275kHz) has a slightly higher amplitude as it grows linearly in the constant overheat case and the harmonic (550kHz) is also slightly larger; however, the trends of the two data sets are similar and selecting a higher wire voltage would probably close the amplitude gap. The hot-wire sensitivity varied with the mean flow as the surveys were conducted, but the exponential growth of the flow disturbances overshadowed these small, by comparison, variations in both cases. Thus, due to the exponential growth of the disturbances, the experimental results are generally insensitive to the operating mode of the CVA as long as a "reasonable" operating wire voltage or overheat is selected.

6.2 Wall Cooling

The lowest wall temperature achieved with the present experimental apparatus was 470°R, which is higher than the 420°R wall temperature used in the LST calculations. To investigate how this variation in temperature impacts the experimental results, the cone was cooled at the minimum rate possible with the cooling system (defined by the boiling point of the cooling fluid) and this wall temperature distribution is presented in Fig. 6.2. In this figure, the wall temperature in the uniform temperature region was 540°R, which is significantly higher than the 470°R used in the experiment.

Using LST trends and the results of Chapter 5 as a guide, an increase in boundary-layer thickness, a reduction in second-mode frequencies, and a reduction in growth rate would be expected at this higher wall temperature compared to the cooled-wall case. Examination of the normalized wire resistance data of Fig. 6.3 indicates that the boundary-layer thickness, increased by 0.003 in. from the cooled-wall case in Fig. 5.3, but is still 0.011 in. below the adiabatic-wall case shown in Fig. 4.3. This increase in boundary-layer thickness should alter the second mode by decreasing the most unstable frequencies due to the boundary-layer tuning effect of the second mode. In Fig. 6.4 the dominant wave-packet frequencies associated with the second mode are presented and can be compared to the frequencies in Fig. 5.12 for the cooled-wall case. For a wall temperature of 470°R, the second-mode wave packet has characteristic frequencies of 291, 306, and 320 kHz. However, when the wall is warmed to 540°R the contribution from 320kHz essentially disappears and the wave packet is composed primarily of disturbances at 291 and 306 kHz. In both cases, however, the dominant frequency is 306kHz and the growth of disturbances at this frequency and their harmonics are compared in Fig. 6.5. The main effect of warming the wall is to reduce the growth rate of the fundamental mode slightly and to delay its saturation point and the accompanying generation of harmonics by roughly 0.5 in.

Since the growth rate and saturation point of the fundamental mode decreases slightly, the evolution of the transition process should be slowed in the case with minimum wall temperature of 540°R relative to the 470°R case. In Fig. 6.6, the contour plot of the disturbance spectra near the location of maximum RMS energy for the wall temperature of 540°R is presented. Compared to Fig. 5.11, it is clear that the boundary layer in the 540°R wall temperature case has only begun to enter the breakdown region at x=16.25 in., while the flow in the cooler-wall case enters the breakdown region further upstream at 15.5 in.

In summary, the trends documented in Figures 6.3 to 6.6 for the wall temperature of 540°R fall between the trends for the adiabatic wall and for a wall temperature of 470°R, but are much closer to the 470°R trends. It can be expected that there may have been a slight increase in growth rate and an increase in the amplitude of the wave-packet frequency at 320kHz had the 420°R wall temperature been achieved. The experimental data is sensitive to changes in wall temperature, as expected, but sensitivity is relatively low for the cooled-wall temperatures investigated and thus the experimental data in Chapter 5 corresponding to a wall temperature of 470°R may be readily compared to the 420°R LST predictions.

6.3 Angle-of-Attack

Orienting the cone at zero angle-of-attack (A-O-A) with respect to the tunnel flow was done using simple mechanical measurements of the cone axis with respect to the axis of the nozzle. The error in this method is ±0.1° in yaw and A-O-A. To investigate the sensitivity of the experimental results to cone orientation, the cone model was rotated by 0.32° in the x-y plane so that the thermocouples and boundary-layer survey path were on the windward side and the pressure orifices were on the leeward side.

In Figures 6.7, 6.8, and 6.9, the effect of this aforementioned A-O-A variation on the mean flow are presented for the cone model under adiabatic-wall conditions. Since the pressure ports were on the leeward side, the compression of the flow on that side was reduced and a reduction in wall pressure was expected. In Fig. 6.7, the wall pressure on the leeward side has been reduced relative to the adiabatic-cone case (at zero A-O-A) showing that the new orientation had a measurable effect. This A-O-A effect has also altered the temperature of the cone wall on the windward side, as shown in Fig. 6.8, by reducing the amplitude and location of maximum wall temperature. The downstream movement of the maximum wall temperature point by about 0.5 in., as shown in Fig. 6.8, suggests that transition of the boundary layer has moved downstream on the windward side. This trend in transition point is consistent with other experimental trends.[106] According to the LST results, the introduction of a flare on the straight cone model compressed the flow and reduced the boundary-layer thickness. Increasing the A-O-A slightly also compressed the flow on the windward side, producing a reduction in boundary-layer thickness. The normalized R_W contour plot (Fig. 6.9) shows that the boundary-layer thickness has been reduced by 0.004 in. relative to the adiabatic-cone case of Fig. 4.3. Thus, the mean effect of the 0.32° increase in A-O-A was to increase wall pressure on the leeward side and to reduce boundary-layer thickness and delay transition on the windward side.

Since the second mode is highly tuned to the thickness of the boundary layer, the reduction in boundary-layer thickness in Fig. 6.9 resulted in an increase in second-mode frequencies, as shown in Fig. 6.10. Recalling that the second-mode wave packet was composed primarily of disturbances at 275 and 291 kHz for the zero A-O-A case, it is clear that the wave-packet frequencies have increased substantially to 299 and 311 kHz for the 0.32° A-O-A case. With a reduction in boundary-layer thickness of about 7%, it is significant to note that the dominant second-mode frequencies have increased by about 7% as well. This is an excellent example of the tuning of the second mode to the thickness of the boundary layer for a given wall condition. It should be noted that if care was not taken in orienting the cone relative to the mean flow, the dominant frequencies could shift to levels as high as those due to the wall cooling. Moreover, the similarity in transition trends (see Fig. 6.8) could easily have led to the false conclusion that linear stability theories predicted the "wrong" second-mode frequency when a slight A-O-A existed. Thus, the frequencies of the second mode are highly sensitive to slight A-O-A variations due to the boundary-layer tuning effect, but the care taken to achieve zero A-O-A in this experiment was sufficient to ensure the validity of the experimental results to within the ±0.1° orientation error quoted.

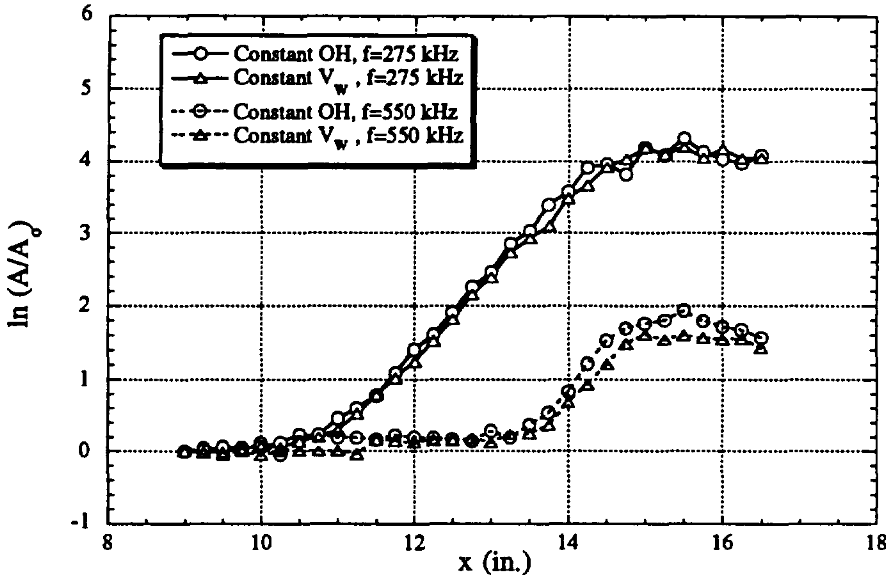

Figure 6.1 Sensitivity of CVA Operation Mode to Adiabatic-Cone Disturbances

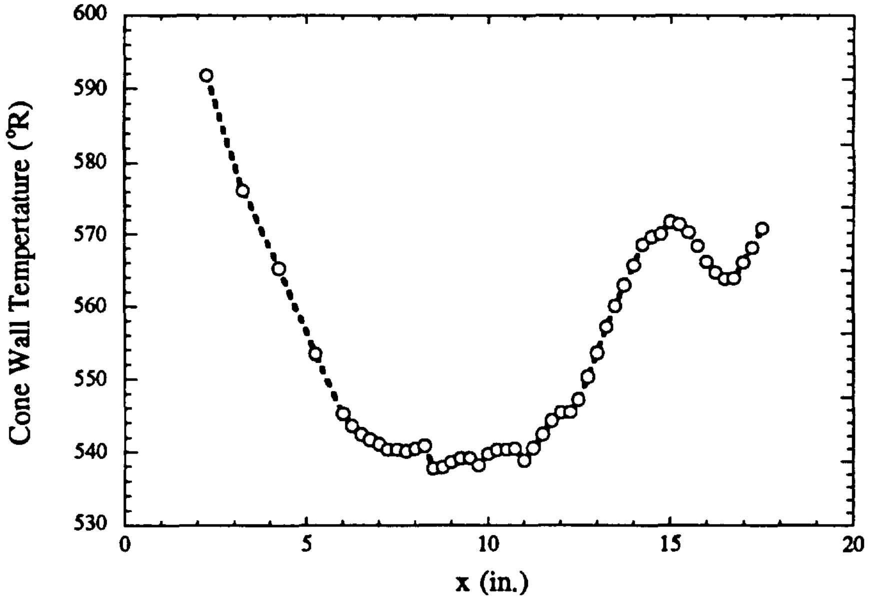

Figure 6.2 Wall Temperature of the Cone with Mimimum Cooling

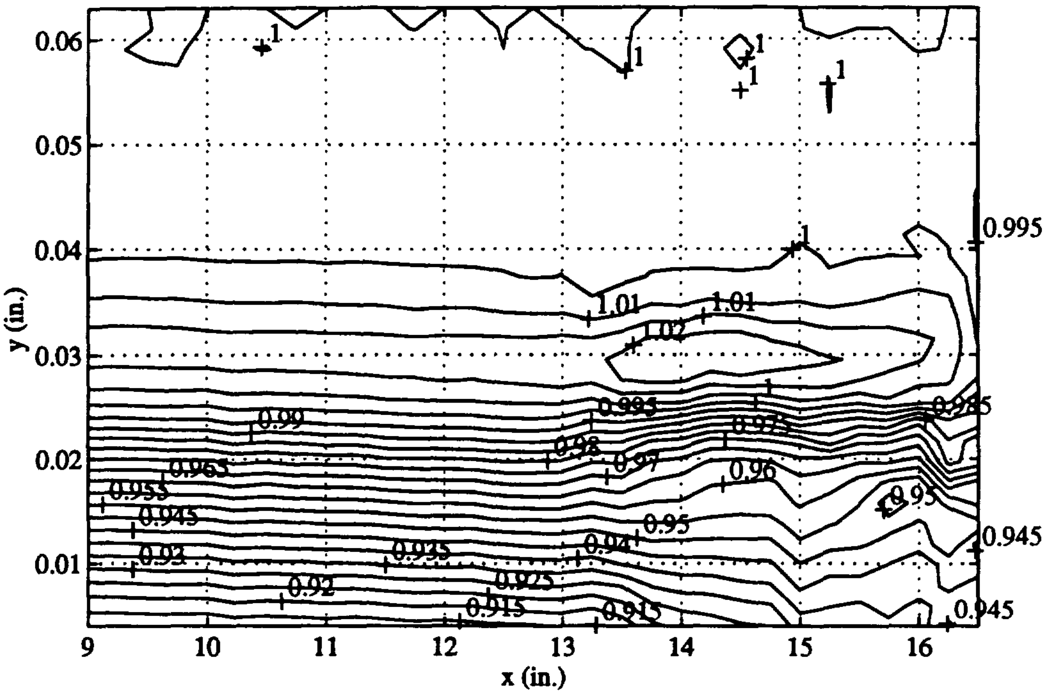

Figure 6.3 Contour Plot of Normalized R_w with Minimal Cooling

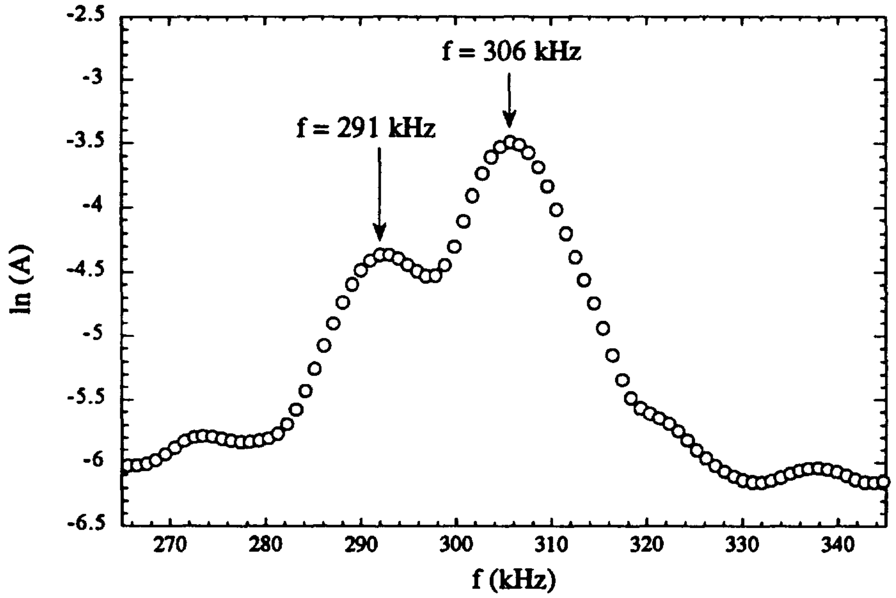

Figure 6.4 Second-Mode Disturbance Band (Mimimum Cooling, x=12 in.)

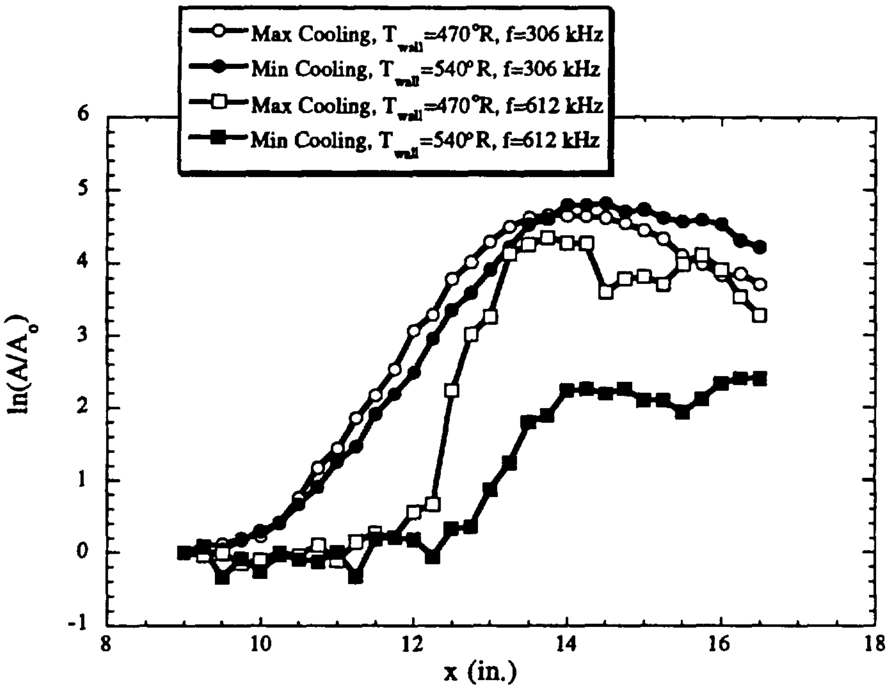

Figure 6.5 Variation in Disturbance Growth with Cooling Rates

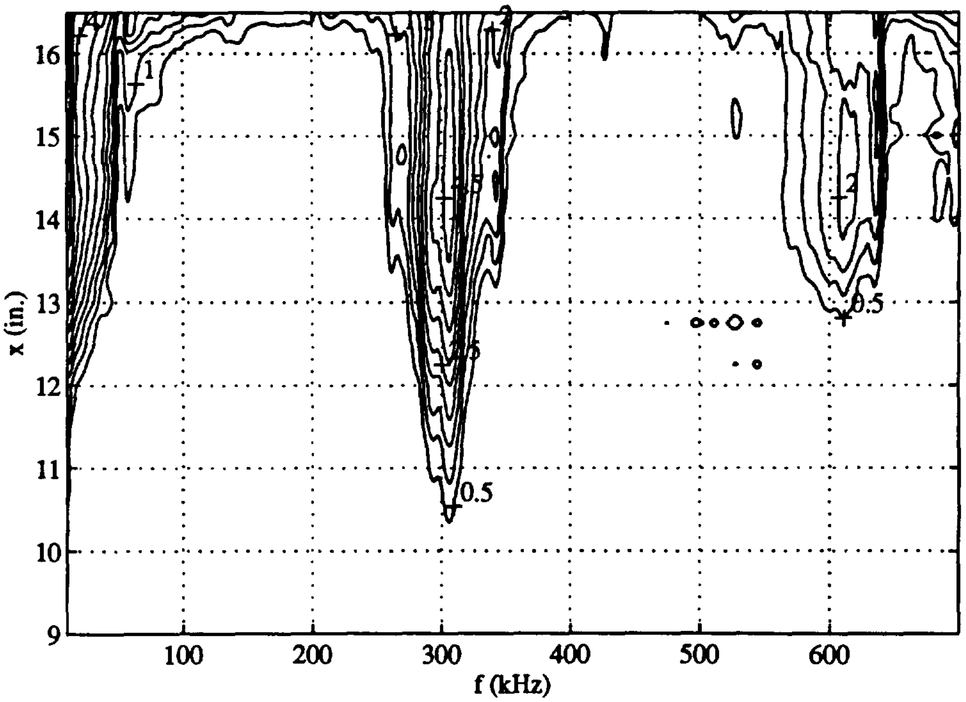

Figure 6.6 Disturbance Spectra in the Minimally-Cooled Boundary Layer

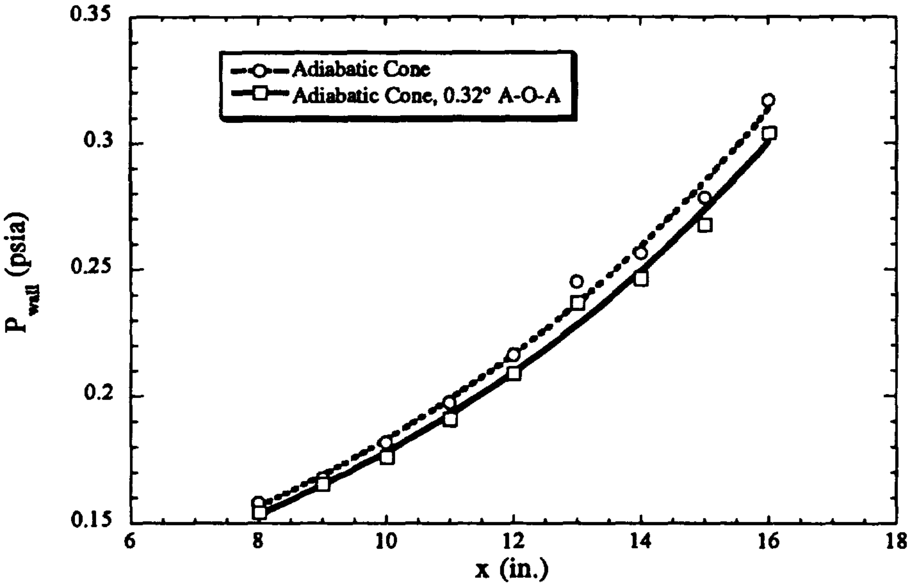

Figure 6.7 Variation in Wall Pressure with A-O-A (Leeward Side Measurements)

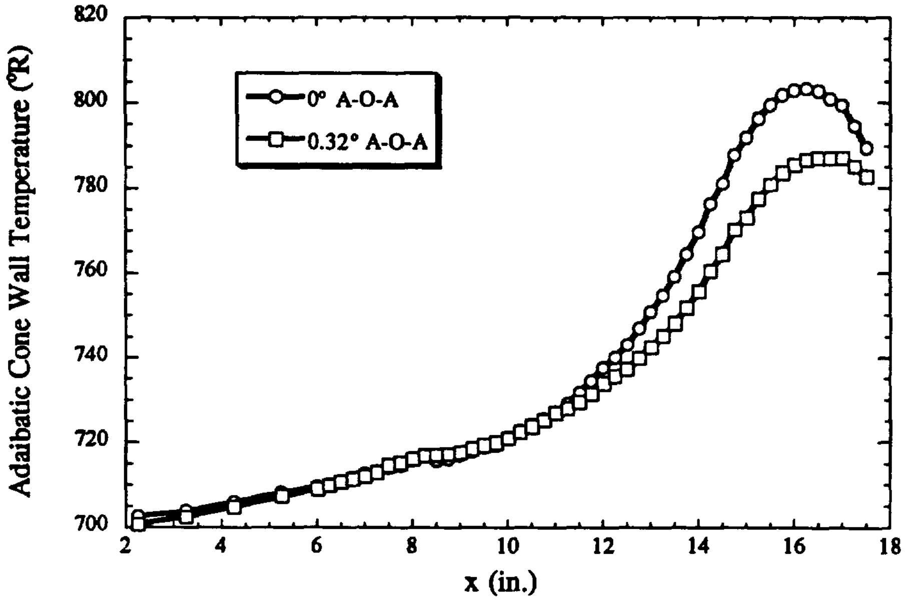

Figure 6.8 Variation in Wall Temperature with A-O-A (Windward Side Measurements)

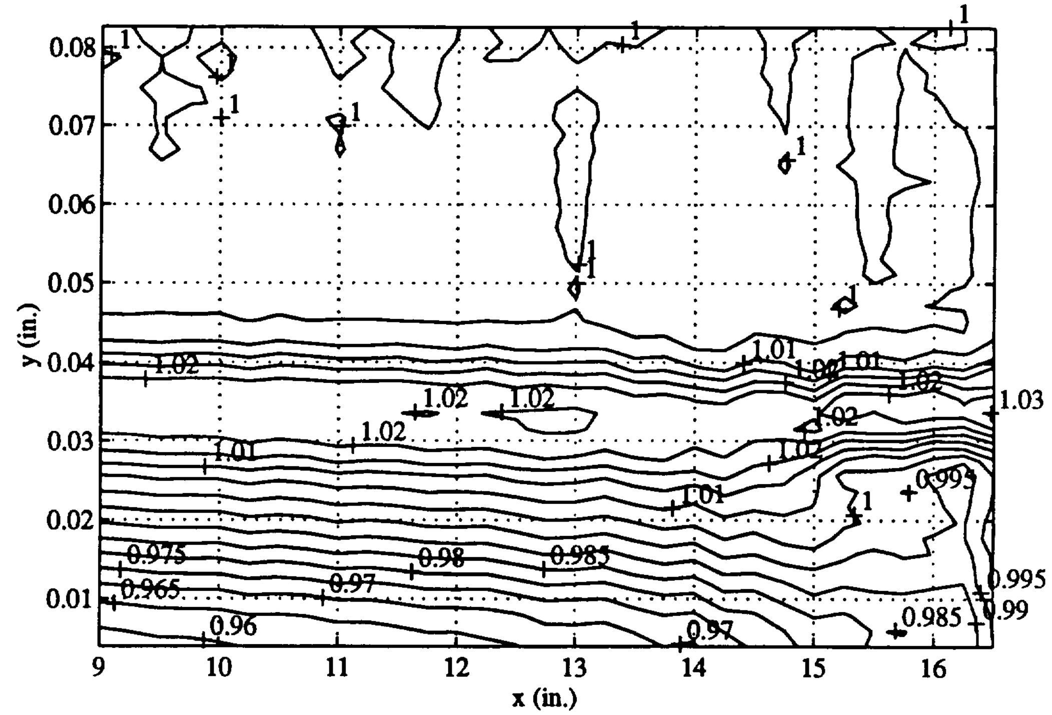

Figure 6.9 Contour Plot of Normalized R_w in the Adiabatic-Cone Boundary Layer with 0.32° A-O-A (Windward Side Measurements)

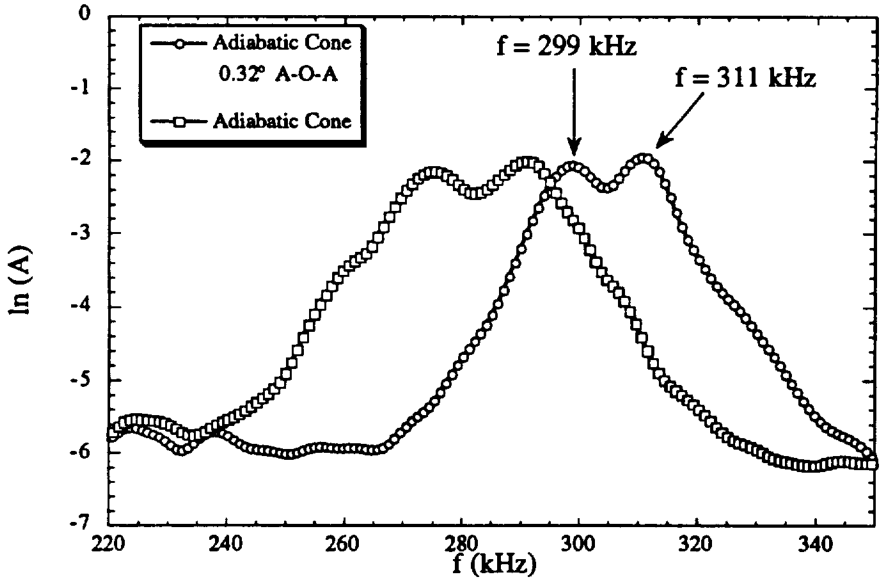

Figure 6.10 Variation in Wave-Packet Frequencies with 0.32° A-O-A (Windward Side Measurements, x=14.25 in.)

CHAPTER 7

SUMMARY, CONCLUSIONS, AND RECOMMENDATIONS

7.1 Summary

7.1.1 Hypersonic Transition

Prior to this experiment, few, if any, experimental data sets existed that documented the evolution of linear disturbances into turbulent flow in the hypersonic flow regime. Most often, a set of linear amplitude data were acquired at one Reynolds number, then the Re was increased, along with the freestream noise level, and a set of nonlinear amplitude data was acquired. In this experiment, for the cooled-wall test of Chapter 5, a unique set of continuous spectral data was acquired that shows linear disturbances being distinguishable from the electronic noise, saturating, and finally breaking down into a nearly turbulent flow. In terms of disturbance growth and mean-flow distortion, the adiabatic-wall data may be considered a subset of the cooled-wall data.

Referring to Fig. 7.1, the linear region of the transition zone in the hypersonic boundary layer over the cooled cone can be readily identified. Up to $x=13$ in., the primary instabilities grow linearly; that is, the boundary layer allows first- (50kHz) and second-mode (306kHz) disturbance waves to grow independently and at exponential rates. The low frequencies are also seen to grow independently in this region and do not interfere with the development of the primary instabilities. Based on LST predictions, the boundary layer is unstable to disturbances at second-mode frequencies starting at $x{\sim}4$. However, due to the limitations of modern sensing equipment, there are no detectable disturbances until $x>10$ in. in the linear region.

The linear region ends as x=13 in. is approached and the primary instability waves associated with the rapidly growing second mode saturate. The flow then enters the nonlinear region and its initiation can be defined by the mere existence of second-mode harmonics which cannot be explained by linear stability theory. Harmonic generation is a classical indication that vortices are evolving, as shown by the author in rotating disk flow.[107] In view of this vortex generation process, the distortion of the contours in Figures 5.3 and 5.4, as x increases beyond 13 in., can be attributed to the large-scale swirling motion of the vortices. It should be noted that these harmonics grow quickly and saturate at about the same location where the primary instability waves saturate. Also, the low-frequency disturbances tend to saturate along with the second-mode disturbances and it is unclear why this occurs.

In the nonlinear region, secondary instabilities generally develop that cause two-dimensional disturbances to become three-dimensional; however, secondary instabilities and nonlinear breakdown are "completely open questions" in high-speed flows.[86] The distortion of the mean flow by the finite-amplitude primary instabilities in the nonlinear region renders the flow more unstable to inviscid instabilities. One recent theory,[108] based on a numerical investigation using the DNS approach, shows that oblique, finite-amplitude subharmonic instabilities can interact with second-mode instabilities and spawn other disturbances that will ultimately lead to a full turbulent spectrum of disturbances. In the cooled-cone data, there are no detectable subharmonic disturbances in the nonlinear region, so this potential transition mechanism does not seem a viable explanation in this case. The only growth in the nonlinear region is a generalized spectral broadening of the dominant frequency bands that evolved from the linear region. Due to its orientation with respect to the axisymmetric flow, the hot-wire sensor can only detect streamwise flow disturbances and is incapable of detecting possible azimuthal disturbances. Hence, the peculiar absence of a distinct and growing frequency band in the spectra taken in the nonlinear region suggests that the secondary instability may not have a significant streamwise component.

The author speculates that the spectral broadening in the nonlinear region may be due to a developing azimuthal mode secondary instability which may be distorting the developing vortices into a pattern similar to the K-type breakdown of Λ-vortices in the flow over a flat plate.[6] Although the distortion of the vortices could follow C-type or H-type patterns, streamwise variations would be present in the spectra in the form of growing subharmonic frequency bands, but there is no evidence of this. The highly speculative azimuthal vorticity pattern that develops is also shown in Fig. 7.1. At the end of the nonlinear region, the flow disturbances are thought to be a series of three-dimensional vortices.

After the nonlinear region, the "breakdown region" is identified in Fig. 7.1 where the spectra rapidly fills and a turbulent flow evolves. As the finite primary disturbances distorted the mean laminar flow and reduce its stability, the finite secondary disturbances distort the flow even further and reduce its stability to other opportunistic instability modes. In Fig. 5.18 a rapidly growing unknown flow disturbance was identified at 800kHz that grew as the spectra was filling. This coincidence leads the author to further speculate that the 800kHz disturbance could be a tertiary instability that interacts with the distorted vortices and ultimately leads to vortex breakdown. Unlike the possible azimuthal mode, this possible tertiary mode is detectable with the hot-wire sensor meaning that it has a streamwise component. Although a true "fully turbulent" flow was not documented in this experiment, the trend toward a turbulent flow at x=16.5 in. is unmistakable (see Fig. 5.9).

To summarize, distinct regions in the transition zone of a hypersonic boundary layer over a cooled cone have been identified. The linear region is rather large (about 8 in. in this case) but the "infinitesimal" amplitude of the disturbances prevents investigation of over half this region. The nonlinear region is small by comparison, about 2.5 in., and the hypothesized azimuthal secondary instability mode cannot be directly detected with the hot wire. It is significant to note that the peaks in cone wall temperature as documented in this experiment tended to occur near the end of the nonlinear region where the boundary layer vortices should have reached their maximum development just prior to breakdown. The final stage in the transition zone is the breakdown region, and the streamwise component of a possible tertiary instability has been identified in this experiment. The extent of the breakdown region has not been determined.

7.1.2 Linear Stability Theory

Reconciling LST predictions and the results of high-speed stability/transition tests in the past were greatly complicated by the transition-promoting effects of acoustic radiation from turbulent wind tunnel walls. In Fig. 7.2, the adiabatic-cone wall temperature is presented with the bleed valves of the M6NTC closed to allow fully turbulent flow on the nozzle wall and thereby create a high-amplitude freestream noise field. Using the location of maximum wall temperature as a guide, the "transition" of the cone moves upstream to x=11.5 in. where N=5.5 (see Fig. 4.13) under this "noisy" flow condition. This transition N-factor is comparable to that found in a conventional tunnel.[19] In the quiet tunnel with the bleed valves open and the freestream noise field as presented in Chapter 3, the transition point moves to x=16 in., as seen in Fig. 4.1, where N=10.5. So by changing the flow over the nozzle walls from turbulent to laminar, the transition N-factor can be nearly doubled. This example illustrates the fact that boundary-layer transition depends heavily on the freestream noise level and highlights the difficulty previous researchers have had in trying to reconcile low N-factor "noisy" transition data with the usual transition N-factor of 9 to 11.

To show the validity of applying LST to predict high-speed flow transition, Fig. 7.3 is presented which compares experimental data from the quiet tunnel with LST predictions. In this figure, the adiabatic-cone results of Fig. 4.13, the cooled-cone results of Fig. 5.13, and another adiabatic-wall data set for cone 93-10 are compared with their respective theoretical growth predictions. The 93-10 cone was investigated on the final day of testing in the M6NTC since LST predictions were known for this cone geometry[14] as well as the 91-6 cone geometry. As shown, the primary instabilities in the 91-6 and 93-10 cone boundary layers under adiabatic-wall conditions both saturate at N=9. Under the cooled-wall conditions, the 91-6 cone boundary layer saturates at N=11. These N values compare favorably with the N=10 factor that can be used in subsonic, transonic, and supersonic transition under low freestream noise conditions.[5] To facilitate future comparisons, the dimensional growth rates of the experimental data in Fig. 7.3 are shown in Fig. 7.4 with third-order polynomials fit to the data. Hence, the results of this experiment show the ability of LST to "predict" the transition of hypersonic boundary layers using the usual N=10 guideline in a low-noise environment.

7.1.3 Quiet Tunnels

Quiet tunnels were developed so that the growth of disturbances in a high-speed boundary layer under low freestream noise conditions could be investigated. As explained in the previous section, use of the quiet tunnel has facilitated the confirmation of LST as an inexpensive transition-prediction tool using the same N=10 guideline in high-speed flows as is used in other flow regimes. Moreover, since the cooled-wall trends match the predicted trends; e.g., transition moves upstream with wall cooling, this quiet tunnel experiment has confirmed the trends Stetson[80] recently documented for a cooled-wall and has shown that previous hypersonic transition experiments[35] showing contrary transition trends were somehow compromised.

The use of a quiet tunnel has also raised fundamental questions related to the receptivity of high-speed boundary layers due to the nature of the second-mode wave packets. Receptivity refers to the mechanisms in the boundary layer that internalize environmental disturbances and generate unstable waves.[5] In Chapter 3, it was shown that there are no detectable second-mode frequencies in the freestream above the cone boundary layers, yet an interesting set of second-mode frequencies exist in the boundary layers. In this experiment, the primary instabilities were seen to grow as well-defined wave packets composed of two or three discrete frequencies from the set of 275, 291, 306, and 320 kHz depending on wall conditions. These frequencies could be considered higher harmonics of a relatively low 14.55 kHz frequency which is detectable in the freestream near the location where the second-mode disturbances are first measurable in the boundary layer. The well-defined wave-packet frequencies identified in this experiment using the quiet tunnel have not been reported in experiments using conventional tunnels, although wave-packet features have.[104] Changing the A-O-A slightly in this experiment changed the orientation of the cone boundary layer to the noise field, resulting in a wave packet with frequencies of 299 and 311 kHz, which could be harmonics of 11.96 kHz, not 14.55 kHz. If the discrete frequency composition of the wave packets were due to a systematic experimental error, then the fundamental harmonic frequency should have been maintained. To investigate the low-frequency source that could be generating harmonics into the second-mode frequency range, the low-frequency bands associated with the spectral data in Fig. 6.10 are shown in Fig. 7.5. Comparing the low frequencies, it is clear that the two curves have different roll-off frequencies that appear to be related the aforementioned "fundamental" of the second-mode wave-packet frequencies (14.55 kHz for zero A-O-A and 11.96 kHz for the 0.32° A-O-A). The possible harmonic relationship between low-frequency freestream disturbances and the clearly defined second-mode wave-packet frequencies in this experiment is unclear but could be the result of an unknown receptivity mechanism unique to high-speed boundary layers.

There is another noteworthy issue related to low-frequency disturbances in the boundary layers growing under quiet conditions. In most high-speed experiments conducted in conventional tunnels, the freestream noise field is roughly constant, which results in a saturated low frequency band in the spectra.[76] However, in this experiment, the amplitude of the freestream noise increases with downstream distance. In Fig. 7.6, disturbance growth for the lowest frequency investigated (15kHz) is presented in the cooled-wall and adiabatic-wall cone boundary layers and in the freestream. As shown, the boundary layers both show 15 kHz amplitude levels that are higher than the freestream level for all x, meaning that these disturbances are being internalized at a rate greater than the damping rate for this frequency. However, the cooled wall amplitudes are everywhere higher than the adiabatic wall amplitudes which suggests that the thinner cooled-wall boundary layer with faster growing disturbances is more "receptive" to the freestream noise than is the adiabatic-wall boundary layer. Since the geometry of the cone model includes a flare, there is the possibility that the growth of the lowest frequencies could be related to the growth of Görtler vortices. However, if this were the case, then the Görtler instabilities were growing near the rate of the second mode, and this is highly unlikely. Hence, the developing noise field in the quiet tunnel shows that low-frequency disturbances grow faster in the cooled-wall case than in the adiabatic-wall case.

To summarize, the quiet tunnel has provided a low-disturbance environment whereby the author was able to verify the validity of LST and its transition prediction capability, but the use of the quiet tunnel has also raised interesting issues related to the receptivity of high-speed boundary layers. For instance, (1) it is still unclear if and how low-frequency freestream noise evolves into high-frequency second-mode disturbances and (2) the faster growth of low frequencies in the cooled-wall case can not be readily explained.

7.2 Conclusions

The stability of the hypersonic boundary layer over a flared cone under adiabatic and cooled wall conditions has been investigated with $Re_\infty = 2.85 \times 10^6$/ft. in a quiet flow. Following are the significant conclusions related to this experiment:

1) The freestream above the boundary layer was found to be "quiet" up to x=12.5 in.
2) The development of the freestream noise field followed typical trends with the lowest frequencies having the highest amplitudes and nowhere was there a measurable second-mode frequency in the freestream.

3) In the linear region, the wall pressure and boundary-layer thicknesses in the adiabatic- and cooled-wall cases compared well with the LST predictions.

4) In the adiabatic- and cooled-wall cases, the second-mode disturbances were found to be composed of well-defined wave-packet frequencies.

5) In the adiabatic-wall case, the second-mode wave-packet frequencies were 275 and 291 kHz and grew, following the 270 kHz trend predicted by LST, up to N=9.

6) In the cooled-wall case, the second-mode wave-packet frequencies were 291, 306, and 320 kHz. Disturbances at the dominant frequency of 306 kHz grew, following the trend for 310 kHz predicted by LST, up to N=11.

7) The "transition" of the linear disturbances at N=9 and N=11 showed that the N=10 LST transition-prediction guideline applies to hypersonic flows under low freestream noise conditions.

8) In the nonlinear region, harmonics of the second mode saturated and it was speculated that azimuthal secondary instabilities could be growing and distorting the developing vortices.

9) In the cooled-wall case, a breakdown region was identified as well as a possible tertiary instability with a streamwise component at 800 kHz.

10) The low frequencies associated with freestream noise grew more rapidly in the cooled-wall case than in the adiabatic-wall case.

11) There was a slow-growing first mode at 50kHz found in the cooled-wall case, but no distinct first mode was found in the adiabatic-wall case.

12) A peak in cone wall temperature was seen to occur near the end of the nonlinear region where the vortices were expected to have achieved maximum development just prior to breakdown.

13) The boundary-layer flow was shown to be very sensitive to angle-of-attack variations with the second-mode wave-packet frequencies tuning to the boundary-layer thickness.

7.3 Recommendations for Future Research

From an engineering perspective, this experiment has proven the validity of applying LST and the N=10 transition criterion to hypersonic flows. In regards to the details of transition in hypersonic flows, it is recommended that the development of the potential azimuthal mode secondary instabilities in the nonlinear region be a focus of future research. An experiment to study this phenomenon would be much more complicated than the present experiment due to the required use of multiple hot-wires to capture the developing three-dimensionality of the flow. The extent of the breakdown region should also be defined in future work and potential tertiary instabilities should be investigated; however, the hot-wire sensing material and/or wire diameter will need to be changed to withstand the increased dynamic loads.

Quiet tunnels and their unique low-disturbance freestreams are highly recommended for certain types of high-speed experiments. Receptivity is still an open issue in experimental hypersonic flows and the only facilities recommended for these sensitive studies are quiet tunnels. In this experiment the initial disturbances were "natural," but if other experiments are to be conducted to investigate the stability of hypersonic flow to low-amplitude, controlled disturbances; e.g., spark-induced oblique waves, the most suitable facility for such an experiment is the quiet tunnel.

The prototype constant-voltage anemometer has proven to be a useful tool in investigating the hypersonic flow in a facility with an intense electronic noise field that has limited the usefulness of other anemometers. It is highly recommended that CVA development continue with the goals of producing an instrument with even higher bandwidth and sensitivity. CVA is recommended to be the "first choice" anemometer for future high-speed stability or receptivity investigations.

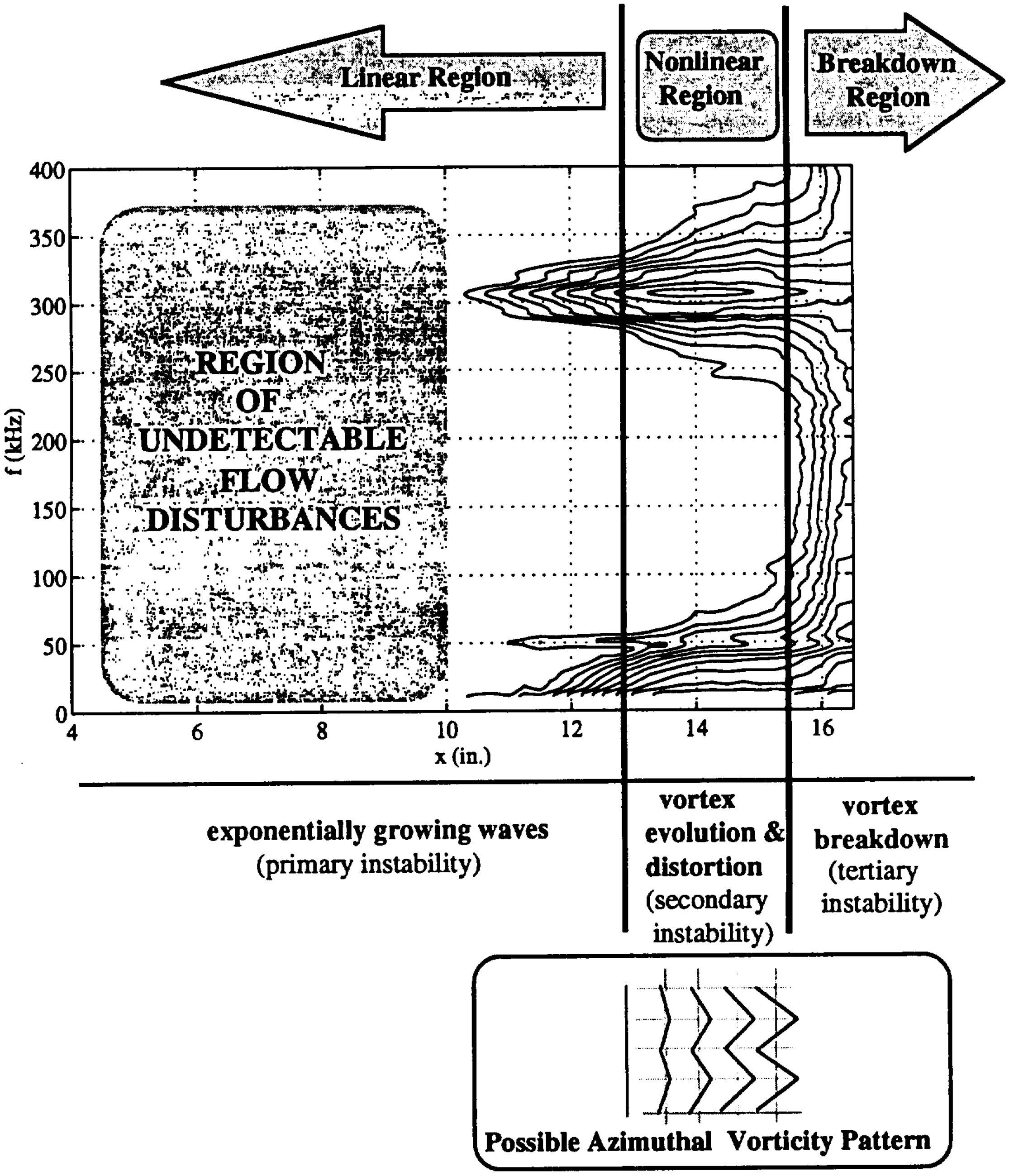

Figure 7.1 Identifiable Flow Regions for a Hypersonic Flow Undergoing Transition (Contour Plot of Cooled Cone data previously presented in Fig. 5.11)

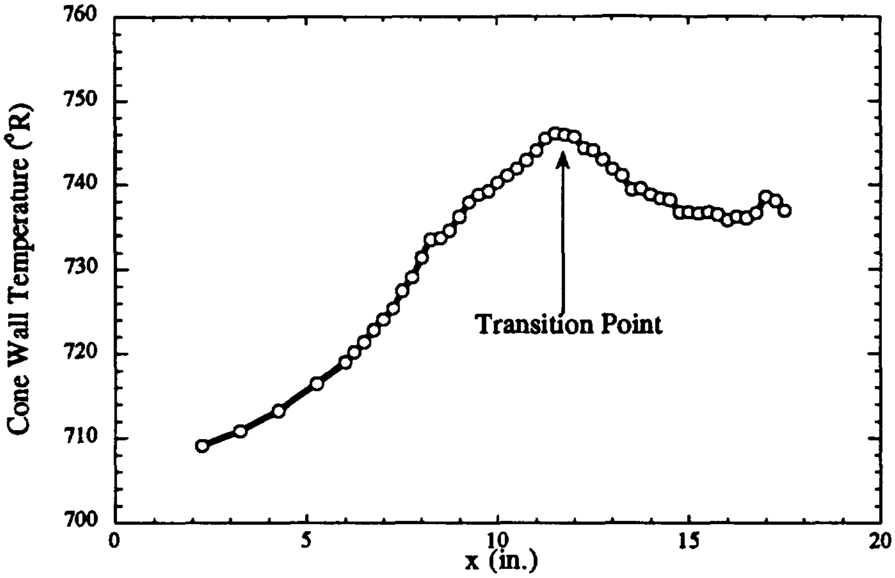

Figure 7.2 Wall Temperature of the Adiabatic Cone with High Noise Level

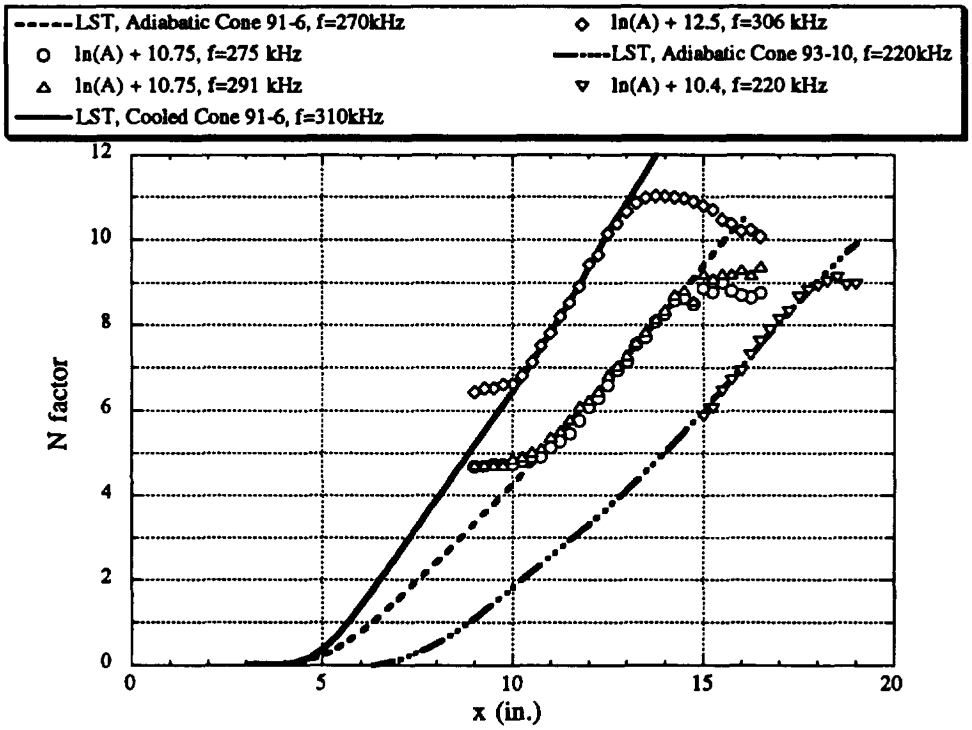

Figure 7.3 Growth Plot for all Experimental Data

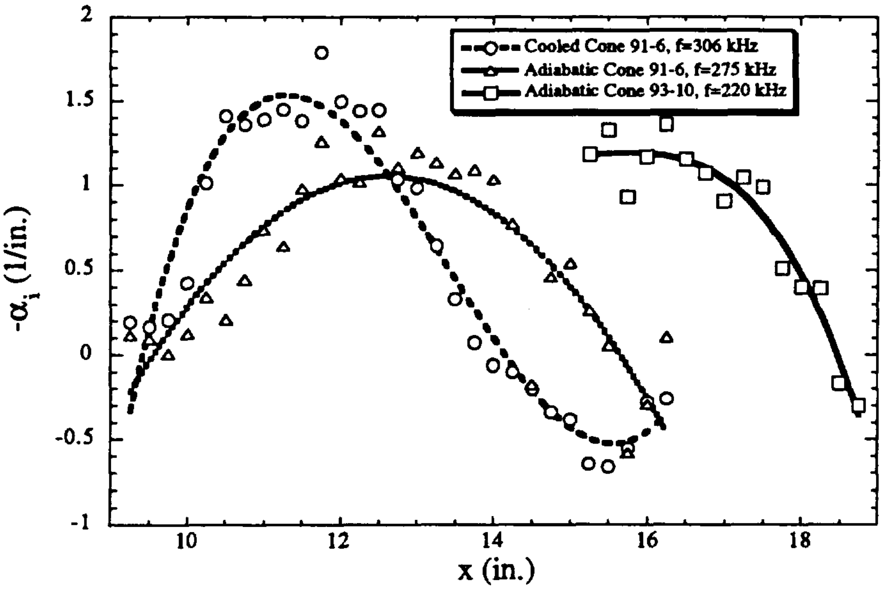

Figure 7.4 Dimensional Growth Rates from Fig. 7.3

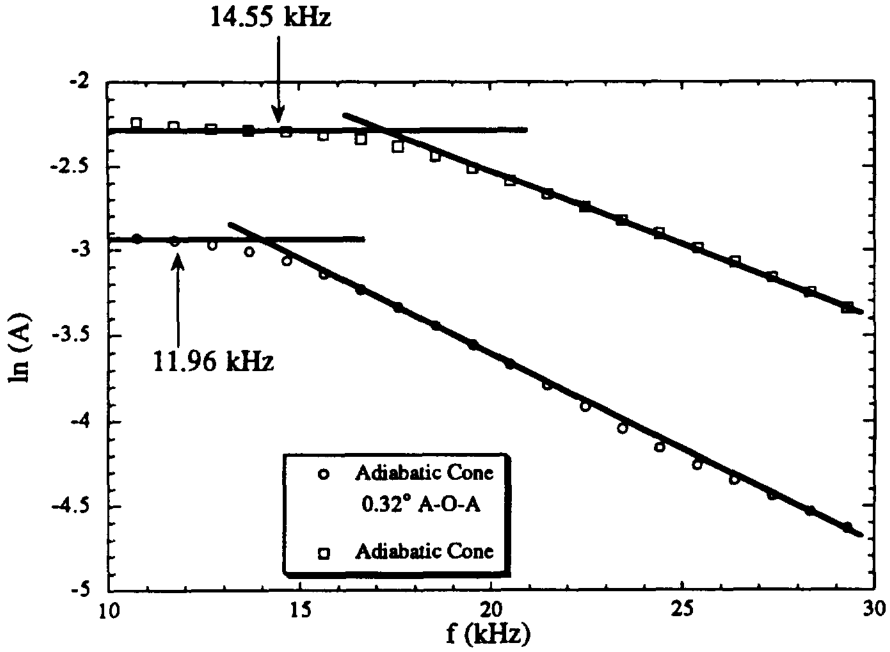

Figure 7.5 Low-Frequency Data Associated with Fig. 6.10 Spectra

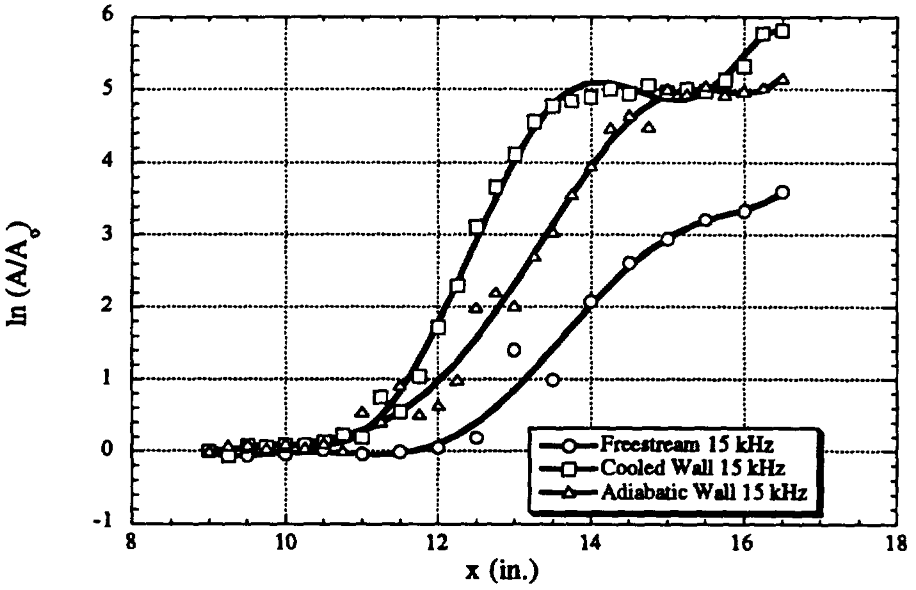

Figure 7.6 The Growth of Disturbances at 15kHz

REFERENCES

1. Mehta, Unmeel B., "Air-Breathing Aerospace Plane Development Essential: Hypersonic Propulsion Flight Tests," NASA Technical Memorandum 108857, November 1994.

2. Reshotko, Eli, "Stability Theory as a Guide to the Evaluation of Transition Data," *AIAA Journal*, Vol. 7, No. 6, pp. 1086-1091.

3. Herbert, T., "Secondary Instability of Boundary Layers," *Annual Review of Fluid Mechanics*, Vol. 20, 1988, pp. 487-526.

4. Ng, Lian and Erlebacher, Gordon, "Secondary Instabilities in Compressible Boundary Layers," Phys. Fluids A, Vol. 4, No. 4, April 1992, pp. 710-726.

5. Arnal, D., "Boundary Layer Transition: Predictions Based on Linear Theory," AGARD-VKI Special Course on 'Progress in Transition Modeling', March-April 1993.

6. White, F.M., *Viscous Fluid Flow*, McGraw-Hill, New York, 1991.

7. Mack, L., "Boundary Layer Stability Theory," Jet Propulsion Laboratory Report no. 900-277, Rev. A., Pasadena, California, 1969.

8. Mack, L., "Boundary-Layer Linear Stability Theory," Special Course on Stability and Transition of Laminar Flow, AGARD-R-709.

9. Malik, M.R., "Numerical Methods for Hypersonic Boundary Layer Stability," *Journal of Computational Physics*, Vol. 86, No. 2, February 1990, pp. 376-413.

10. Stuckert, G. and Reed, H., "Linear Stability of Supersonic Cone Boundary Layers," AIAA Journal, Vol. 30, No. 10, October 1992, pp. 2402-2410.

11. Lees L., and Lin, C., *Investigation of the Stability of the Laminar Boundary Layer in a Compressible Fluid*, NACA TN no. 1115, 1946.

12. Lees, L., The Stability of the Laminar Boundary Layer in a Compressible Fluid, NACA Technical Report no. 876, 1947.

13. Pruett, C. and Chang, C., "A Comparison of PSE and DNS for High-Speed Boundary-Layer Flows," FED-Vol. 151, Transitional and Turbulent Compressible Flows, ASME, 1993, pp. 57-67.

14. Balakumar, P. and Malik, M.R., "Effect of Adverse Pressure Gradient and Wall Cooling on Instability of Hypersonic Boundary Layers," High Technology Corporation, High Technology Report no. HTC-9404, March 1994.

15. Malik, M., "e^{Malik}: A New Spatial Stability Analysis Program for Transition Prediction using the e^N Method," High Technology Report No. HTC-9203.

16. Smith, A.M.O., "The Boundary Layer and I," *AIAA Journal*, Vol. 19, No. 11, November 1981, pp. 1377-1385.

17. Jaffe, N.A., Okamura, T. and Smith A.M.O., "Determination of Spatial Amplification Factors and Their Application to Predicting Transition," *AIAA Journal*, Vol. 8, No. 2, February, 1970, pp. 301-308.

18. Malik, Mujeeb R., "Prediction and Control of Transition in Supersonic and Hypersonic Boundary Layers," *AIAA Journal*, Vol. 27, No. 11, November 1989, pp. 1487-1493.

19. Mack, L., "Stability of Axisymmetric Boundary Layers on Sharp Cones at Hypersonic Mach Numbers", AIAA Paper 87-1413, Honolulu, Hawaii, 1987.

20. Morkovin, Mark V., "On Transition Experiments at Moderate Supersonic Speeds," *Journal of the Aeronautical Sciences*, Vol. 24, No. 7, July 1957, pp. 480-486.

21. Morkovin, M.V., "On Supersonic Wind Tunnels with Low Free-Stream Disturbances," *Journal of Applied Mechanics*, September 1959, pp. 319-324.

22. Laufer, John, "Aerodynamic Noise in Supersonic Wind Tunnels," *Journal of the Aeronautical Sciences*, Vol. 28, No. 9, September 1961, pp. 685-692.

23. Laufer, John, "Some Statistical Properties of the Pressure Field Radiated by a Turbulent Boundary Layer," *The Physics of Fluids*, Vol. 7, No. 8, August 1964, pp. 1191-1197.

24. Pate, S.R., and Schueler, C.J., "Radiated Aerodynamic Noise Effects on Boundary-Layer Transition in Supersonic and Hypersonic Wind Tunnels," *AIAA Journal*, Vol. 7, No. 3, March 1969, pp. 450-457.

25. Pate, S.R., "Measurements and Correlations of Transition Reynolds Numbers on Sharp Slender Cones at High Speeds," *AIAA Journal*, Vol. 9, No. 6, June 1971, pp. 1082-1090.

26. Kovasnay, L.S.G., "Turbulence in Supersonic Flow," *Journal of the Aeronautical Sciences*, Vol. 20, No. 10, October 1953, pp. 657-682.

27. Laufer, J., "Factors Affecting Transition Reynolds Numbers on Models in Supersonic Wind Tunnels, *Journal of the Aeronautical Sciences*, Vol. 21, No. 7, July 1954, pp. 497-498.

28. Beckwith, I.E., Chen, F.-J., Wilkinson, S.P., Malik, M.R., and Tuttle, D., "Design and Operational Features of Low-Disturbance Wind Tunnels at NASA Langley for Mach Numbers from 3.5 to 18," AIAA Paper 90-1391.

29. Wilkinson, S.P.; Anders, S.G.; Chen, F.-J. and Beckwith, I.E., "Supersonic and Hypersonic Quiet Tunnel Technology at NASA Langley," AIAA Paper 92-3908.

30. Wilkinson, S.P., Anders, S.G., Chen, F.-J., and White, J.A., "Status of NASA Langley Quiet Flow Facility Developments," AIAA Paper 94-2498.

31. Beckwith, I.E., "Development of a High Reynolds Number Quiet Tunnel for Transition Research," *AIAA Journal*, Vol. 13, No. 3, March 1975, pp. 300-306.

32. Anders, J.B., Stainback, P.C., Keefe, L.R., and Beckwith, I.E., "Fluctuating Disturbances in a Mach 5 Wind Tunnel," Presented at the AIAA Ninth Aerodynamic Testing Conference, Arlington, Texas, June 7-9, 1976.

33. Chen, Fang-Jeng and Wilkinson, Stephen P., "Görtler Instability and Hypersonic Quiet Nozzle Design," Journal of Spacecraft and Rockets, Vol. 30, No. 2, March-April 1993, pp. 170-175.

34. Blanchard, A., Lachowicz, J., and Wilkinson, S., "Performance of the NASA-Langley Mach 6 Nozzle Test Chamber Facility," AIAA Paper 96-0441, Reno, Nevada, 1996.

35. Potter, J., "Review of the Influence of Cooled Walls on Boundary-Layer Transition," *AIAA Journal*, Vol. 18, No. 8, pp. 1010-1012.

36. Scherrer, Richard, "Comparison of Theoretical and Experimental Heat-Transfer Characteristics of Bodies of Revolution at Supersonic Speeds," NACA Report TR-1055, 1951.

37. Scheerer, Richard, and Gowen, Forest E., "Comparison of Theoretical and Experimental Heat Transfer on a Cooled 20° Cone with Laminar Boundary Layer at a Mach Number of 2.02," NACA TN 2087, 1950.

38. Scheerer, Richard, "Boundary-Layer Transition on a Cooled 20° Cone at Mach Numbers of 1.5 and 2.0," NACA TN 2131, 1950.

39. Eber, G.R., "Recent Investigation of Temperature Recovery and Heat Transmission on Cones and Cylinders in Axial Flow in the N.O.L. Aeroballistics Wind Tunnel," *Journal of the Aeronautical Sciences*, Vol. 19, No. 1, January 1952, pp. 1-6.

40. DeLaurer, R.D. and Nagamatsu, H.T., "Experimental Investigation of Heat Transfer at Hypersonic Mach Number," California Institute of Technology, 1953.

41. Czarnecki, K.R., "An Investigation of the Effects of Heat Transfer on Boundary-Layer Transition on a Parabolic Body of Revolution (NACA RM-10) at a Mach Number of 1.61," NACA Report 1240, 1955.

42. Jack, John R., and Diaconis, N.S., "Variation of Boundary-Layer Transition and Heat Transfer on Two Bodies of Revolution at a Mach Number of 3.12," NACA TN 3562, 1955.

43. Jack, John R., and Diaconis, N.S., "Heat-Transfer Measurements on Two Bodies of Revolution at a Mach Number of 3.12. " NACA TN 3776, 1956.

44. Diaconis, N.S., Jack, John R., and Wisniewski Richard J., "Boundary-Layer Transition at Mach 3.12 as Affected by Cooling and Nose Blunting," NACA TN 3928, 1957.

45. Van Driest, E.R. and Boison, Christopher J., "Experiments on Boundary-Layer Transition at Supersonic Speeds," *Journal of the Aeronautical Sciences*, Vol. 24, No. 12, December 1957, pp. 885-899.

46. Jack, John R., Wisniewski Richard J., and Diaconis, N.S., "Effects of Extreme Cooling on Boundary-Layer Transition," NACA TN 4094, 1957.

47. Stetson, Kenneth F., "Boundary-Layer Transition on Blunt Bodies with Highly Cooled Boundary Layers," *Journal of The Aero/Space Sciences*, Vol. 27, No. 2, February 1960, pp. 81-91.

48. Wisniewski, Richard, J. and Jack, John R., "Recent Studies on the Effect of Cooling on Boundary-Layer Transition at Mach 4," *Journal of the Aerospace Sciences*, Vol. 28, No. 3, March 1961, pp. 250-251.

49. Potter, J. Leith and Whitfield, Jack D., "The Relation Between Wall Temperature and the Effect of Roughness on Boundary-Layer Transition," *Journal of the Aerospace Sciences*, Vol. 28, No. 8, August 1961, pp. 663-664.

50. Brinich, Paul F., "Recovery Temperature, Transition, and Heat-Transfer Measurements at Mach 5," NASA TN D-1047, 1961.

51. Zakkay, Victor, "Laminar, Transitional, and Turbulent Heat transfer to a Cone-Cylinder-Flare Body at Mach 8.0," *Journal of the Aerospace Sciences*, Vol. 29, No. 12, December 1962, pp. 1403-1413.

52. Schmotolocha, S.N. and Himka, T., "Experimental Investigations of Heat Transfer and Pressure Distributions for Conical and Elliptical Slender Bodies at Mach 10," Republic Aviation Corporation, RAC 2368 under Contract No. AF33(657)-9697, May 1964.

53. Sanator R.J., DeCarlo J.P., and Torrillo D.T., "Hypersonic Boundary-Layer Transition Data for a Cold-Wall Slender Cone," *AIAA Journal*, Vol. 3, No. 4, April 1965, pp. 758-760.

54. Henderson, A., Rogallo, R.S., and Woods, W.C., "Exploratory Hypersonic Boundary-Layer Transition Studies," *AIAA Journal*, Vol. 3, No. 7, July 1965, pp. 1363-1364.

55. Nagasmatsu, H.T., Sheer R.E., and Wisler, D.C., "Wall Cooling Effects on Hypersonic Boundary Layer Transition, M_1=7.5-15," BSD-TR-229, August 1966.

56. McCauley, W.D., Saydah A.R., and Bueche, J.F., "Effect of Spherical Roughness on Hypersonic Boundary-Layer Transition," *AIAA Journal*, Vol. 4, No. 12, December 1966, pp. 2142-2148.

57. Richards, B.E. and Stollery, J.L., "Further Experiments on Transition Reversal at Hypersonic Speeds," *AIAA Journal*, Vol. 4, No. 12, December 1966, pp. 2224-2226.

58. Stetson, Kenneth F. and Rushton, George H., "Shock Tunnel Investigation of Boundary-Layer Transition at M=5.5," *AIAA Journal*, Vol. 5, No. 5, May 1967, pp. 899-906.

59. Everhart, Philip E. and Hamilton, Harris H., "Experimental Investigation of Boundary-Layer Transition on a Cooled 7.5° Total-Angle Cone," NASA TN D-4188, 1967.

60. Cary, Aubrey M., "Turbulent Boundary-Layer Heat Transfer and Transition Measurements for Cold-Wall Conditions at Mach 6," *AIAA Journal*, Vol. 6, No. 5, May 1968, pp. 958-959.

61. Maddalon, Dal V., "Effect of Varying Wall Temperature and Total Temperature on Transition Reynolds Number at Mach 6.8," *AIAA Journal*, Vol. 7, No. 12, December 1969, pp. 780-781.

62. Rhudy, J.P., "Effect of Uncooled Leading Edge on Cooled-Wall Hypersonic Flat-Plate Boundary-Layer Transition," *AIAA Journal*, Vol. 8, No. 3, March 1970, pp. 576-577.

63. Mateer, George G., "Effects of Wall Cooling and Angle of Attack on Boundary-Layer Transition on Sharp Cones at M_∞=7.4," NASA TN D-6908, 1972.

64. Fischer, Michael C., "Influence of Moderate Wall Cooling on Cone Transition at M_e=13.7 in Helium," *Journal of Spacecraft and Rockets*, Vol. 10, No. 4, April 1973, pp. 282-283.

65. Potter, J. Leith, "Boundary-Layer Transition on Supersonic Cones in an Aeroballistic Range," *AIAA Journal*, Vol. 13, No. 3, March 1975, pp. 270-277.

66. Watson, Ralph D., "Wall Cooling Effects on Hypersonic Transitional/Turbulent Boundary Layers at High Reynolds Numbers," *AIAA Journal*, Vol. 15, No. 10, October 1977, pp. 1455-1461.

67. Nagamatsu, H.T., Sheer, R.E., and Wisler, D.C., "Wall Cooling Effects on Hypersonic Boundary Layer Transition, M_1=7.5 - 15," AIAA Paper 86-1088, May 1986.

68. Kimmel, R.L., "Experimental Transition Zone Lengths in Pressure Gradient in Hypersonic Flow," FED-Vol. 151, Transitional and Turbulent Compressible Flows, ASME, 1993, pp. 117-127.

69. Schubauer, G.B. and Skramstad, H.K., "Laminar Boundary Layer Oscillations and Transition on a Flat Plate," NACA TR 909, 1948.

70. Demetriades, A., "An Experimental Investigation of the Stability of the Laminar Hypersonic Boundary Layer," GALCIT Hypersonic Research Project, Memorandum No. 43, 1958.

71. Demetriades, A., "An Experiment on the Stability of Hypersonic Laminar Boundary Layers," *Journal of Fluid Mechanics*, Vol. 7, Part 3, March 1960, pp. 385-396.

72. Kendall, J.M., "Supersonic Boundary Layer Stability Experiments, " Proceedings of Boundary Layer Transition Study Group Meeting, Vol. II, Aerospace Corporation, August 1967.

73. Kendall, J.M., "Wind Tunnel Experiments Relating to Supersonic and Hypersonic Boundary-Layer Transition," *AIAA Journal*, Vol. 13, No. 3, March 1975, pp. 290-299.

74. Demetriades, A., "Boundary Layer Instability Observations at Mach Number 7," Journal of Applied Mechanics, ASME, Vol. 99, No. 1, March 1977.

75. Demetriades, A., "New Experiments on Hypersonic Boundary Layer Stability Including Wall Temperature Effects," Proceedings of the Heat Transfer and Fluid Mechanics Institute, pp. 39-54, 1978.

76. Stetson, K., Thompson, E., Donaldson, J. and Siler, L., "Laminar Boundary Layer Stability Experiments on a Cone at Mach 8, Part 1: Sharp Cone," AIAA Paper 83-1761, Danvers, Massachusetts, 1983.

77. Stetson, K.F., Thompson, E.R., Donaldson, J.C., and Siler, L.G., "Laminar Boundary Layer Stability Experiments on a Cone at Mach 8, Part 2: Blunt Cone," AIAA Paper 84-006, January 1984.

78. Stetson, K.F., Thompson, E.R., Donaldson, J.C., and Siler, L.G., "Laminar Boundary Layer Stability Experiments on a Cone at Mach 8, Part 3: Sharp Cone at Angle of Attack," AIAA Paper 85-0492, January 1985.

79. Stetson, K.F., Thompson, E.R., Donaldson, J.C., and Siler, L.G., "Laminar Boundary Layer Stability Experiments on a Cone at Mach 8, Part 4: On Reynolds Number and Environmental Effects," AIAA Paper 86-1087, May 1986.

80. Stetson, K., Thompson, E. and Donaldson, J., "Laminar Boundary Layer Stability Experiments On a Cone at Mach 8, Part 5: Tests with a Cooled Model," AIAA Paper 89-1895, Buffalo, New York, 1989.

81. Stetson, K.F., Thompson, E.R., Donaldson, J.C. and Siler, L.G., "On Hypersonic Transition Testing and Prediction," AIAA Paper 88-2007.

82. Stetson, Kenneth F. and Kimmel Roger L., "Example of Second-Mode Instability Dominance at a Mach Number of 5.2," AIAA Journal, Vol. 30, No. 12, December 1992, pp. 2974-2976.

83. Stetson, K. and Kimmel, R., "Surface Temperature Effects on Boundary-Layer Transition," *AIAA Journal,* Vol. 30, No. 11, pp. 2782-2783.

84. Stetson, K., "On Nonlinear Aspects of Hypersonic Boundary-Layer Stability," AIAA Journal, Vol. 26, No. 7, July 1988, pp. 883-885.

85. Stetson, K.F., Thompson, E.R., Donaldson, J.C., and Siler, L.G., "A Comparison of Planar and Conical Boundary Layer Stability and Transition at a Mach Number of 8," AIAA Paper 91-1639, June 1991.

86. Stetson, K. and Kimmel R., "On Hypersonic Boundary-Layer Stability," AIAA Paper 92-0737, Reno, Nevada, January 1992.

87. El-Hady, Nabil, M., "Secondary Instability of High-Speed Flows and the Influence of Wall Cooling and Suction," *Phys. Fluids A*, Vol. 4, No. 4, April 1992, pp. 727-743.

88. Ng, Liam L. and Zang, Thomas A., "Secondary Instability Mechanisms in Compressible Axisymmetric Boundary Layers," *AIAA Journal*, Vol. 31, No. 9, September 1993, pp. 1605-1610.

89. Chang, C-L., Malik M.R., Erlebacher, G. and Hussaini, M.Y., "Compressible Stability of Growing Boundary Layers Using Parabolized Stability Equations," AIAA Paper 91-1636, Honolulu, Hawaii, 1991.

80. Chen, F. -J., Malik, M.R. and Beckwith, I.E., "Comparison of Boundary Layer Transition on a Cone and Flat Plate at Mach 3.5," AIAA Paper 88-0411, Reno, Nevada, 1988.

91. Goldstein, Richard, J., *Fluid Mechanics Measurements*, Hemisphere Publishing Corporation, New York, 1983.

92. Perry, A.E., Smits, A.J. and Chong, M.S., "The Effects of Certain Low-Frequency Phenomena on the Calibration of Hot Wires," *Journal of Fluid Mechanics*, Vol. 90, Part 3, pp. 415-431.

93. Smits, A.J., Hayakawa, K. and Muck, K.C., "Constant Temperature Hot-Wire Anemometer in Practice in Supersonic Flows," *Experiments in Fluids*, Springer-Verlag, 1983.

94. Ko, C.L., McLaughlin, D.K., and Troutt, T.R., "Supersonic Hot-Wire Fluctuation Data Analysis with a Conduction End-Loss Correction," *Journal of Physics E: Sci. Instrum.*, Vol. 11, 1978, pp. 488-494.

95. Morkovin, M., *Fluctuations and Hot-Wire Anemometry in Compressible Flow*, AGARDograph 24, 1956.

96. Anders, John B., "Turbulence Measurements in Hypersonic, Helium Flow," Princeton University, USAF Report 1157, February 1974.

97. Analytical Services and Materials, Inc., High Sensitivity, Large Bandwidth Constant Voltage Anemometer for High Speed Transition Research, NASA LaRC SBIR Number 92-1 02.07, Phase I Report, August 1993.

98. Sarma, Garimella, "Analysis of a Constant Voltage Anemometer Circuit," IEEE/IMTA Conference, Irvine CA, May 18-29, 1993.

99. Mangalam, S.M., Sarma, G.R., Kuppa, S., and Kubendran, L.R., "A New Approach to High-Speed Flow Measurements Using Constant Voltage Anemometry," AIAA Paper 92-3957.

100. Kuppa, S., Sarma, G.R. and Mangalam, S.M., "Effect of Thermal Inertia on the Frequency Response of Constant Voltage Hot Wire Anemometry and Its Compensation," FED-Vol. 161, *Fluid Measurement and Instrumentation*, ASME 1993, pp. 67-73.

101. Anderson, J.D., *Modern Compressible Flow*, McGraw-Hill, New York, 1982.

102. Ames Research Staff, "Equations, Tables, and Charts for Compressible Flow," NACA Report 1135, 1953.

103. Schlichting, H., *Boundary Layer Theory*, 7th ed., McGraw-Hill, New York, 1987.

104. Kimmel, R., Demetriades, A. and Donaldson, J., "Space-Time Correlation Measurements in a Hypersonic Transitional Boundary Layer," AIAA Paper 95-2292, San Diego, California, June 1995.

105. Kimmel, R. and Kendall, J., "Nonlinear Disturbances in a Hypersonic Laminar Boundary Layer," AIAA Paper 91-0320, Reno, Nevada, 1991.

106. Anderson, J.D., *Hypersonic and High-Temperature Gas Dynamics*, McGraw-Hill, New York, 1989.

107. Blanchard, A., "Experimental Investigation of Crossflow Instability Waves in Rotating-Disk Flow," Masters Thesis, Old Dominion University, 1992.

108. Pruett, C.D. and Zang, T.A., "Direct Numerical Simulation of Laminar Breakdown in High-Speed, Axisymmetric Boundary Layers," AIAA Paper 92-0742, Reno, Nevada, 1992.

REPORT DOCUMENTATION PAGE

Form Approved
OMB No. 0704-0188

1. AGENCY USE ONLY *(Leave blank)*

2. REPORT DATE
February 1996

3. REPORT TYPE AND DATES COVERED
Contractor Report

4. TITLE AND SUBTITLE
An Experimental Investigation of Wall-Cooling Effects on Hypersonic Boundary-Layer Stability in a Quiet Wind Tunnel

5. FUNDING NUMBERS
NCC1-180
505-59-50-02

6. AUTHOR(S)
Alan E. Blanchard and Gregory V. Selby

7. PERFORMING ORGANIZATION NAME(S) AND ADDRESS(ES)
Old Dominion University
Norfolk, VA 23508

8. PERFORMING ORGANIZATION REPORT NUMBER

9. SPONSORING/MONITORING AGENCY NAME(S) AND ADDRESS(ES)
National Aeronautics and Space Administration
Langley Research Center
Hampton, VA 23681-0001

10. SPONSORING/MONITORING AGENCY REPORT NUMBER
NASA CR-198287

11. SUPPLEMENTARY NOTES
Langley Technical Monitor: Stephen P. Wilkinson
Final Report

12a. DISTRIBUTION/AVAILABILITY STATEMENT
Unclassified–Unlimited
Subject Category 02

12b. DISTRIBUTION CODE

13. ABSTRACT *(Maximum 200 words)*

One of the primary reasons for developing quiet tunnels is for the investigation of high-speed boundary-layer stability and transition phenomena without the transition-promoting effects of acoustic radiation from tunnel walls. In this experiment, a flared-cone model under adiabatic- and cooled-wall conditions was placed in a calibrated, "quiet" Mach 6 flow and the stability of the boundary layer was investigated using a prototype constant-voltage anemometer. The results of this experiment were compared with linear-stability theory predictions and good agreement was found in the prediction of second-mode frequencies and growth. In addition, the same "N=10" criterion used to predict boundary-layer transition in subsonic, transonic, and supersonic flows was found to be applicable for the hypersonic flow regime as well. Under cooled-wall conditions, a unique set of continuous spectra data was acquired that documents the linear, nonlinear, and breakdown regions associated with the transition of hypersonic flow under low-noise conditions.

14. SUBJECT TERMS
Stability; Transition; Quiet wind tunnel; Linear stability theory; Hypersonic; Second mode; Constant-voltage anemometry; e^N

15. NUMBER OF PAGES
115

16. PRICE CODE
A06

17. SECURITY CLASSIFICATION OF REPORT	18. SECURITY CLASSIFICATION OF THIS PAGE	19. SECURITY CLASSIFICATION OF ABSTRACT	20. LIMITATION OF ABSTRACT
Unclassified	Unclassified	Unclassified	

NSN 7540-01-280-5500

Standard Form 298 (Rev. 2-89)
Prescribed by ANSI Std. Z39-18
298-102